THERMODYNAMICS AND MECHANISMS OF ORGANOCHLORINE POLLUTANTS ADSORPTION ON ZEOLITES

TIMOTHY MANDA

A Thesis Submitted to the Board of Postgraduate Studies in Partial Fulfillment of the Requirements for the Award of a Degree of Master of Science in Physics

SCHOOL OF BIOLOGICAL, PHYSICAL, MATHEMATICS AND ACTUARIAL SCIENCES

JARAMOGI OGINGA ODINGA UNIVERSITY OF SCIENCE AND TECHNOLOGY

DECLARATION

This thesis is my original work and has not been presented for a degree award in Jaramogi Oginga Odinga University of Science and Technology or any other institution.

Signature……Date:…… ……

Timothy Manda

Adm. No: S251/P/0013/21

APPROVAL

This thesis has been submitted for examination with our approval as the university supervisors.

1. Signature  Date:……

   Dr. Godfrey Barasa

   Department of Physical Sciences

   School of Biological, Physical, Mathematics and Actuarial Science

   Jaramogi Oginga Odinga University of Science and Technology

2. Signature:…  Date: ……

   Dr. Solomon Omwoma

   Department of Physical Sciences

   School of Biological, Physical, Mathematics and Actuarial Science

   Jaramogi Oginga Odinga University of Science and Technology.

ACKNOWLEDGEMENT

I give God the glory for endowing me with the knowledge, insight, and understanding that have been essential to finishing this work. Along with my family, I want to thank Sarah Shisia, my older sister, for taking on the burden and providing me with financial support. I also appreciate Dr. Godfrey Barasa and Dr. Solomon Omwoma Lugasi, my exemplary supervisors, for their direction, counsel, and overall support in getting this work done. I would especially want to thank Dr. Anthony Pembere for technical knowhow on molecular simulations and Dr. Livingstone Ochilo for the high performance computer which set a strong pillar for this work. I want to express my gratitude to the Austrian Partnership Programme in Higher Education and Research (APPEAR, Project 249) for full scholarship. The JOOUST community has been instrumental in this project. It is impossible to ignore the lab and working atmosphere that JOOUST offers. I sincerely thank each and every one of my friends who have helped make my work successful. May God richly bless JOOUST and all of Kenya.

DEDICATION

This writing is a tribute to my mother Grace Nanzala Manda and my elder sister Sarah Shisia Shiyuka.

ABSTRACT

Zeolites, mineral substances composed of aluminum and silicon, have found industrial applications in purification and as a separation technique for compounds. For instance, zeolites can separate isomers, gases and remove volatile organic compounds from some waste air streams. Their porous structures are utilized to "sieve" the molecules/compounds of specific size hence separating them from their mixtures. Technologically, the separation can be enhanced by fine-tuning and adjusting zeolite pore sizes and their surface morphology. In order to achieve this mechanism of fine-tuning zeolites, there is a need to understand zeolite separation mechanisms and their associated thermodynamics. For instance, isosteric heats of an adsorbent can affect its homogeneity and consequently separation efficiency. In the current study, therefore, we explore physical chemical parameters of various types of zeolites adsorption using selected organic pollutant molecules. Effect of doping to adsorption is also investigated. Adsorption parameters including isosteric heats, adsorption sites, adsorption isotherms, activation energies, temperature and loading rates are determined for various types of zeolites using selected organic pollutants. Mulliken charges are also investigated. Thereafter, laboratory adsorption experiments were done to verify loading rates of the zeolites. The average values of isosteric heats for the studied organic pollutants range between 0 to 59 kcal, which is synonymous with physical adsorption mechanisms of the organic compounds and also indicate a homogeneous mixture of the adsorbate and adsorbent. Among the 245 types of zeolites studied, zeolite Cloverite (CLO) gave the best loading rate for all the studied organic pollutants. It is demonstrated that zeolites can separate the various organic chemicals from polluted water environments using different adsorption sites. Furthermore, under low concentrations of adsorbate, the adsorption process on zeolites obeys a pseudo second order kinetic. In addition, sticking probability of adsorbate to adsorbent maximizes at activation energy (Ea) then reduces, indicating the ability of avoiding secondary waste generation through control of Ea. Doping the zeolites with aluminum increases the ability to adsorb organochlorines. It is also noted that charge transfer takes place during adsorption. Laboratory experiments required high silica zeolite in order to pack the columns. Addition of silica gel to the zeolite in the ratio 5;3 was found to be appropriate in order to make slurry. Sorption experiments revealed that clinoptilolite zeolite clogged the columns hence no adsorption. Untreated synthetic zeolite FAU was the best adsorbent with a removal percentage of 95%. Furthermore, untreated zeolite could be reused several times before reaching the saturation point contrary to treated zeolite. The interstitial water within the untreated zeolite provides the active oxygen sites for adsorption thus making it the best adsorbent compared to the treated zeolite with no water in its framework. Experimental results thus agree with our simulation results.

TABLE OF CONTENTS

LIST OF TABLES

LIST OF FIGURES

LIST OF ABBREVIATIONS

SAR	Silicon/aluminum ratio
MC	Monte Carlo simulations
MD	Molecular dynamic simulation
POPs	Persistent organic pollutants
CBA	Chitin based adsorbents
AMBER	Assited model building with energy refinement
GAFF	Generalized AMBER force field
COMPASS	Condensed-Phase optimized molecular potentials for atomistic simulation studies
CVFF	Consistent valence force field
UFF	Universal force field
SCCPs	Short chain chlorinated paraffins
MCCPs	Medium chain chlorinated paraffins
CPs	Chlorinated paraffins
PCB	Polychlorinated biphenyl
PAHs	Polycyclic aromatic hydrocarbons
IZA	International zeolites association
HOMO	Highest occupied molecular orbital
LUMO	Lowest unoccupied molecular orbital
Di	Largest overall cavity diameter
D	Density
M	Mass
HVF	Helium void fraction
APV	Accessible pore volume
VSA	Volumetric surface area
GSA	Gravimetric surface area
DPS	Dimensionality of the pore system

CHAPTER ONE
INTRODUCTION

1.1 Background

Zeolites are environmentally compatible crystalline solids, implying that their activities does not harm the environment, or at least minimizes their negative impact to the environment. Zeolites micro-pore dimensions and physico-chemical properties strongly depend on their framework composition[1]. This means that zeolites' The hydrophilic/hydrophobic character of these materials can be tailored by varying the SiO_2/Al_2O_3 ratio (SAR)[2]. Zeolites three dimensional framework, generating nanometer-sized channels and cages, imparts to them high porosity and large surface areas[3]. Therefore, the three-dimensional framework of zeolites is based on their crystal or lattice structure. On the other hand, the shape of the internal pore structure strongly affects the adsorption selectivity towards host molecules. For these reasons, zeolites have been used as adsorbent media for specific classes of chemicals, including hydrocarbons[4,5,6], halocarbons[7,8,9] and pharmaceuticals[10,11,12].

Adsorption mechanisms of drugs on zeolites can involve both non-specific (ionic) and specific interactions due to the formation of well-defined local chemical bonds, either covalent or supramolecular[13]. For a given adsorbent material, the different interactions will depend on the acid-base properties, the number of H-donor groups, and the hydrophobicity of substances. Recent studies evidenced the presence of stable H-bonded adducts for drug adsorbed from aqueous solution on zeolites[10]. In addition, zeolites can exchange K^+, Na^+, Cu^{2+}, Ba^{2+}, Mg^{2+}, Cd^{2+}, and Rb^{2+} cations[14]. As a result, its application in the petrochemical and engineering catalysis sectors has drawn interest recently. By being divided into various classes like zeolite X, zeolites' commercial usage is further strengthened [15]. Zeolite A, zeolite CHA[16], zeolite FAU[17], and zeolite Y[18] are all classes of zeolites. Based on particular characteristics of zeolite materials, this categorization was created. Several studies have shown that zeolites are good adsorbents for various contaminants[19,20]. The grand canonical ensemble and statistical physics can be used to fit the simulation of the isotherms of adsorption of organic contaminants on zeolites at 298 K[21].

In statistical physics modeling, each model statement represents a particular instance of an adsorption process. These models are developed gradually, starting with the simplest Langmuir model (one site energy, one site occupation, and one layer), and moving on to more complex adsorption processes like the Hill model (monolayer, mono-energy, and multi-occupancy), double Hill (monolayer, different site energies, and mono-occupancy), or BET (multilayer, multi-site energies, mono or multi occupancy)[21]. The tested models are influenced by the properties of the curve form, including the linearity, shape, amount of saturation, slope at the curve's origin, and presence or absence of saturation. A coefficient of fitting quality makes it possible to choose, from among all a priori provided models, the model that best describes the nature of the adsorption process and the energies of different adsorption interactions involved in the adsorption process. However, it is impossible to determine the chemical origin and structure unless a fitting energy is a priori assigned to a recognized chemical functional group[22]. Therefore, this task can be completed using molecular simulation techniques. Entropy, internal energy, and Gibbs free energy are three thermodynamic functions that are calculated and evaluated to conduct a macroscopic analysis. Regardless of the particle motion equations, the Monte Carlo (MC) simulation approach creates a number of microscopic states under a certain stochastic law. The MC method is just a simulation tool for events in thermodynamic equilibrium because it does not use equations of motion and hence cannot incorporate the concept of explicit time. This method uses a probability density function to create a number of tiny states. The following is the main algorithm for the MC simulation of a non-spherical particle system:

(i) Describe each particle's beginning position and motion.

(ii) Calculate the interaction energy U_i using this state as the microscopic state i

(iii) Select a random or arbitrary particle and designate it as "particle α"

(iv) Use random numbers to translate the particle, then compute the interaction energy U_j for this new arrangement.

(v) For the example if $U_j \leq U_i$, adopt this new microscopic state and proceed to Step 7.

(vi) Determine ρ_j/ρ_i for the scenario where $U_j > U_i$ and select R_1 at random from a uniform random number sequence with values ranging from 0 to 1.

Adopt this microscopic state j and go to Step 7 if $R_1 \leq U_j/U_i$. Reject this microscopic state if $R_1 > U_j/U_i$, treat the previous state i as the new microscopic state j, and move on to Step 7.

(vii) Use random values to alter the particle's orientation, then compute the interaction energy U_k in the new state.

(viii) If $U_k \leq U_j$, take on this new tiny state and repeat Step 2.

(ix) Determine ρ_k/ρ_j and select a random integer R_2 from the uniform random number sequence if $U_k > U_j$. Adopt this new microscopic state k and restart from Step 2 if $R_2 \leq \rho_k/\rho_j$. Reject this new state, use the prior state j as the new microscopic state k, and start over at Step 2 if $R_2 > \rho_k/\rho_j$.

The potential energy of a system of particles is described by force field functions and parameter sets, which are generated from both experimental work and complex quantum mechanical computations (typically molecules and atoms). Both bound terms pertaining to atoms connected by covalent bonds and nonbonded (sometimes referred to as "noncovalent") terms characterizing the long-range electrostatic and van der Waals forces are included in the fundamental functional form of a force field. A broad form for the total energy in an additive force field can be stated as in **eq. 1.1**;

$$E_{total} = E_{bonded} + E_{non-bonded} \quad 1.1$$

but the precise decomposition of the terms depends on the force field.

where the following summations provide the components of the covalent and noncovalent contributions:

$$E_{bonded} = E_{bond} + E_{andle} + E_{dihedral} \quad 1.2$$

$$E_{nonbonded} = E_{electrostatic} + E_{vanderwaals} \quad 1.3$$

The accepted model can then be used to derive the thermodynamical potential functions that control the adsorption process, such as internal energy E_{int}, free enthalpy of Gibbs G_a, and entropy S_a. To ascertain if the process is feasible or not, certain thermodynamic parameters must be determined. Knowing the direction in which the reaction would occur is also made possible by thermodynamics. In predicting the best zeolite for adsorption of

organic pollutants, the three thermodynamic parameters have been calculated. This is significant in determining the mechanisms of adsorption as well as the direction in which the process takes place and further stating the possibility of the process. In order to study the adsorption mechanisms of the 245 zeolites, various organo-chlorine pollutants have been selected and used in the present study. The selected organic pollutants have been previously detected in environmental samples beyond allowable limits[23]. According to reports from 2019, Lake Victoria is more heavily polluted than usual by persistent organic pollutants [23]. This has an impact on the standard of the water supplied for home and commercial use. Both people and aquatic creatures who use the lakes' waters may experience health issues as a result of these chemicals, which are endocrine disruptors. It would be proper to use water purification techniques to get rid of these chemicals, but all of them have been shown to be costly, time-consuming, and some even discharge dangerous byproducts into the environment. Therefore, given their affordability and environmental friendliness, zeolites can be a promising choice for the adsorption of POPs like HCB[24]. Since most of these toxins are anthropogenic in origin, a unique remediation strategy is required. However the availability of a large number of zeolite to date makes it not easy to select the best zeolite for adsorption. This would require experiment with all the zeolites before getting the best material. This is however, not possible as laboratory experiments would take a lot of time and resources and sometimes tiresome as a result of several failures. To get rid of this challenge, the current study employs Monte Carlo simulations in predicting the optimal zeolite for organic pollutants adsorption.

1.2 Problem Statement

The presence of organic pollutants (POPs) in the environment has been reported by previous researchers. These pollutants include organochlorine compounds which were found present in L. Victoria in 2019. Basing on this, several methods have been attempted to get rid of these compounds in order to increase clean water availability, but all have faced numerous setbacks, including cost, time requirement and environmental unfriendliness. Thus, the need for effective techniques of removing these compounds is required. One of the most effective ways is the use of sorption techniques on porous materials. Zeolite adsorbents have been proved to be the best adsorbents for various applications. In this regard they can as well be utilized as adsorbents for organic pollutants such as organochlorides. Numerous theoretical and experimental research have been conducted to explain how molecules adhere to porous materials[21]. The adsorption thermodynamics for the interaction of the adsorbate molecules with the receptor sites of zeolites, however, remain a subject of ongoing debate. Since there are a large number of different zeolites discovered (over 240 types), getting the best zeolite for application is the greatest challenge. By simulating macroscopic properties using microscopic factors, such as adsorption energies, chemical potential, etc., statistical thermodynamics based on mathematical models enables the prediction of the optimal zeolite for application. For their use in various fields, it is crucial to investigate POPs' adsorption using a statistical physics technique in micro porous materials.

1.3 Objectives

1.3.1 Main Objective

To determine thermodynamics and mechanisms of organochlorine pollutants adsorption on zeolites.

1.3.2 Specific Objectives

i. To simulate hence predict organic pollutants adsorption thermodynamics and mechanisms on zeolites (245 types) using molecular dynamics simulations technique.

ii. To determine, experimentally, organic pollutant loading rates using any one of the studied pollutants in objective one and compare experimental and simulation results hence verify objective (i).

1.4 Justification of the Study

Zeolites adsorbents have been proved as the best adsorbents for various substances. This is due to their unique features and performance abilities. For instance, zeolites have been used as adsorbents for gaseous molecules such as CO_2 and Hydrogen. Others include heavy metals, dyes such as methylene blue, organic micro pollutants. Similarly, zeolites can as well be employed in adsorption of organic pollutants. However, from the previous studies, there has been no clear classification of all available zeolites adsorbents with the adsorbate materials that can be adsorbed. Therefore, there is need to carry out trials with all the materials in order to get the optimal. Doing this experimentally for over 245 zeolites would require a lot of time, space, finances and other resources making it difficult. Thus, molecular dynamic simulations would be more appropriate for predicting the best adsorbent material. Simulations have been successfully performed previously. For instance, Amira et al 2017[25] issued a review paper where zeolites have been used to adsorb gases. Wanda et al 2022 also presented results on simulation experiments on gas adsorption in zeolites[26]. From these examples it will also be possible to carry out simulation for organic pollutants. However these simulation results have to be tested and proved by laboratory experiments.

1.5 Significance of the Study

One of the most effective strategies for treating and removing harmful contaminants from the environment is the adsorption process using solid adsorbents[27]. Natural zeolite adsorbent is inexpensive and widely available. Other organic contaminants have been known to adsorb from wastewaters using natural zeolite. Because of their widespread availability, they are viable alternatives for wastewater cleanup, lowering the health risks associated with pollution exposure. This study's findings will provide scientific information on the efficacy of treatment for selected organic pollutants, as well as the extent of pollution.

CHAPTER TWO
LITERATURE REVIEW

2.1. Introduction

Environmental science has attracted many scholars around the world as a result of the growing number of modern issues affecting the ecosystem[28]. The availability of drinkable water for use by humans and animals is the key factor impacting the environment[29] . This is a result of both industrialized and developing nations' continuous industrialization. In order to ensure that the supply of clean water is restored, various scientists have tried to develop remedies[30]. Adsorption has drawn the most attention out of all the techniques used because it has attracted many scientists to its promising results. As a result, this has been the subject of several studies under a variety of conditions, including temperature, pressure, pH, time, and many more. Material scientists have already started researching the synthesis of zeolites for adsorption[31]. As a result, the adsorption mechanisms of different zeolites for different materials have been investigated.

This chapter focuses on contemporary research on zeolites adsorptions conducted by various specialists and molecular simulations that have successfully been employed in problem solving. To begin with, a general review has been done on molecular simulations, zeolites, and their structure and attributes as presented by recent research, including ion compositions. Furthermore, this chapter contrasts zeolites with other adsorbing substances, such as chitin-based adsorbents (CBA), which have also been discovered[32]. Finally, the chapter includes a summary of existing organic pollution removal techniques, along with a discussion of their drawbacks.

2.2 Molecular Simulations

Microscopic analysis techniques are required in the present era of nanotechnology in order to create new functional materials and examine physical processes at the molecular level. These techniques take into account the species that make up a system, like molecules and tiny particles. The behavior of these species can be studied to derive macroscopic and microscopic quantities of interest. The Monte Carlo (MC) and molecular dynamics (MD) methods are examples of what are known as "molecular simulation methods[33]." While MC techniques are effective for analyzing thermodynamic

equilibrium, they are inappropriate for analyzing dynamic processes. This is because MC simulations typically involve generating a large number of samples from a probability distribution that is stationary and time-independent, whereas dynamic processes involve time-dependent changes in the system. While MD techniques can be used to study thermodynamic equilibrium[34], they are more effective when examining a system's dynamic qualities when it is not in an equilibrium state.

2.2.1 Force Fields

The selection of force fields in molecular simulations is crucial[35]. The term "force field" is used differently in chemistry and computational biology than it is typically used in physics. Instead of being the gradient of a scalar potential as it is defined in physics, it is a system of potential energy functions in chemistry. The force field equations are derived from the potential energy function, and they represent the gradients of the potential energy with respect to the positions of the atoms or molecules[36]. In other words, the force field equations specify how the potential energy changes as the positions of the atoms or molecules are varied. The potential energy function itself is a scalar function that depends on the positions of all the atoms or molecules in the system[37]. It is not the gradient of a scalar potential or a system of potential energy functions, but rather a single function that captures all of the interactions between the particles in the system. Generally, the force field equations are the gradients of a scalar potential energy function that represents the sum of terms that describe various types of interactions between the atoms or molecules in a system[38]. Typically, harmonic oscillators **eq. 2.1,** are used to represent the bond and angle terms in force fields that forbid bond breakdown. This is given as;

$$E_R = \frac{1}{2} K_{ij}(r - r_{ij})^2 \qquad 2.1$$

The more expensive Morse potential, **eq.2.2,** gives a more accurate representation of a covalent bond at higher stretching.

$$E_R = D_{ij}[e^{-\alpha(r - r_{ij})} - 1]^2 \qquad 2.2$$

$$\alpha = [\frac{K_{ij}}{2D_{ij}}]^{\frac{1}{2}} \qquad 2.3$$

$$r_{ij} = r_i + r_j + r_{BO} + r_{EN} \qquad 2.4$$

The Morse potential level spacing diminishes as the energy approaches the dissociation energy, in contrast to the equally spaced energy levels of the harmonic oscillator potential. Due to the zero point energy of the lowest (v = 0) vibrational level, the dissociation energy D_{ij} is more than the actual energy needed for dissociation D_0.[39]. (See the **figure 2.1**)

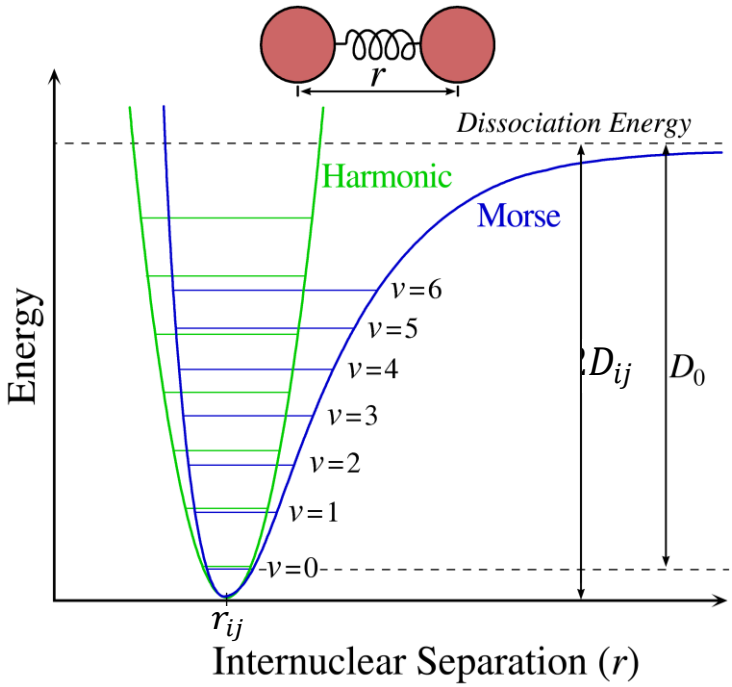

Figure 2.1: *The harmonic oscillator potential (green) and the Morse potential (blue)*[28].

The rest of the bonded terms have a very flexible functional shape. Usually, accurate dihedral potentials are supplied. Additionally, "cross terms" that characterize coupling of various internal variables, such as angles and bond lengths, may be introduced to ensure the planarity of aromatic rings and other conjugated systems. Hydrogen bonding are also explicitly described in several force fields[40]. Since there are many more interactions per atom in the nonbonded terms[41], they need the most computation. Limiting interactions to pairwise energies is a common decision. The electrostatic term is typically calculated using Coulomb's law, and the van der Waals term with a Lennard-Jones potential, but both can be scaled or buffered by a constant amount to take into account electronic polarizability and produce results that are more in line with experimental observations.

For each kind of atom, a force field specifies a set of parameters in addition to the functional form of the potentials[42]. For instance, a force field would have different characteristics for an oxygen atom in a functional group that is carbonyl and one that is hydroxyl. The typical parameter set consists of the effective spring constant for each potential as well as values for the atomic mass, van der Waals radius, and partial charge for each individual atom[43]. It also includes equilibrium values for the bond lengths, bond angles, and dihedral angles for pairs, triplets, and quadruplets of bonded atoms.

2.2.1.1 Assisted Model Building with Energy Refinement (AMBER)

The late Peter Kollman's Introduction to Molecular Dynamics 5 group at the University of California, San Francisco created the AMBER family of force fields for MD simulation of biomolecules[44]. The MD software program that mimics these force fields goes by the moniker AMBER. The functional form employed by the family of AMBER force fields is often referred to as a "AMBER force field." There are several parameters in this form, and each member of the family of AMBER force fields has its own name and values for each one[45]. The AMBER force field's functional is illustrated by **eq 2.5**:

$$V(r^N) = \sum_{bonds}\frac{1}{2}k_b(l-l_0)^2 + \sum_{angles}\frac{1}{2}k_a(\theta-\theta_0)^2 \quad + \sum_{tortions}\frac{1}{2}V_n(1 + \cos(n\omega-\gamma)) \; + \sum_{j=1}^{N-1}\;\sum_{i=j+1}^{N}\left(\varepsilon_{i,j}\left[-2\left(\frac{r_{0ij}}{r_{ij}}\right)^6\right] + \frac{q_iq_j}{4\pi\varepsilon_0 r_{ij}}\right) \qquad 2.5$$

where k_a and k_b are the force constants determined experimentally, l is the bond length after stretching, l_0 is the equilibrium bond length, θ is the bond angle after bending, θ_0 is the equilibrium bond angle, V_n is the energy term, n is the periodicity parameter, ω is the dihedral bond torsion angle, γ is the phase parameter, $\varepsilon_{i,j}$ is the well depth, r_{0ij} is the distance at which the interaction energy between the two atoms is zero, r_{ij} is the separation between the molecules, q_iq_j is the atomic charges on the atoms/molecules, and ε_0 is the permittivity of free space. The force is the derivative of the system's potential energy with respect to location, which is defined by this equation despite the phrase "force field" being used[46]. The following are the definitions of terms from the right side: The energy between atoms that are covalently bound is represented by the first term (which sums over bonds). Near the equilibrium link length, this harmonic (ideal

spring) force is a decent approximation, but as atoms separate, it becomes progressively worse[47]. The energy resulting from the geometry of the electron orbitals engaged in covalent bonding is represented in the second term (summing over angles). The third term (summing over torsions): This term denotes the energy required to twist a bond as a result of surrounding bonds, lone pairs of electrons, and bond order (such as double bonds). It should be noted that a single bond may have multiple instances of these components, resulting in a Fourier series that represents the overall torsional energy. The nonbo nded energy between all atom pairs is represented by the fourth term (double summation over i and j), which can be divided into van der Waals (first term of summation) and electrostatic (second term of summation) energies.

2.2.1.2 Generalized AMBER force field (GAFF)

To make it easier to simulate medications and their small-molecule ligands in combination with biomolecules, GAFF contains parameters for small organic molecules. The Generalized AMBER Force Field (GAFF) is a widely used force field for molecular simulations in computational chemistry[48]. It is an extension of the original AMBER (Assisted Model Building with Energy Refinement) force field, designed to provide accurate descriptions of a wide range of organic and small inorganic molecules. GAFF was developed to address the limitations of traditional AMBER force fields, which were primarily designed for simulating biomolecules. The goal of GAFF was to provide a more general and transferable force field that could accurately describe a broader range of chemical compounds encountered in drug discovery, materials science, and other fields[49]. The GAFF force field incorporates parameters for a diverse set of functional groups, including common organic molecules, aromatic compounds, halogens, metals, and more[50]. It assigns atom types, bond parameters, angle parameters, torsion parameters, and partial charges to each atom in a molecule. These parameters are derived from experimental and quantum mechanical data, as well as empirical fitting to reproduce a variety of molecular properties. One key feature of GAFF is its ability to handle diverse chemical environments by using a set of generalized parameters. This makes it particularly useful for studying molecules with non-standard structures or modifications. However, it's worth noting that GAFF may not provide the same level of accuracy for specialized systems compared to force fields specifically tailored for those systems, such

as protein force fields for studying biomolecules[51]. GAFF has been implemented in several molecular simulation packages, including the widely used AMBER software suite. It has been applied in a wide range of research areas, such as drug discovery, molecular dynamics simulations, and computational chemistry studies involving small organic molecules.

2.2.1.3 GLYCAM force fields

For the purpose of simulating carbs, Rob Woods developed the GLYCAM force fields. The GLYCAM (GLYCogen parameters for CHARMM) force fields are a set of force fields specifically designed for simulating carbohydrates and glycoproteins in molecular dynamics simulations[52]. Carbohydrates play crucial roles in biological processes, and the GLYCAM force fields provide accurate descriptions of their conformational behavior and interactions with other biomolecules. The GLYCAM force fields were initially developed to complement the CHARMM (Chemistry at Harvard Macromolecular Mechanics) force field, which is a widely used force field for simulating biomolecular systems[53]. The GLYCAM force fields extend the CHARMM force field to include parameters for the unique structural features and chemical properties of carbohydrates. GLYCAM force fields assign atom types, bond parameters, angle parameters, torsion parameters, and partial charges to each atom in a carbohydrate or glycoprotein molecule. These parameters are derived from experimental data, quantum mechanical calculations, and empirical fitting to reproduce a range of carbohydrate properties, such as glycosidic bond conformations and anomeric equilibria[54].

One of the strengths of the GLYCAM force fields is their ability to accurately model the complex and diverse structural features of carbohydrates, including ring conformations, glycosidic linkages, and branch points. The force fields also include parameters for glycan-protein interactions, allowing for simulations of glycoproteins and protein-carbohydrate complexes. The GLYCAM force fields have been widely used in studies of carbohydrate-protein interactions, molecular recognition, enzymatic processes, and other areas of carbohydrate biology[55]. They have been implemented in popular molecular simulation software packages, such as CHARMM and AMBER, and have been continuously refined and updated to improve their accuracy and coverage of carbohydrate

structures. It's worth noting that the GLYCAM force fields are focused on carbohydrates and glycoproteins, and may not provide accurate descriptions of other types of molecules.

2.2.1.4 Condensed-phase optimized molecular potentials for atomistic simulation studies (COMPASS)

COMPASS[56] is a member of the consistent family of force fields, which includes the second-generation force fields consistent force field (CFF)91, polymer CFF (PCFF), CFF, and COMPASS. For organic compounds including H, C, N, O, S, P, halogen atoms and ions, alkali metal cations, and numerous biochemically significant divalent metal cations, they were parameterized against a wide variety of experimental observables. Based on CFF91, PCFF has been expanded to cover a wide range of organic polymers and (inorganic) metals. Condensed-phase properties, as well as various and empirical data for molecules in alone, were used to parameterize and validate this force field[57]. Because of this, a wide variety of molecules, both alone and in condensed phases, may have their structural, conformational, vibrational, and thermophysical properties accurately and simultaneously predicted by this force field. The COMPASS force field includes terms for bonds (b), eq. 2.7**,** angles (θ), eq. 2.8**,** dihedral (φ), eq. 2.9 and out-of-plane angles (χ), eq. 2.10**,** as well as cross terms and two nonbonded functions: a coulomb function for electrostatic interactions and a Lennard-Jones potential for van der Waals interactions:

$$E_{total} = E_b + E_\theta + E_\varphi + E_\chi + E_{b,b'} + E_{b,\theta} + E_{b,\varphi} + E_{\theta,\varphi} + E_{\theta'\theta} + E_{\theta\theta'\varphi} + E_q + E_{vdw} \quad 2.6$$

Where;

$$E_b = \sum_b [k_2(b - b_0)^2 + k_3(b - b_0)^3 + k_4(b - b_0)^4] \quad 2.7$$

$$E_\theta = \sum_\theta [k_2(\theta - \theta_0)^2 + k_3(\theta - \theta_0)^3 + k_4(\theta - \theta_0)^4] \quad 2.8$$

$$E_\varphi = \sum_\varphi [k_1(1 - \cos\varphi) + k_2(1 - \cos 2\varphi) + k_3(1 - \cos 3\varphi)] \quad 2.9$$

$$E_\chi = \sum_\chi k_2\chi^2 \quad 2.10$$

$$E_{b,b'} = \sum k\,(b - b_0)(b' - b_0') \quad 2.11$$

$$E_{b,\theta} = \sum_{b,\varphi} k\,(b - b_\theta)(\,\theta - \theta_0) \quad 2.12$$

$$E_{b,\varphi} = \sum_{b,\varphi} (b - b_0)[k_1 \cos\varphi + k_2 \cos 2\varphi + k_3 \cos 3\varphi] \quad 2.13$$

$$E_{\theta,\varphi} = \sum_{\theta,\varphi} (\theta - \theta_0)\,[k_1 \cos\varphi + k_2 \cos 2\varphi + k_3 \cos 3\varphi] \quad 2.14$$

$$E_{\theta,\theta'} = \sum_{\theta,\theta'} k\,(\theta - \theta_0)(\theta' - \theta_0') \quad 2.15$$

$$E_{\theta,\theta'\varphi} = \sum_{\theta,\theta',\varphi} k\,(\theta - \theta_0)(\theta' - \theta_0')\cos\varphi \quad 2.16$$

$$E_q = \sum_{ij} \frac{q_i q_j}{r_{ij}} \quad 2.17$$

$$E_{vdw} = \sum_{ij} \sum_{ij} \left[2\left(\frac{r^0{}_{ij}}{r_{ij}}\right)^9 - 3\left(\frac{r^0{}_{ij}}{r_{ij}}\right)^6 \right] \quad 2.18$$

where k, k_1, k_2, k_3, and k_4 are the force constants determined experimentally; b and θ are the bond length and bond angle after stretching and bending, respectively; b_0 and θ_0 are the equilibrium bond length and equilibrium bond angle, respectively; φ is the bond torsion angle; χ is the out-of-plane inversion angle; E_b,b_0, E_θ,θ_0, E_b,θ, E_b, φ , E_θ, φ , and E_θ,θ_0 , φ are the cross terms representing the energy due to interaction between bond stretch-bond stretch, bond bend-bond bend, bond stretch-bond bend, bond stretch-bond torsion, bond bend-bond torsion, and bond bend-bond bend-bond torsion, respectively; $\varepsilon_{i,j}$ is the well depth; $r_{ij}{}^0$ is the distance at which the interaction energy between the two atoms is zero; r_{ij} is the separation between the atoms/ molecules; q_i, q_j are the atomic charges on the atoms/molecules; and ε_0 is the permittivity of free space.

2.2.1.5 CHARMm force field

CHARMm, which stands for Chemistry at HARvard Macromolecular Mechanics, is a highly adaptable molecular dynamics and mechanics program that was first created in the Harvard University laboratory of Dr. Martin Karplus[58]. It was parameterized using tiny biological model geometry and ab initio energies. A flexible and thorough empirical energy function that is the accumulation of numerous separate energy factors is used by

CHARMm. Separable internal coordinate terms and pairwise nonbond interaction terms provide the foundation of the energy function. **Eq. 2.19** below provides an expression for the total energy. To replicate solvent effects, the electrostatic term might be scaled[59]. The functional form and van der Waals combination rules are derived from rare-gas potentials;

$$E_{pot} = \sum k_b(r - r_0)^2 + \sum k_\theta(\theta - \theta_0)^2 + \sum |k_\varphi| - k_\varphi \cos(n_\varphi) + \sum k_\chi(\chi - \chi_0)^2 + \sum \frac{q_i q_j}{4\pi\varepsilon_0 r_{ij}} + \sum \left(\frac{A_{ij}}{r_{ij}^{12}}\right) - \left(\frac{B_{ij}}{r_{ij}^{6}}\right) sw(r_{ij}^2, r_{on}^2, r_{off}^2) + E_{constraints} + E_{user} \quad 2.19$$

where k_b, k_θ, k_φ, and k_χ are the force constants for bond stretching, bond bending, bond torsion, and out-of-plane inversion, respectively; r, θ, and χ are the bond length, bond angle, and inversion angle respectively; r^0, θ_0, and χ^0 are the equilibrium bond length, equilibrium bond angle, and equilibrium inversion angle, respectively; rij are the separation between the atoms/ molecules; n is the periodicity parameter; q_i, q_j are the atomic charges on the atoms/molecules; ε_0 is the permittivity of free space; A_{ij} and B_{ij} are the distances over which the interatomic interaction is zero; and $E_{constraint}$ and E_{user} are the energies arising due to constraint (if applied) and certain user-defined terms (to customize the force field), respectively.

The r^{12} term is the repulsive term, describing Pauli repulsion at short ranges due to overlapping electron orbitals, and the r^6 term is the attractive long-range term. As a default energy phrase, hydrogen bond energy is excluded. The present CHARMm parameter set was developed in a way that electrostatic and van der Waals forces work together to characterize hydrogen bond effects[60].

2.2.1.6 Consistent valence force field (CVFF)

The Discover program's original force field, the CVFF, is a generalized valence force field. Amino acids, water, and numerous other functional groups are given parameters. CVFF[61] has the capacity to use automated parameters, which assign missing parameters'

values automatically, in the absence of explicit parameters. The output file from the calculation makes note of these. Small organic crystals and gas-phase structures, such as amides, carboxylic acids, etc., were fitted by CVFF. It deals with proteins, peptides, and a variety of chemical systems[62]. It has been widely utilized for many years as Discover's default force field. Although it reasonably predicts vibrational frequencies and conformational energies, its primary use is for studies of structures and binding energies. The CVFF force field's out-of-plane energy is calculated using an incorrect torsion. An incorrect torsion perceives three atoms that are related to one another and a center atom as torsion. Based on permutations of the connected atoms, there are three potential incorrect torsions that can be formed for a specific out of plane[63]. Only one of these incorrect torsions is utilized for CVFF. The energy expression utilized in CVFF is represented analytically in the following equation **eq. 2.20.** The bond lengths, bond angles, torsion angles, and out-of-plane interactions' relative energies of deformation are represented by terms 1-4, which are referred to as the diagonal terms of the valence force field. The bond-stretching term is expressed as a Morse potential (Term 1). For this term, the Discover software also supports a straightforward harmonic potential[64]:

$$
\begin{aligned}
E_{pot} = & \sum_{D_b}\left(1 - e^{-\alpha(b-b_0)}\right) + \sum_{\theta} H_\theta\,(\theta-\theta_0)^2 \\
& + \sum_{\varphi} H_\varphi(1 + s\cos(n\varphi)\,) \\
& + \sum H_\chi \chi^2 \\
& + \sum_{b}\sum_{b'} Fbb'(b-b_0)(b'b_0') \\
& + \sum_{\theta}\sum_{\theta'} F_{\theta\theta'}(\theta-\theta_0)(\theta'-\theta_0') \\
& + \sum_{b}\sum_{b_\theta} F_{b_\theta}(b-b_0)(\,\theta-\theta_0) + \sum_{\varphi} F\varphi_{\theta\theta'}\cos\varphi\,(\theta-\theta_0)(\theta'-\theta_0') \\
& + \sum_{\chi}\sum_{\chi} F_{\chi\chi'}\chi\chi' + \sum \varepsilon\left[\left(\frac{r^*}{r}\right)^{12} - 2\left(\frac{r^*}{r}\right)^{6}\right] \\
& + \sum \frac{q_i q_j}{\varepsilon r_{ij}}
\end{aligned}
\qquad 2.20
$$

where D_b is the well depth or bond dissociation energy; α is the parameter that controls the width of the potential well (the smaller the "α," the larger the well); b and b_0 are the separation between atoms and equilibrium bond distance, respectively; θ and θ_0 are the bond angle and equilibrium bond angle, respectively; χ is the inversion angle; n is the periodicity parameter; q_i, q_j are the atomic charges on the atoms/molecules; ε is the well depth (in Term 10) and permittivity of free space (in Term 11); H_θ, H_φ, and H_χ are the constants associated with bond bending, torsion, and out-of-plane inversion, respectively; F_b,b_0, F_θ,θ_0, F_b,θ, F_φ ,θ,θ_0, and $F_{\chi,\chi 0}$ are the cross terms representing the energy due to interaction between bond stretch-bond stretch, bond bend-bond bend, bond stretch-bond bend, bond torsion-bond bend-bond bend, out of plane/out-of-plane inversion, respectively; r* is the separation at which interatomic potential is zero; and r is the separation between the atoms[64].

2.2.1.7 DREIDING force field

The structures and dynamics of organic, biological, and main-group inorganic compounds can be predicted using this general force field. The atom kinds are the constituent parts of the DRE8lDlNG force field. The molecular mechanics force field treats atoms of the same atom type the same way[65]. A superposition of valence (or bonded) interactions (E_{val}), **eq.2.22** that depend on the specific connections (bonds) of the structure and nonbonded interactions (E_{nb}), **2.27,** that depend only on the distance between the atoms is used to express the potential energy for a molecule with any conceivable geometry;

$$E = E_{val} + E_{nb} \quad 2.21$$

$$E_{val} = E_B + E_A + E_T + E_I \quad 2.22$$

$$E_B = \frac{1}{2} K_e (R - R_e)^2 \quad 2.23$$

$$E_A = \frac{1}{2} K_{ijk} \left[\theta_{ijk} - \theta_j^0\right]^2 \quad 2.24$$

$$E_T = \frac{1}{2} V_{jk} \left[1 - \cos\left[n_{jk}(\varphi - \varphi_{jk})\right]\right] \quad 2.25$$

$$E_I = \frac{1}{2} K_{inv} (\varphi - \varphi_n)^2 \quad 2.26$$

The energy for non-bonded is given as

$$E_{nb} = E_{vdw} + E_\varphi + E_{hb} \quad 2.27$$

2.2.1.8 Universal force field (UFF)

A collection of hybridization-dependent atomic bond radii, a set of hybridization angles, van der Waals parameters, torsional and inversion barriers, and a set of effective nuclear charges are among the parameters used to create the universal force field[64]. For a molecule, the potential energy is expressed as a superposition of several two-body, three-body, and four-body interactions. The total of valence or bound interactions and nonbonded interactions represents the potential energy illustrated by eq.2.28:

$$E = E_R + E_\theta + E_\varphi + E_\omega + E_{vdw} + E_{el} \qquad 2.28$$

The valence interactions consist of bond stretching E_R discussed and angular distortions E_θ discussed earlier. Included as angular distortions are bond angle bending E_θ, dihedral angle torsion (E_φ) and inversion terms (E_ω). The nonbonded interactions consist of van der Waals (E_{vdw}) terms and electrostatic(E_{el}) terms (their illustrations are given from eq. 2.6 above)

2.2.2 Potentials

Use of proper inter atomic energies and forces is required for the atomistic MC and MD modeling techniques, which have had an impact on everything from medication design to crystal development. These interactions are typically modeled using first-principle total-energy calculations, semi empirical electronic structure approaches, or analytical potential energy expressions[66].

The bond stretch interaction is described by the universal force field as either a harmonic oscillator illustrated by eq. 2.29:

$$E_R = \frac{1}{2} K_{ij}\left(r - r_{ij}\right)^2 \qquad 2.29$$

Or as the Morse function:

$$E_R = D_{ij}[e^{-\alpha(r - r_{ij})} - 1]^2 \qquad 2.30$$

where k_{ij} is the force constant in units of (kcal/mol), r_{ij} is the standard or natural bond length in angstroms, D_{ij} is the bond dissociation energy (kcal/mol), and;

$$\alpha = \left[\frac{K_{ij}}{2D_{ij}}\right]^{\frac{1}{2}} \qquad 2.31$$

Since the Morse function implicitly incorporates anharmonic terms close to equilibrium (r_{ij}) and results in a finite energy (D_{ij}) for bond breakage, it is a more realistic representation. The natural bond length r_{ij} is taken to be the total of single bond radii particular to each atom type plus bond order and electronegativity corrections[67]:

$$r_{ij} = r_i + r_j + r_{BO} + r_{EN} \quad 2.32$$

2.2.3 Ensemble

Ensemble is a grouping of many systems that are microscopically diverse yet macroscopically same[68]. In statistical thermodynamics, we only look at the average attributes of the particles that make up a macroscopic sample rather than their behavior. Particles are virtually absent from classical thermodynamics. Such a thermodynamic is only interested in bulk properties, such as the quantity of particles N, the temperature T, and the container volume V. The ergodic theorem states that the average value we calculate over this huge number of replications is exactly the same as the temporal average we would derive by examining the time history of the original system. The two are identical. At the molecular level, not all of the ensemble's cells are exact duplicates of one another[69]. Simply put, we make sure that each cell has a specified quantity of identical thermodynamic characteristics. At this point, there is no discussion of molecular characteristics. An ensemble of cells with identical N, V, and T values may be shown in the **Figure 2.2** below. A canonical ensemble is stated to be formed by this collection of cells. According to what is held constant in each cell, there are three additional significant ensembles in the theory of statistical thermodynamics[70]. We have the following ensembles in addition to the classical ensemble, where N, V, and T are kept constant: The microcanonical ensemble, where each cell's N, E, and V values are fixed. As a result of the fact that energy cannot move from one cell to another, this ensemble is actually incredibly simple. (ii) A constant is maintained for N, T, and P in an isothermal-isobaric ensemble. (iii) The grand canonical ensemble is the last one, which maintains constants for V, T, and the chemical potential. The fact that the number of particles can vary makes the vast canonical ensemble attractive[71].

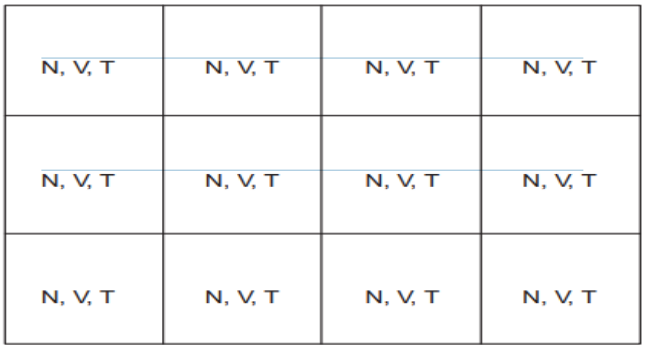

Figure 2.2: *A canonical ensemble illustration with number of particles N, volume V and temperature T kept constant.*

In the context of adsorption, the concept of an ensemble refers to a collection of identical or similar systems that differ only in their initial conditions or configurations[69]. Ensembles are useful for understanding the statistical properties of a system, such as its thermodynamic behavior and the likelihood of observing certain configurations or events[72]. One important application of ensembles in adsorption is the study of the adsorption isotherm[69], which describes the relationship between the amount of adsorbate (e.g., gas) adsorbed on a surface and the pressure or concentration of the adsorbate in the surrounding environment. The adsorption isotherm is often modeled using different types of ensembles, such as the grand canonical ensemble, the canonical ensemble, or the microcanonical ensemble. For example, in the grand canonical ensemble, the total number of particles (i.e., the adsorbate molecules) and the chemical potential of the system are fixed, but the number of particles in the adsorbed phase can fluctuate. This ensemble is useful for modeling adsorption processes that occur at constant chemical potential, such as gas adsorption on a solid surface. In the canonical ensemble, the number of particles and the volume of the system are fixed, but the energy of the system can fluctuate[73]. This ensemble is useful for adsorption on a porous material. Ensembles can also be used to model the kinetics of adsorption processes[74], by considering the time evolution of the distribution of particles in the system. This approach can be useful for predicting the rate and mechanism of adsorption, and for designing materials with specific adsorption properties. In summary, the concept of an ensemble is relevant to adsorption because it allows for the statistical analysis of the thermodynamic and kinetic

properties of adsorption systems, and can be used to model and predict the behavior of these systems under different conditions[75].

2.3 Zeolites

Zeolite is a naturally occurring aluminum silicate that can also be synthesized. The pore structure of zeolite is three-dimensional (**Figure 2.3**). Silicon, aluminum, and oxygen ions make up this compound. In the crystal structure, the silicon ions are neutrally loaded. Negative regions are created by the aluminum ions. A cation (Na^+, K^+) or a proton (H^+) is introduced in the pores as a counter-ion to maintain the load balanced[76].

Each zeolite variety contains pores of the same size throughout the crystal structure. These material types with same pore structure throughout the structure are referred to as Hierarchical[77]. The ring size of a crystal structure influences its structure in part. The pore size as well as the counter-ion can be altered by changing the aluminum/silicon ratio. Natural zeolites are hydrophilic and contain aluminum. These materials make a good combination.

Table 2.1 : *Properties of major synthetic zeolites*[78]

Zeolite Type	Pore Size Dimensions (Å)	Silica to Alumina Ratio	Applications
Zeolite A	4.1	2–5	Detergent manufacturing
Faujasite	7.4	3–6	Catalytic cracking and hydro cracking
ZSM-5	5.2×5.8	30–200	Xylene isomerization, benzene alkylation, catalytic cracking, catalyst dewaxing, and methanol conversion
Mordenite	6.7×7.0	10–12	Hydro-isomerization and dewaxing

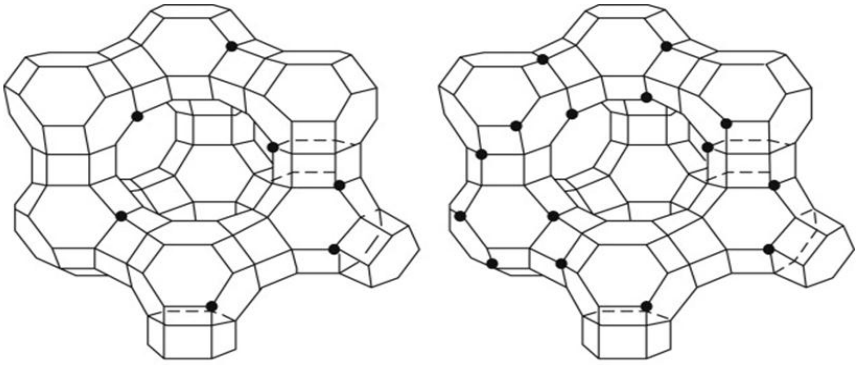

Figure 2.3: a) *USY zeolite and b) equilibrium REY zeolite*[78]

Zeolites have been found in Kenya. The most notable occurrence of zeolites in Kenya is in the Lake Magadi area[79], which is located in the southern part of the country[80]. The Lake Magadi area is known for its extensive deposits of trona and nahcolite, which are minerals that are often associated with zeolites.

2.4 Zeolites' adsorption phenomena

Adsorption is the process of solute molecules accumulating at an interface. Gas–solid and liquid–solid interfaces have the most adsorption processes, with solute dispersed preferentially between the fluid and solid phases. Due to the limited amount of accumulation per unit surface area, extremely porous substances with a large internal area per unit volume are recommended[81,82]. Physical and chemical adsorptions are the two types of adsorptions that have been recognized. Physical adsorption, also known as physisorption, is based on van der Waals forces (vapor condensation), whereas chemical adsorption, also known as chemisorption, is based on chemical bonding.

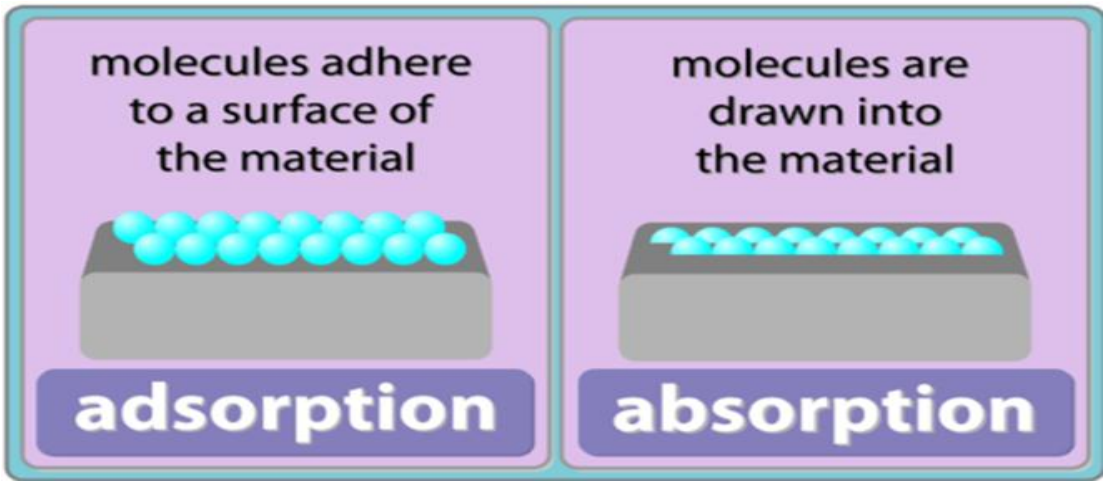

Figure 2.4: *Difference between adsorption and absorption as modified from reference* [83]

The former is better suited to a regenerable process, whereas the latter tends to degrade the adsorbent's capacity[84]. This means that zeolites can be used and later regenerated by cleaning the active sites covered by the by-products of adsorption. Because of their effectiveness in removing contaminants, adsorption techniques have recently gained in their favor. Adsorption is also a viable treatment option, especially if the adsorbent is affordable and easily available. The adsorption method has the advantages of being sludge-free, clean, and removing contaminants completely even in dilute solutions. As a result, adsorption is one of the most cost-effective and efficient methods for removing contaminants from wastewater. For instance Lamia and coworkers looked into the adsorption kinetics of methylene blue (BM) on zeolites as one way of addressing water pollution[85]. Dyes were the most significant contaminants in their research. The authors did this by conducting a parametric investigation of adsorption and the effect of various key parameters on adsorption of BM on the material employed, in particular the contact time (equilibrium was reached after 120 minutes), different adsorbent concentrations, varied masses, pH and temperature. These parameters had a critical role in their tests, as evidenced by the results. Lamia et al and colleagues conducted a kinetic investigation and used kinetic models such as pseudo-first order and pseudo-second order to analyze the experimental results. In this investigation, two types of adsorbent materials were employed to illustrate their methylene blue dye adsorption mechanisms: natural clay and activated clay. Natural zeolites were not used since they were not available.

Furthermore, Lamia et al. did not investigate the adsorption of organic pollutants, which are jeopardizing the availability of a clean environment, in their study. This study focused on the adsorption kinetics of methylene blue (BM) on zeolites as a means to address water pollution caused by dyes. While their research provided valuable insights into the adsorption parameters and mechanisms for dyes, it did not include an investigation of organic pollutants such as organochlorines. This research gap highlights the need for a specific study that explores the adsorption behavior of organochlorines on zeolites. Heavy metals, in addition to dyes, have been identified as water pollutants, and methods for their removal have been developed. Yuna evaluated the removal of heavy metals from wastewater using natural, modified, and manufactured zeolites[86]. In his review, Yuna outlined the applications of natural, modified, and synthetic zeolite in the removal of heavy metals from waste water solutions, and compared the removal effectiveness on the same heavy metal. For comparison analysis, three types of zeolites, including natural, modified, and synthetic zeolites, were employed to remove the same heavy metal, thus Yuna chose an appropriate adsorbent based on the features of the wastewater in use. He discovered that modified and synthetic zeolites had better cation exchange capacities and were more stable than natural zeolites.

The sorption process of three types of zeolites was mostly spontaneous and endothermic, and heavy metal ions were removed by adsorption and ion exchange processes. As a result, he concluded that zeolites are effective adsorbent materials with a wide range of applications in the removal of heavy metals from waste water. Yuna, on the other hand, dealt on heavy metal adsorption in his study review. Yuna's review examined the removal of heavy metals from wastewater using different types of zeolites. Although the study compared the effectiveness of natural, modified, and synthetic zeolites for heavy metal removal, it did not delve into the adsorption mechanisms of organic pollutants. Hence, a dedicated study focusing on the thermodynamics and mechanisms of organochlorine pollutants on zeolites is still lacking. Another sort of adsorbent material, on the other hand, was developed by Parthasarathy and Narayanan for defluoridation of drinking water[87]. According to their research, a novel low-cost composite adsorbent for removing excess fluoride from drinking water was successfully manufactured using waste egg shell (ES), alum, and chitin. Variation of synthesis parameters such as alumina loading,

ES:chitin ratio, calcinations temperature, calcinations time, shaking time, drying temperature, and washing time were used to optimize the synthesis of chitin-based adsorbent (CBA). Narayan and Parthasarathy suggested that using XRD and other techniques, they were able to prove the presence of several phases of alumina, including crystalline and amorphous phases for defluoridation of drinking water. According to Parthasarathy and Narayanan (2014), CBA is a composite material containing heterogeneous phases of $Ca(OH)_2$, $Al(OH)_3$, Al_2O_3 encapsulated with carbon, $Al(OH)_3$ and Al_2O_3 coated on carbon and Al_2O_3. They found out that by using XRD and SEM techniques, they were able to prove the presence of several phases of alumina, including crystalline and amorphous phases.

The material's elemental composition and EDX results both pointed to a composite nature of the material with several phases. Their SEM image of CBA revealed the presence of both coarse and tiny particles, as well as irregularly shaped alumina agglomerates clinging to ES calcite particles. According to this research, CBA beat several reported adsorbents with its greater adsorption capacity of 30.3 mg g-1, which showed that defluoridation performance was comprehensively evaluated for CBA. CBA followed pseudo second order kinetics, and the fluoride adsorption mechanism was complicated, involving both intra-particle and surface diffusion in the rate-limiting step. Parthasarathy and Narayanan developed a composite adsorbent material for defluoridation of drinking water, but their research did not address the adsorption of organochlorine pollutants. This further emphasizes the need for a study specifically targeting the adsorption behavior of organochlorines on zeolites.

Furthermore, Chitin has an amide group per glucose unit; this amide group contains an electron pair that is available for coordination and behaves like a Lewis base. These mechanisms are often complex because they necessitate the presence of several interactions such as ion exchange, complex coordination/chelation training, electrostatic contacts, acid–base interactions, and hydrogen bonds[85]. In this regard, zeolites provide the finest mechanisms since they entail ion exchange due to their charged nature, as well as acid-base interaction due to their acidic sites. Several other studies have been published on the use of clinoptilolite-rich rock for removing NH_4^+ from water. For

instance, Parthasarathy and Narayanan in 2014 prepared distilled water (electrical conductivity 1 S/m) by first removing NH_4^+ using a Chinese clinoptilolite (0.4-0.8 mm) and then passing the water through a commercial cation-exchange column. Kallo in 2001 harvested drinking water from ground water by removing NH_4^+ (5.6 mg/L) via ion exchange with clinoptilolite-rich material (Georgian occurrence) and removing H_2S (1.5 mg/L) via oxidation with chlorine and sodium hypochlorite, which was electrolytically produced from a NaCl regeneration solution[88]. Obtaining drinking water from most natural resources, as well as wastewaters with different levels of pollutants, necessitates water treatment. Large particles, such as bacteria or suspended solids, as well as dissolved or colloidal inorganic and organic compounds, may include these contaminants. Kallo in his work in 2018 gives an overview of the use of natural zeolites in water and wastewater purification to remove Persistent organic pollutants[88]. In all the above research items, there is no single research that identifies adsorption thermodynamics and mechanisms of organochlorines on zeolites. Overall, the existing literature review highlights the research gaps in understanding the adsorption thermodynamics and mechanisms of organochlorine pollutants on zeolites. By addressing these gaps, a study focused on investigating the adsorption behavior of organochlorines on 245 zeolites would contribute valuable knowledge to the field of wastewater treatment and provide insights into the efficient removal of these pollutants from contaminated water sources.

2.5 Persistent organic pollutants. (POPs)

Persistent organic pollutants (POPs), also known as "forever chemicals," are organic molecules that are resistant to chemical, biological, and photolytic breakdown in the environment[89]. They're poisonous compounds that have a negative impact on human health and the environment all over the world. Most POPs generated in one country can and do impact people and wildlife far from where they are used and discharged because they can be transferred by wind and water. The impact of persistent organic pollutants (POPs) on human and environmental health was debated by the worldwide community in 2001 at the Stockholm Convention on Persistent Organic Pollutants, with the goal of eliminating or severely limiting their production[90]. The United States has taken significant domestic measures to limit POP emissions. For example, none of the initial

POPs pesticides specified in the Stockholm Convention are now registered for sale and distribution in the United States, and in 1978, Congress banned the manufacture of polychlorinated biphenyl (PCB) and severely limited the use of residual PCB stocks[91]. Furthermore, since 1987, the Environmental Protection Agency and the states have effectively decreased environmental emissions of dioxins and furans from U.S. sources to land, air, and water[92].

Hexachlorobenzene (**Figure 2.5**) is a byproduct of industrial operations and incinerator activities, as well as a former organochlorine fungicide. It has been identified as a potential carcinogen to living beings[91]. It is prohibited worldwide under the Stockholm Convention on Persistent Organic Pollutants. Prior to its prohibition in the United States, the chemical was widely used as a seed treatment fungicide for onions, sorghum, wheat, and other cereals. It was also utilized as a chemical intermediate in the manufacturing of dyes and the synthesis of other organic chemicals, as a raw material in the development of pyrotechnic compositions for the military, as a plasticizer for polyvinyl chloride, and as a wood preservative. It has the ability to bioaccumulate in fat and bio magnify in tissues of living animals at the top of the food chain[23]. HCB is insoluble in water but soluble in organic solvents.

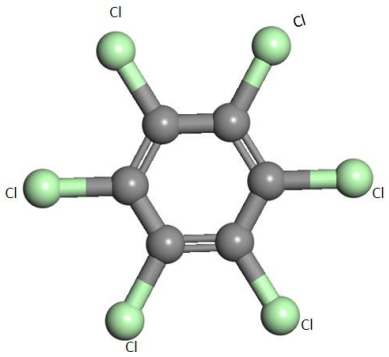

Figure 2.5: *Hexachlorobenzene structure used as a seed treatment fungicide*

It is very volatile, and as a result, it is likely to partition into the atmosphere. It is highly resistant to decomposition and has a high partition coefficient (KOW=3.03-6.42) and is known to bioconcentrate in live creatures' fats. As a result, HCB is illegal in Austria, Belgium, Slovakia, Denmark, the European Union, and Germany Hungary,

Liechtenstein, the Netherlands, Panama, Switzerland, Turkey, the United Kingdom, and the United States. In Argentina, New Zealand, and elsewhere, it is severely restricted or has been voluntarily withdrawn[89].

2.6 Effects of HCB to living organisms

In humans, chronic (long-term) oral exposure to hexachlorobenzene causes liver illness with accompanying skin lesions. Epidemiologic investigations were done in 1965 using some samples of individuals and it was found that those who were orally exposed to hexachlorobenzene found no evidence of an elevated cancer risk. However, the EPA has classed hexachlorobenzene as a possible carcinogen based on animal studies that have documented cancer of the liver, thyroid, and kidney from oral exposure to hexachlorobenzene (Group B2). There is very little evidence on inhaling[93].

Porphyria, skin lesions, hyper excitability, weight changes, enzyme activities, and liver morphology have all been linked to HCB sub chronic toxicity. In addition, HCB has been shown to activate the immune system in rats while suppressing the immune system in mice. HCB has also been linked to negative effects on fertility and reproductive tissue[89].

So far, several remediation approaches have been used to remove PCB contaminants from the environment. However, none of the strategies were successful in reaching this goal. Chemical reagent, supercritical water oxidation, ultrasonic radiation, bimetallic systems, nZVI, and nZVI combination with a second metal, for example, have high remediation efficiency (78–99%) and a short reaction time[94]. However, these technologies are frequently prohibitively expensive. The remediation efficacy of phytoremediation and microbial degradation is low (40–60%)[95]. Despite the fact that phytoremediation and microbial degradation have a low remediation efficiency and a long remediation time, the main advantage is the inexpensive implementation costs. As a result, they are not suitable for full-scale application at an in-situ contaminated site. When compared to the technologies listed above, activated carbon and the biofilm coated activated carbon techniques received the highest rankings in this table. Because of their low cost and relatively high remediation efficiency (more than 60%), they can be used for both in-situ and ex-situ PCB remediation[96]. Because PCBs are complicated substances, knowledge of their chemical and physical properties is essential for better

understanding of their movement and fate and, as a result, selecting effective cleanup measures. This study advocates for sorption as the most cost-effective, dependable, and environmentally acceptable method of removing organochlorine pollutants.

2.7 Chlorinated Paraffins (CP)

Chlorinated paraffins (CPs), which include short-chain chlorinated paraffins (C10–C13, SCCPs), medium-chain chlorinated paraffins (C14–C17, M[97]CCPs) and long-chain chlorinated paraffins (C18–C30, LCCPs), are complex mixtures of polychlorinated n-alkanes[98]. Short and Medium Chain Chlorinated Paraffins (SCCPs and MCCPs, respectively) are chemicals that are persistent, bioaccumulative and toxic to aquatic organisms [99]. For several decades, they have been used in industrial applications such as high-temperature lubricants, plasticizers, flame retardants, and additives in adhesives, paint, rubber, and sealants. Among all CPs, SCCPs have gained the most attention due to their properties including long-range transport potential [95,99, 100], bioaccumulation potential [101,102,103], and chronic toxicity to organisms [104, 105]. SCCPs have been listed in Annex A at the eighth meeting of the Conference of the Parties to the Stockholm Convention (SC) in May 2017 as new persistent organic pollutants (POPs) [106]. Similarly, as a subclass of CPs, MCCPs are also widely applied in industrial production and can enter the environment when being produced and used. They possess chemical properties like those of SCCPs. Therefore, MCCPs can also potentially have adverse effects on the environment and human health [107, 108, 109]. China began the CP production in the 1950s, and it is currently the largest producer and user of CPs in the world [97]. Since the 1990s, both the production and release of CPs into the environment have soared globally. Literature studies indicate that SCCPs and MCCPs are widely distributed in different environmental matrices [110,102,101,111,112,113]. However, CP levels in environmental matrices of remote areas have scarcely been reported. Remote high-altitude mountain regions always have low temperature and high precipitation, and thus can trap various semi-volatile chemicals through distillation and cold condensation effects, which is also known as “mountain cold-trapping”.

2.8. Polycyclic aromatic hydrocarbons (PAHs)

PAHs have been commonly detected in air, soil and water entailing a ubiquitous environment risk[114]. The low solubility of PAHs in water causes their attachment to the surface of particular matter which enables them to reach the hydrosphere[115]. According to Karyab et al [116], PAHs enter water sources predominantly through fossils fuels combustion, petroleum spill, road runoff, industrial wastewater, leaching from creosote-impregnate wood and dry and wet deposition[116]. Hence, PAHs have been reported in drinking water, rivers and lakes, groundwater, wastewater, seawater and sediments[117].

2.9 Thermodynamics of adsorption in zeolites adsorbents

The thermodynamic behavior of the sorption of organic compounds onto zeolites adsorbents from aqueous solution shows whether the sorption process follows physisorption or chemisorption. In physisorption, a weak Van der Waals attraction is observed between an adsorbate (organic compound) and a surface. However, chemisorption occurs by the formation of chemical bonds between the surfaces of solid (adsorbent) and the compound. In this case, it is difficult to remove adsorbate being adsorbed from the adsorbent; therefore, chemisorption is of irreversible nature. In contrast, the process of physisorption is reversible, i.e., desorption of the adsorbate occurs by increasing the temperature and does not require any activation energy.

2.9.1 Significance of thermodynamic parameters for the adsorption of heavy metals onto green adsorbents

Thermodynamic parameters of adsorption from solutions provide a great deal of information concerning the type and mechanism of the adsorption process. The Gibbs energy change ΔG° is calculated from **eq. 2.33**:

$$\Delta G^0 = -RT ln\, K \qquad 2.33$$

A negative Gibbs free energy value indicates the feasibility and spontaneous nature of the adsorption process. The distribution constant K can be expressed as;

$$K = \frac{C_{ad}}{C_e} \qquad 2.34$$

In which C_{ad} and C_e are the concentration of solute adsorbed at equilibrium and the solute concentration in solution at equilibrium, respectively. R is the gas constant with a value of 8.314 J mol^{-1} K^{-1}, and T is the absolute temperature in kelvins.

The relationship of (ΔG°) to enthalpy change (ΔH°) and entropy change (ΔS°) of adsorption is expressed as equation. 2.35:

$$\Delta G^0 = \Delta H^0 - \mathrm{T}\Delta \mathrm{S}^0 \qquad 2.35$$

Using equation 2.33 in equation 2.35;

$$\ln K = \frac{-\Delta H^0}{RT} + \frac{\Delta S^0}{R} \qquad 2.36$$

The values of ΔH° and ΔS° are determined from the slope and intercept of the linear plot of$(\ln K)$ versus (1/T) of Equation 2.10.

The positive value of change in enthalpy (ΔH°) indicates that the adsorption is an endothermic process, while positive value of change in entropy (ΔS°) reflects the increased randomness at the solid/solution interface during adsorption process, whereas negative ΔS° values represent the opposite phenomenon (decreased randomness).

2.9.2 The adsorption isotherm

The adsorption isotherm displays information of how much material will adsorb for a given set of state variables (pressure P and temperature T when using gases as adsorptives, concentration c and temperature T when dealing with adsorption from solutions). The amount of adsorbed material can be given as surface coverage, i.e., the fraction of occupied/available sites, or by the volume V_m taken up by the sum of particles adsorbed in the first monolayer.

The adsorption isotherm is one of the most important criteria for an adsorption process. In practice, the uptake of adsorptive of a given catalyst material is a decisive quantity, since a high uptake usually means a (desired) high catalyst efficiency. The respective uptake is often called , 'sorption capacity' and characterised by the sorption (or adsorption) isotherm. The form of the sorption isotherm provides a lot of first-glance information about the chemical and physical properties of the catalyst material and about how the adsorption process proceeds over a given surface. In principle, various kinds of

isotherms can be distinguished, depending on the nature of the catalyst and the kind of interaction.

i) The Langmuir adsorption isotherm

The Langmuir adsorption isotherm is based on the fact that in adsorption - desorption equilibrium the rates of adsorption and desorption are equal, while the rate of adsorption is determined by the collision frequency of the gas phase particles with the surface. The Langmuir adsorption isotherm is expressed as equation. 2.37;

$$K(T) = \frac{S_0}{\nu N_{max}} (2\pi mkT)^{-1/2}\, exp\left(\frac{E_{des}}{kT}\right) \qquad 2.37$$

With S_0 representing the initial sticking coefficient, ν the frequency factor of the desorption reaction, K (T) is the equilibrium constant at temperature T and N_{max} the maximum number of adsorbed particles: For non-activated (spontaneous) adsorption, the desorption energy E_{des} is equal to the energy of adsorption, E_{ad}. The adsorption equilibrium constant (K) is used to estimate thermodynamic parameters of adsorption However, the amount of adsorbed molecules is given by the Langmuir equation as;

$$q_e = q_{max} \frac{C_e K_L}{C_e K_L + 1} \qquad 2.38$$

In which q_e and q_{max} are the amount adsorbed at equilibrium and maximum adsorption capacity of adsorbent.

ii) The BET adsorption isotherm

The aim of this isotherm is to explain the physical adsorption of gas molecules on a solid surface and serves as the basis for an important analysis technique for the measurement of the specific surface area of materials. The BET equation is given as;

$$\theta = \frac{CP}{(1 - P/P_0)\big(P_0 + P(C-1)\big)} \qquad 2.39$$

Where C is referred to as the BET C-constant, P_0 is the vapor pressure of the adsorptive bulk liquid phase which would be at the temperature of the adsorbate and θ is the surface coverage, defined as:

$$\theta = n_{ads}/n_m \qquad 2.40$$

Here n_{ads} is the amount of adsorbate and n_m is called the monolayer equivalent. The n_m is the entire amount that would be present as a monolayer (which is theoretically impossible) for physical adsorption would cover the surface with exactly one layer of

adsorbate. The above equation, equation 2.13, is usually rearranged to yield the following equation for the ease of analysis:

$$\frac{\frac{P}{P_0}}{\nu[1-(P/P_0)]} = \frac{C-1}{\nu_m C}\left(\frac{P}{P_0}\right) + \frac{1}{\nu_m C} \qquad 2.41$$

Where P and P_0 are the equilibrium and the saturation pressure of adsorbates at the temperature of adsorption, respectively; $\nu$is the adsorbed gas quantity (for example, in volume units) while ν_m is the monolayer adsorbed gas quantity. C is the BET constant,

$$c = \exp\left(\frac{E_I - E_L}{RT}\right) \qquad 2.42$$

Where E_I is the heat of adsorption for the first layer, and E_L is that for the second and higher layers and is equal to the heat of liquefaction or heat of vaporization.

CHAPTER THREE

METHODOLOGY

3.1 Adsorption on various Zeolites (simulation experiments)

All the zeolites that were used in this study were obtained from the International Zeolites Association (IZA) database. The organic pollutants such as HCB structure was modeled using the material studio software. This was done by first sketching a benzene ring using the 'sketch a ring' on the sketch toolbar. The benzene ring was then filled with chlorine atoms on each carbon atom, ensuring the correct bonding of the atoms. The resultant compound was the required HCB compound. Since the structure resulting from initial sketch is usually not chemically reasonable [118] in the sense that it may violate certain fundamental principles of chemistry, such as the octet rule or the requirement for certain types of bonding , the sketch structure was 'cleaned' using the *clean* button on the sketch toolbar. There was a need of finally optimizing the structure and thus this was done using forcite module in material studio software. During geometry optimization, this module performs energy minimization on molecular and periodic systems. The module was chosen because it maintains the initial symmetry established by the space group throughout optimization, and the crystal structure is optimized either with regard to all structural degrees of freedom or using rigid body constraints, which fix the relative distances between a group of atoms. Furthermore, BIOVIA Materials Studio Forcite is intended to interact with a wide range of forcefields while providing simple and flexible access to the corresponding parameter settings[119]. All the other compounds were modeled in similar way with the use of appropriate atoms.

Material studio software contains various structures including zeolites, polymers, semiconductors, metals, and nanotubes. Having modeled and optimized the pollutant structure (sorbate), the zeolite (sorbent) structure was imported from the zeolite database. This was attained by selecting file and choosing *import* from the menu bar, or one could simply click the import button so as to open the *import document* dialog. This was then followed by careful navigation to the structures, zeolites and then selecting a zeolite. The desired zeolite was selected and opened. Before setting up the calculation, the symmetry of the sorbent was changed to P1 since sorption calculations require crystals without

symmetry as guest molecules would break any available symmetry [118]. To do this, we selected b*uild, symmetry* and selected *make P1* from the menu bar.

The sorption calculation was performed as follows, first the sorption tools button was identified from the task bar and calculations selected from the dropdown list. This displayed the sorption calculation dialogue from which adsorption conditions were set. Since we were interested in the adsorption of organic pollutants on zeolites, the task was set to adsorption isotherm using metropolis method[120]. The task quality was set to medium in order to achieve good results since realistic statistical analysis requires the Medium or Fine setting. However, it was noted that the fine quality took a lot of time giving similar results with the medium quality. The upper and lower fugacity at which calculations were performed was set as 1 atm (101.325 kPa) and 10 atm (1013.25 kPa), respectively. The Fugacity steps were set to 9 and the Logarithmic checkbox was checked. The Temperature was set to 298 K. The force fields options to be used in the calculation were selected from the energy tab of the sorption calculation dialog as universal. The quality of the energy calculation was set to medium with the previously mentioned reasons, setting the Ewald and group to electrostatic summation method. The van der Waals summation method was set to atom based. Finally, the appropriate properties calculation was selected from the properties tab of the sorption calculation by checking the check boxes for Energy distribution, Density field and Energy field. The sample interval was set to 50 and the grid resolution to medium which automatically set the grid interval to 0.4 Å. Calculations were then performed using the run tool in the title bar. The criteria used for selecting the parameters for calculation are based on established literature and experimental conditions for studying adsorption on zeolites. The temperature was set to 298 K, which is the standard temperature used for most experimental studies. The pressure range of 1-10 atm was chosen as it represents a range of typical environmental conditions and the sorption isotherm calculation was performed using the Metropolis method. The upper and lower fugacity limits were set to 1 atm and 10 atm, respectively, as these are common ranges for studying adsorption behavior. The force fields options used in the calculation were selected as universal and the quality of the energy calculation was set to medium, with the Ewald and group to electrostatic summation method and the van der Waals summation method set to atom-based.

This selection was made to ensure that the calculated results are both accurate and computationally feasible. The appropriate properties calculation was selected, including Energy distribution, Density field, and Energy field. These parameters were selected to ensure reliable and accurate results, and were based on previous studies and established best practices in the field. However, before running calculations for all zeolites, we first calculated the adsorption capacities using all the force fields in order to identify the best force fields. Other zeolites structural properties were obtained from iRASPA software. Adsorption locator was used to determine the adsorption sites for all the compounds.

To analyse the adsorption isotherms, origin pro software was used to fit all the plots obtained. Origin is a software application for interactive scientific graphing and data analysis. OriginLab Corporation created it, and it works on Microsoft Windows[121]. It produced a large number of platform-independent open-source clones and alternatives, including LabPlot and SciDAVis. Origin's graphing support provides a variety of 2D/3D plot types.

In Origin, data analyses include statistics, signal processing, curve fitting, and peak analysis. A nonlinear least squares fitter based on the Levenberg-Marquardt algorithm is used to fit the curves in Origin.

Origin accepts data files in a variety of formats, including ASCII text, Excel, NI TDM, DIADem, NetCDF, SPC, and others[122]. It also exports the graph to a variety of picture file types, including JPEG, GIF, EPS, TIFF, and others.

3.2 Laboratory Adsorption Experiments

3.2.1 Preparation of zeolites

The zeolites were obtained from Sigma Aldrich and were crushed to a required particle size to increase the surface area prior to thermal activation. The thermal activation process was carried out by following a previously reported method (cite the source) with slight modifications. Briefly, the required amount of the desired zeolite X was placed in a sample tube and plugged with glass wool to prevent the zeolite from being blown off. The sample tube was then connected to a vacuum pump under room temperature for 30 minutes to remove any moisture present in the zeolite. The temperature was then raised

gradually by 50 ℃ every 30 minutes until it reached 400 ℃, under vacuum conditions. This temperature was selected based on previous studies that have shown that it is sufficient to activate the zeolite[123 124]. The sample was then held at this temperature for 4 hours under a 10-5 torr vacuum to complete the activation process. Finally, the sample was carefully removed from the pump. The selection of the temperature for zeolite activation was based on previous studies that have investigated the effect of temperature on the physicochemical properties of zeolites[125]. It has been reported that the thermal stability of zeolites increases with increasing temperature, and temperatures above 300 ℃ are required to remove the water molecules present in the zeolite framework[126 127]. Moreover, studies have shown that high-temperature activation of zeolites can increase the surface area, pore volume, and pore size distribution, leading to enhanced adsorption properties[128]. Therefore, we chose to activate the zeolites, **Figure 3.1,** at 400 ℃ to ensure complete removal of the water molecules and to enhance their adsorption properties.

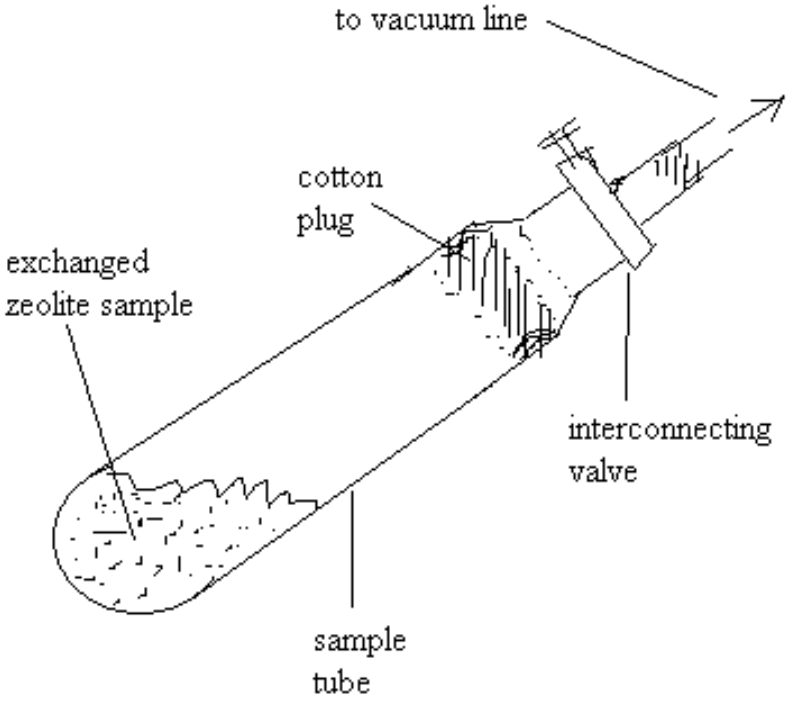

Figure 3.1: *Zeolite activation set up for laboratory sorption experiments.*

3.2.2 Adsorbate preparation

In a 500 ml volumetric flask, 300ml stock solution of 30 ppm was prepared. Using various standards of 1ppm, 2ppm, 3ppm, 4ppm, 5ppm, 6ppm, 7ppm, 8ppm, 9ppm, 10ppm 15ppm, 20ppm and 25ppm were prepared from the stock solution.

3.2.3 Standard calibration curve

The standards prepared were used to measure absorbance using a UV-Vis biospectrometer machine (Eppendorf AG 22331 Hamburg). The absorbance of each sample standard was measured seven times and the average value calculated. The standard deviation was then calculated from the obtained values. This was used to fix error bars on the calibration curve. A graph of absorbance against concentration was plotted.

3.2.4 Adsorption experiments

Zeolite x was mixed with silica gel in the ratio 5:3. This was done in order to increase the Si/Al ratio. This was done for both treated and untreated zeolite. The main aim was to increase hydrophobic nature of the zeolite in order to improve the adsorption. Zeolite clineoptile was also used to investigate the adsorption since it contains a higher Si/Al ratio. Silica gel was also investigated for its adsorption ability. Five columns were therefore set, one packed with silica gel, one with treated zeolite x, one with untreated zeolite x, one with treated clineoptile and one with untreated clineoptile zeolite. A standard solution of 15ppm was run through all the columns several times until there was no further change in concentration as determined from our developed standard curve.

CHAPTER FOUR

RESULTS AND DISCUSSION

4.1. Introduction

Force fields including hydrophobic effect, torsional angle, Lennard Jones distance and atom angle as illustrated in **Figure 4.0** provide initial parameters needed to calculate potential energy of a system in Monte Carlo simulations.

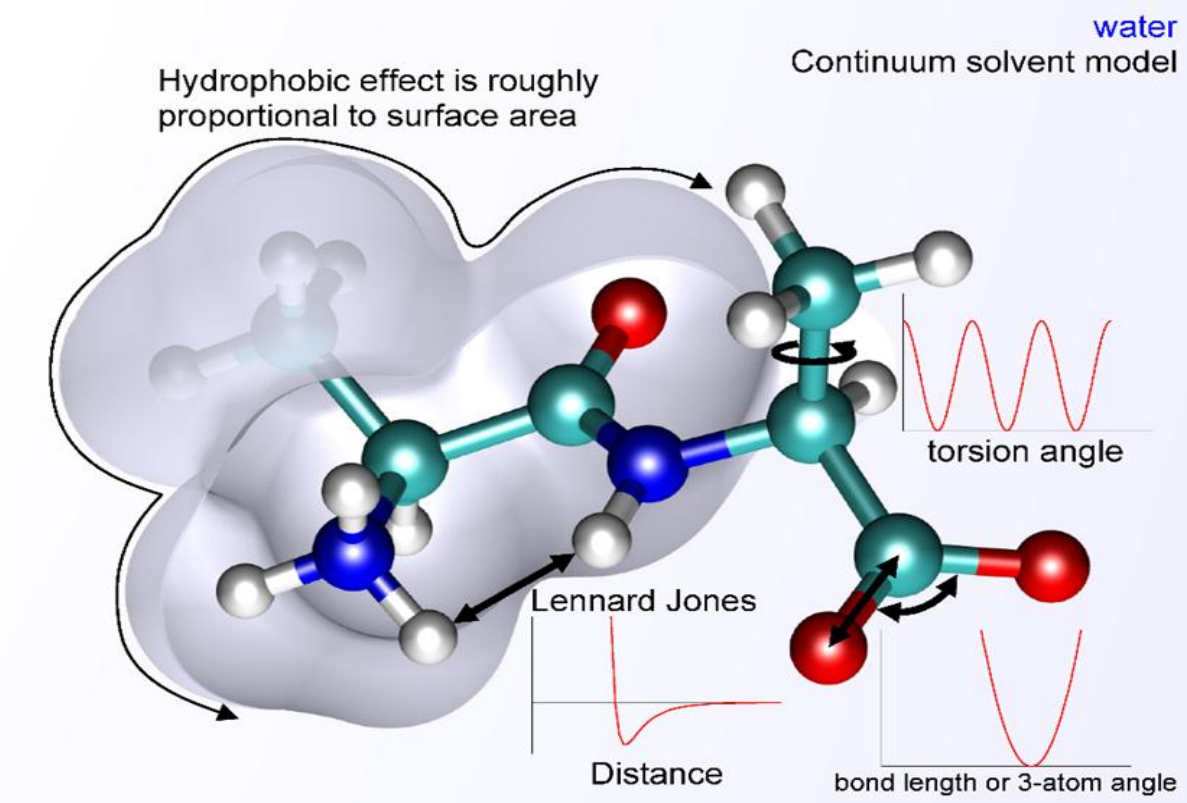

Figure. 4.0: *Illustration of various force fields exhibited by a molecule in motion. Adopted from Heinz et al. 2017*[129]

Other force field parameters include atomic mass, atomic charge and dihedral angles. Among the methods of determining force field parameters, it was found out that the universal force field method provide parameters necessary for optimal organic pollutant loading on zeolites (**Figure 4.1**).

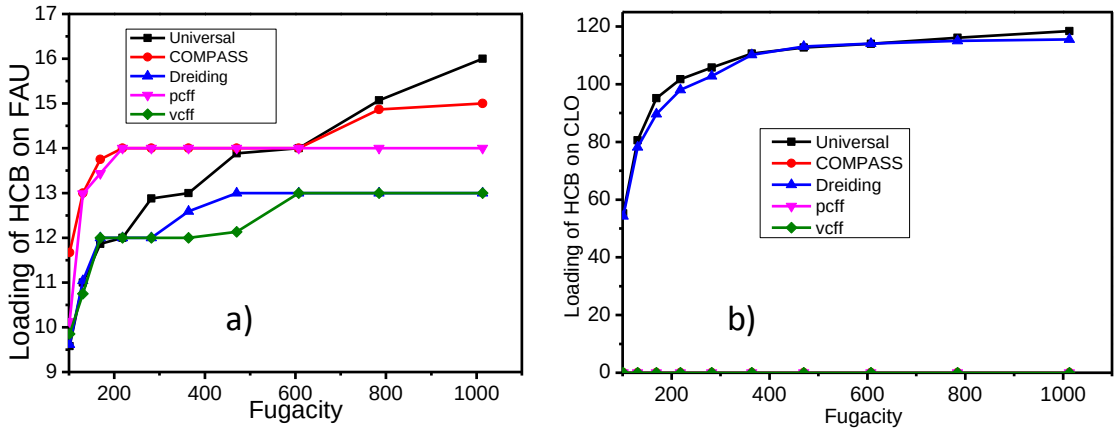

Fig. 4.1. *Loading of hexachlorobenzene (HCB) molecules on FAU zeolite (a) and CLO zeolite (b) at various forcefields. vcff: valency consistent force field; pcff: polymer consistent force-field; dreiding: a simple generic force field; COMPASS: condensed-phase optimized molecular potentials for atomistic simulation studies.*

Structural features of the 245 types of zeolites were determined including mass (M), density (D), helium void fraction (HVF), accessible pore volume (APV), gravimetric surface area (GSA), and dimensionality of the pore system (Di) (**Table Ap 4.1**). These results are placed in the appendix (Ap) due to their bulky nature. The structural features and hexachlorobenzene force fields were used to predict possible loading capacities of organic pollutants on specific zeolites. Activation energies in kcal and isosteric heats in kcal were also predicted for the adsorption processes. Based on the results in **Table Ap 4.1**, only 15 zeolites were selected to have substantive loading rates for organic pollutants. Consequently, the 15 resultant zeolites were predicted for loading of other organic pollutants including Hexachlorocyclohexane (**Table 4.2**), Dichlorodiphenyl trichloroethane (**Table 4.3**), Phenanthrene (**Table 4.4**), Fluoranthene (**Table 4.5**), Acenaphthylene (**Table 4.6**), Hexachlorotetradecane (**Table 4.7**), Heptachlorotetradecane (**Table 4.8**), Octachlorotetradecane (**Table 4.9**), Hexachlorodecane (**Table 4.10**), Heptachlorodecane (**Table 4.11**), and Octachlorobenzene (**Table 4.12**). A summary of the adsorption process provides CLO as the best zeolites adsorbent for the studied organic pollutants (**Table 4.1**). It is noted that whereas some organic pollutants adsorption would happen spontaneously (exothermic reactions), others would be non-spontaneous (endothermic) at 298 K and a pressure of

between 101.325KPa and 1013KPa. The adsorption process may be at equilibrium in an average of 30 minutes and the adsorbate would mix homogeneously with the adsorbent (isosteric heats of around 50 kcal) (**Table 4.1**).

Table 4.1. *Predicted organic pollutant loading rates (molecules per unit cell) on the best zeolite adsorbent with the accompanying activation energy, isosteric heat and approximate time of adsorption at a temperature of 298K and a pressure range of between 101.325KPa and 1013KPa.*

Organic Pollutant	**Zeolite**	**Loading (Molecules/cell)**	**Activation Energy Ea (kcal)**	**Isosteric Heat (kcal)**	**Time (Sec)**
Hexachlorobenzene	CLO	120	-642 (*exothermic*)	38	1340
Hexachlorocyclohexane	CLO	113	247 (*endothermic*)	40	1180
Dichlorodiphenyl trichloroethane	CLO	43	227 (*endothermic*)	44	857
Phenanthrene	CLO	132	999 (*endothermic*)	52	1880
Fluoranthene	CLO	105	4547 (*endothermic*)	53	1680
Acenaphthylene	CLO	167	5686 (*endothermic*)	48	2180
Hexachlorotetradecane	CLO	21	-125 (*exothermic*)	51	1280
Heptachlorotetradecane	CLO	22	-239 (*exothermic*)	52	1080
Octachlorotetradecane	CLO	19	-102 (*exothermic*)	56	1150
Hexachlorodecane	CLO	47	-2 (*exothermic*)	53	1120
Heptachlorodecane	CLO	30	-109 (*exothermic*)	53	1186
Octachlorobenzene	CLO	22	-189 (*exothermic*)	45	1160

Table 4.2; *Loading of Hexachlorocyclohexane (HCH) on selected zeolites, activation energies (E_a) and isosteric heats at a temperature of 298K and a pressure range of between 101.325KPa and 1013KPa*

S/No.	Zeolite	Loading	total energy	isosteric heats	Time taken (sec)
1.	CLO	113	246.857	39.492	1180
2.	TSC	24	-27.3	41.992	319
3.	ITV	19	64.688	37.692	221
4.	IFT	15	-34.234	44.092	317
5.	FAU	11	-23.818	42.992	212
6.	IRY	10	-13.47	45.392	335
7.	RWY	10	27.231	39.392	213
8.	DFO	10	-57.638	44.592	374
9.	SYT	9	-30.983	48.392	312
10.	LTA	8	-49.638	40.192	332
11.	LTN	8	-55.522	40.192	392
12.	SBT	6	-24.735	38.992	518
13.	EMT	6	-11.007	41.792	400
14.	SBS	5	-23.976	44.492	395
15.	MWF	2	-18.209	41.392	477

Table 4.3; *Loading of dichlorodiphenyl trichloroethane (DDT) on selected zeolites, activation energies (E_a) and isosteric heats at a temperature of 298K and a pressure range of between 101.325KPa and 1013KPa*

S/No	Zeolite	loading	total energy	isosteric heats	time taken (sec)
1.	CLO	43	227.244	43.292	857
2.	TSC	12	-62.998	53.992	337
3.	ITV	10	16.284	49.192	229
4.	FAU	6	-76.692	53.292	3472
5.	RWY	6	-7.76	51.492	585
6.	IRY	5	-19.815	50.992	428
7.	IFT	5	-31.744	48.592	333
8.	SBT	3	-31.593	53.192	603
9.	DFO	3	-21.878	52.792	394
10.	EMT	3	-34.122	53.792	409
11.	SBS	3	-39.912	55.492	509
12.	SYT	2	-0.27	38.992	299
13.	LTA	0	0	-	20
14.	LTN	0	0	-	39
15.	MWF	0	0	-	0

Table 4.4; *Loading of phenanthrene on selected zeolites, adsorption energies (E_a) and isosteric heats at a temperature of 298K and a pressure range of between 101.325KPa and 1013KPa*

S/No	ZEOLITE	LOADING	TOTAL ENERGY	ISOSTERIC HEAT	TIME
1.	CLO	132	999.188	52.192	1880
2.	TSC	30	3.857	57.892	1119
3.	ITV	26	131.213	55.792	821
4.	FAU	16	-3.395	57.792	717
5.	IFT	16	-18.046	59.992	212
6.	RWY	13	44.294	57.692	635
7.	DFO	12	1.148	52.692	313
8.	SBT	11	-12.558	56.992	374
9.	LTA	10	-16.375	54.892	312
10.	IRY	10	10.323	54.092	232
11.	SYT	10	-2.079	55.092	492
12.	LTN	8	-26.151	43.692	518
13.	EMT	8	-21.234	56.492	400
14.	SBS	6	2.268	53.192	395
15.	MWF	2	3.175	38.692	477

Table 4.5; *Loading of fluoranthene on selected zeolites, activation energies (E_a) and isosteric heats at a temperature of 298K and a pressure range of between 101.325KPa and 1013KPa*

S/NO	ZEOLITE	LOADING	TOTAL ENERGY	ISOSTERIC HEAT	TIME
1.	CLO	105	4546.752	53.792	1680
2.	TSC	25	856.737	64.592	839
3.	ITV	22	896.023	53.792	261
4.	FAU	15	497.665	64.292	317
5.	RWY	12	438.182	62.792	1129
6.	IFT	11	398.182	58.692	155
7.	IRY	10	336.115	64.392	213
8.	LTA	8	286.111	44.892	274
9.	LTN	8	240.683	47.592	312
10.	SYT	8	306.113	47.392	352
11.	DFO	8	259.318	55.892	392
12.	SBT	7	241.432	59.692	518
13.	EMT	7	233.222	61.192	610
14.	SBS	7	220.367	63.692	395
15.	MWF	0	0		417

Table 4.6; *Loading of acenaphthylene on selected zeolites, activation energies (E_a) and isosteric heats at a temperature of 298K and a pressure range of between 101.325KPa and 1013KPa*

S/NO	ZEOLITE	LOADING	TOTAL ENERGY	ISOSTERIC HEAT	TIME
1	CLO	167	5686.454	47.792	2180
2	TSC	38	1089.09	50.792	719
3	ITV	33	1075.544	47.492	1221
4	FAU	19	505.922	45.392	917
5	LTA	16	394.262	49.392	212
6	IRY	14	415.7.7	50.392	335
7	SBT	12	336.505	49.792	223
8	IFT	21	619.018	52.092	376
9	RWY	15	494.12	51.792	362
10	LTN	16	377.048	49.892	432
11	SYT	12	343.304	50.992	372
12	DFO	16	440.777	47.892	518
13	EMT	9	269.674	47.892	460
14	SBS	10	259.252	52.992	398
15	MWF	2	54.26	37.292	457

A graph of sorption probability (sticking probability), P(E), versus total energy of hexachlorobenzene on CLO is presented in **Fig. 4.2**. The parameter P(E) shows the potential of an adsorbate to remain on an adsorbent system and it serves the best purpose when its value lie between zero and unity ($0<P(E)<1$). The parameter P(E) is independent of the system's operating temperature[130]. Sticking probability can also be evaluated from **Eq. 4.1**;

$$\ln(1-\theta) = \ln(P(E)) + \frac{E_a}{RT} \qquad 4.1$$

Where; θ is the surface coverage and E_a is the activation/sorption energy. Activation energy is the minimum energy required to cause a chemical reaction. For sorption process, a negative activation energy suggests that a low temperature favors the process in which case the sorption process is termed to be exothermic[131, 132]. In **Fig. 4.2**, the maximum adsorption energy for adsorption of HCB on CLO zeolite was -27 kca/mol. At this value, the isosteric heats of adsorption (from **Table Ap 4.1**) was obtained as 38 kca/mol. From the work done by Sedlacek[133], it is noted that at maximum adsorption energy, the activation energy is approximately half of the isosteric heats. Basing on this,

the activation energy at this point was calculated as -19 kca/mol[134]. It is clear from **Fig. 4.2 a, b and c** that before the activation energy is attained, the sticking probability increases. However, at the optimum activation, the sticking probability is very high. Beyond activation energy, the sorption probability decreases. This behavior is evident for all adsorbates and adsorbents studied in this work. This shows that separation (adsorption) for the exothermic process should occur below E_a and regeneration of adsorbate should be done above E_a.

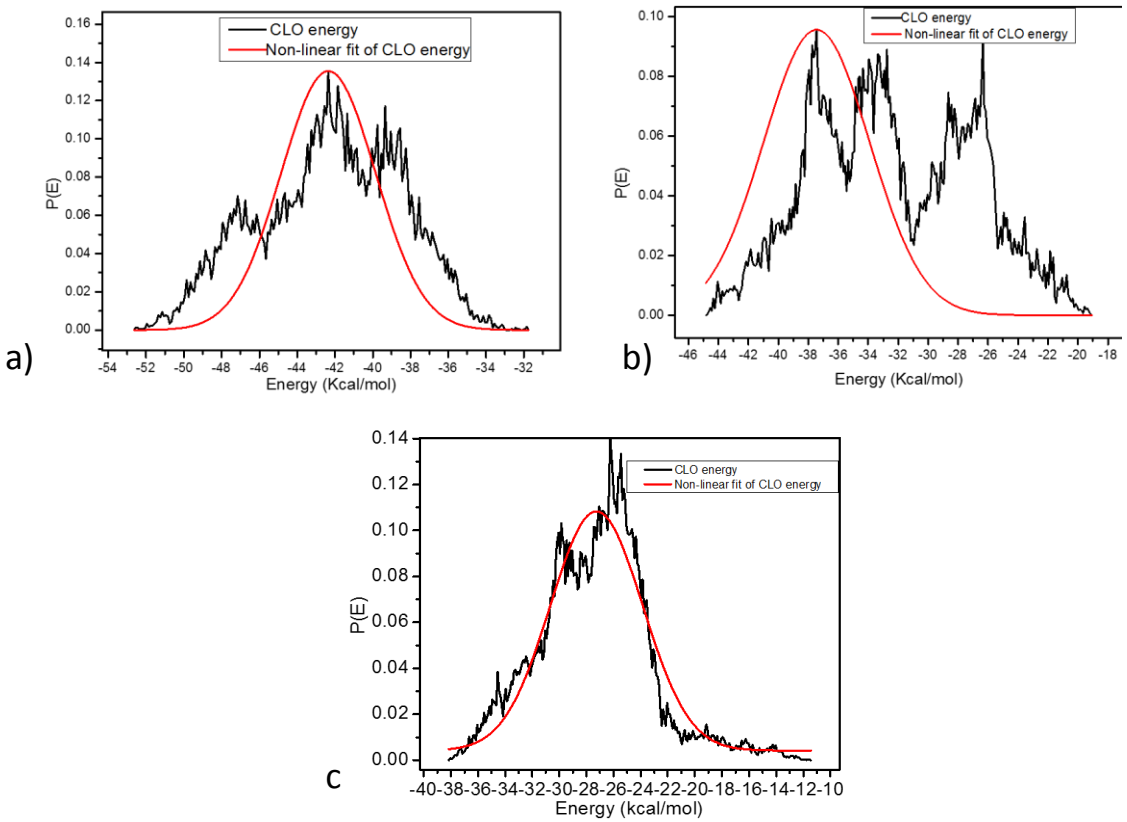

Figure. 4.2. *Sticking probabilities versus activation energy for adsorption of octachloroundecane a, heptachlorodecane b and hexachlorobenzene c on CLO zeolite.*

It is also evident, from Figure 4.2, that the activation energy for these organochlorines decreases with the increase in the number of chlorine atoms in the structure. This is evidenced from **Figure 4.2 a, b, c** in which octachloroundecane a) with eight chlorine atoms has Ea of -42Kcal/mol, heptachlorodecane b) with seven chlorine atoms has Ea of -36 Kcal/mol and hexachlorobenzene c) with six chlorine atoms has Ea of -27 Kcal/mol. This trend has been reported in previous studies and hence the results in the present study is justified. One study published in the Journal of Organic Chemistry in 2017 investigated

the effect of chlorine substitution on the activation energy of a series of reactions involving aromatic compounds[135]. The authors found that the presence of chlorines in the ortho position to a reaction site lowered the activation energy of the reaction, while chlorines in the meta or para position had no effect or even increased the activation energy. Another study published in Environmental Science and Technology in 2019 investigated the effect of chlorine substitution on the degradation of polychlorinated biphenyls (PCBs) in the environment[136]. The authors found that the presence of chlorine atoms in the PCBs lowered the activation energy of the degradation reactions, leading to faster degradation rates. These studies support the trend observed in the present study, that the activation energy of organochlorines decreases with an increase in the number of chlorine atoms in the structure. However, it is important to note that the effect of chlorine substitution on activation energy can depend on the specific reaction and the position of the chlorine atoms in the molecule.

Isosteric heat is the ratio of the infinitesimal change in the adsorbate enthalpy to the infinitesimal change in the quantity adsorbed under constant temperature and pressure[137]. It is the heat of adsorption established at constant amount of adsorbate adsorbed. This parameter is essential in characterization of adsorption process and is usually calculated using Clausius-Claperyron equation (**Eq. 4.2**)[138]

$$\frac{d(\ln C_e)}{dT} = \frac{\Delta H_x}{RT^2} \qquad 4.2$$

Where; C_e = equilibrium concentration of adsorbate

T= Temperature (K)

R= Universal gas constant

ΔH_x= enthalpy change

Isosteric heat of adsorption is very important as it can be used to carry out characterization of the surface adsorbents[131]. It has been proven that an adsorbent is homogeneous if its isosteric heat of adsorption is independent of the amount of adsorbate it adsorbs and heterogeneous if it varies with the amount of adsorbate adsorbed [137]. From the current study, there was no relationship between the amount of adsorbate adsorbed and the isosteric heat **Table Ap 4.1** thus the adsorbents were homogeneous. In addition,

most values for the isosteric heat of adsorption were found to range between 0-59 kcal**,** thus indicating that the adsorption was physisorption[139].

Furthermore, the present data gives the percentage weight (wt%) of adsorbed molecules on various adsorbents, as in **Table Ap 4.1**. This indicated that CLO zeolite, shown in **Fig. 4.3**, has the highest wt% of the adsorbate, 65.84wt%. Therefore, the best adsorbent was selected basing on the wt% since this could give the efficiency of the material for HCB adsorption. This was also considered for other compounds investigated in the current work. Therefore, CLO zeolite is the best material for the separation of HCB. This material has a mass of 17728g/mol and a three-dimensional pore system. Zeolite RWY (second best), compared to CLO, has a smaller mass. This makes it adsorb fewer molecules per cell than CLO. In addition, the fact that some of the adsorbed molecules may escape from the cells makes this material to have a lower wt% than CLO.

Notably, the highest loading shown by CLO zeolite is also attributed to its overall large cavity diameter, 10.06 Å. This diameter enables it to have a higher maximum loading capacity of HCB compound inside its cells. GSA and VSA are also very important factors affecting the loading capacity of HCB on zeolites. This means that if a material has a large mass, comparable GSA and VSA and a larger pore size, it may accommodate many guest molecules[140]. RWY zeolite on the other hand, has a lower mass but a large Di with a large GSA and VSA, giving it a higher wt% capacity (54.23 wt. %) of HCB molecules giving it a second rank as in **Table Ap 4.1**. Zeolite ITV has a larger mass, GSA and VSA with a small Di than the preceding two zeolites. The small Di overrides the other factors and makes it the third in the rank with an uptake capacity of 33.65 wt %. The fourth zeolite in the rank is IFU with a capacity of 32.41 wt%. This is very close to that of ITV zeolite. This is attributed to the fact that ITV has a larger mass than LTA and LTA has a larger Di than ITV, thus bringing uptake efficiency such close. Zeolite LTA with an uptake capacity of 32.31 is ranked the fifth. This value is very close to that of IFU. However, this closeness may be attributed to their almost equal pore sizes. This explains how the different parameter (structural) affects the loading capacity. The variation in mass, GSA, VSA and Di is exhibited among all zeolites in **Table Ap 4.1**, resulting into different uptake capacity of the adsorbate.

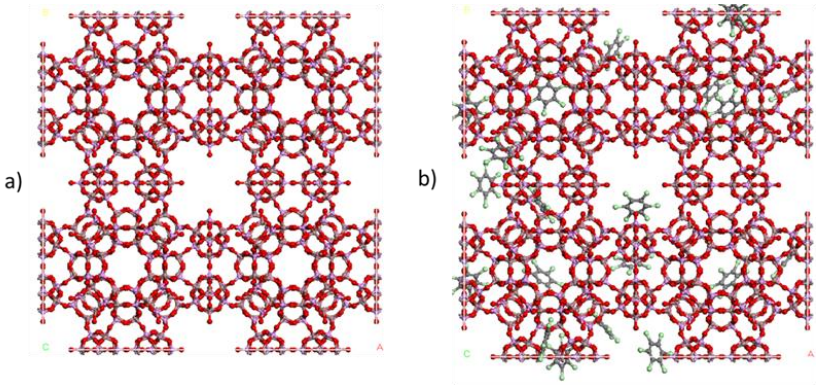

Figure 4.3: *CLO zeolite structures before and after hexachlorobenzene (HCB) uptake, respectively.*

However, if the Di of a material is much larger, it allows a large number of guest molecules into the host material though the efficiency of retention is lowered by escaping molecules. For instance, zeolite TSC with 28 molecules loaded per cell and a Di of 15.87Å has an uptake capacity of 25.69 %wt. The results of this study show that some materials with a Di of zero can still accommodate guest molecules. The zero diameters are attributed to the lack of dimensionality in their pore system. This zero dimension means that the material contains pores in both dimensions, 1D, 2D and 3D, since zero is a basis of everything [141]. In physics and mathematics, a zero-dimensional object or system has no spatial extent in any direction, meaning it lacks any measurable length, width, or height[142]. A zero-dimensional object can be thought of as a point or a particle that has position but no size or volume. In the context of materials science and porous materials, a zero-dimensional pore system refers to a pore structure that does not have a well-defined pore size or dimensionality, meaning it has pores in multiple dimensions (1D, 2D, and 3D), resulting in a pore system with infinite possibilities and characteristics. Their aspect has the following characteristics: they are limitless in both macroscopic and microscopic scales, they can retain their form within the three-dimensional Universe, they can exist both within and outside three-dimensional matters, and they perform the critical function of emitting and perceiving information within the structure of matters[143].

A correlation analysis was done in order to get more understanding of how various structural features affect the uptake capacity since it is evident that HCB compound was adsorbed within the cages in the zeolite, see **Figure 4.3**. The results showed that mass and density were negatively correlated to adsorption capacity (**Figure 4.4a**). This means that a heavier material would have less uptake capacity compared to lighter material. This is logical experimentally as in a measure of equal amount of two substances for different relative masses, with less relative mass, would be quantitative compared to the one with higher relative mass. This means that the more quantitave (large mass) material would have more adsorption sites than the less quantitative (smaller mass) one. Similarly, the density is negatively correlated to adsorption capacity (**Figure 4.4b**). This is due to the fact that density of a material is mass per unit volume meaning that it follows same ideas as mass. On the other hand, HVF, APV, VSA, GSA and Di are positively correlated to wt% (**Figure 4.4 c-h**). However there is a strong positive correlation between APV and wt% compared to other parameters with positive correlation. This implys that accessible pore volume plays a key role to the adsorption capacity of hexachlorobenzene on zeolites.

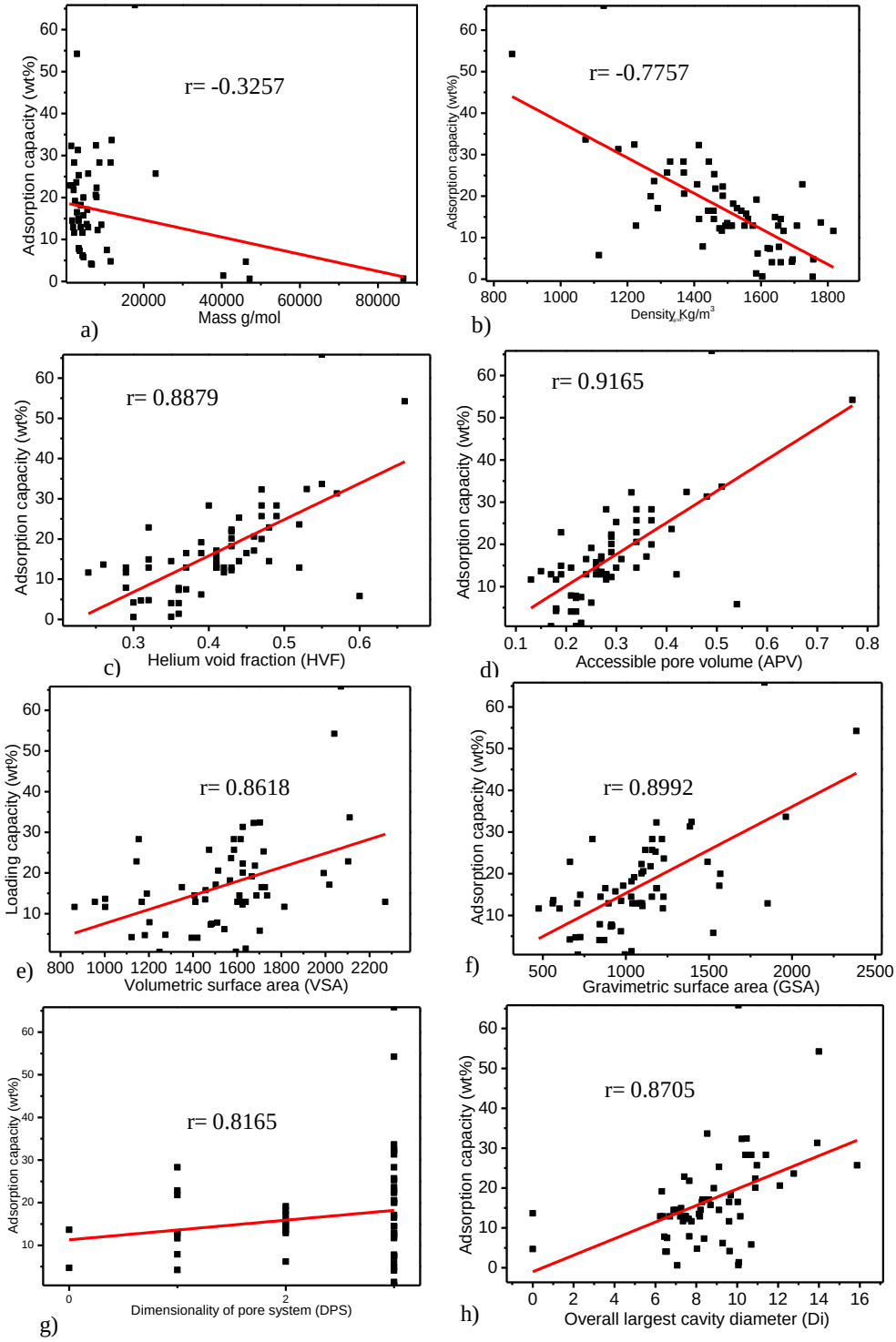

Figure 4.4: *a,b,c,d,e,f,g,h Correlation between zeolites structural parameters; mass, density, HVF, APV, VSA, GSA DPS, Di and adsorption capacity (wt%).*

Experimentally, previous research have also pointed out the effect of structural features of zeolites on adsorption. For instance, Magdalena Wołowiec and co-workers did experimental study on the removal of volatile organic compounds (VOCs) and PAHs by zeolites and surfactant modified[144], and discovered that molar mass of the zeolites and diameter were the major factors which affected the adsorption capacities of these pollutants on zeolites. The present study is agreement with their findings and has further looked into more features as shown in figure 4.4.

Adsorption isotherms were also used to compare the adsorption capacity of adsorbents for HCB. **Figure 4.5** shows the adsorption isotherms of HCB on the best 10 zeolites investigated in this study.

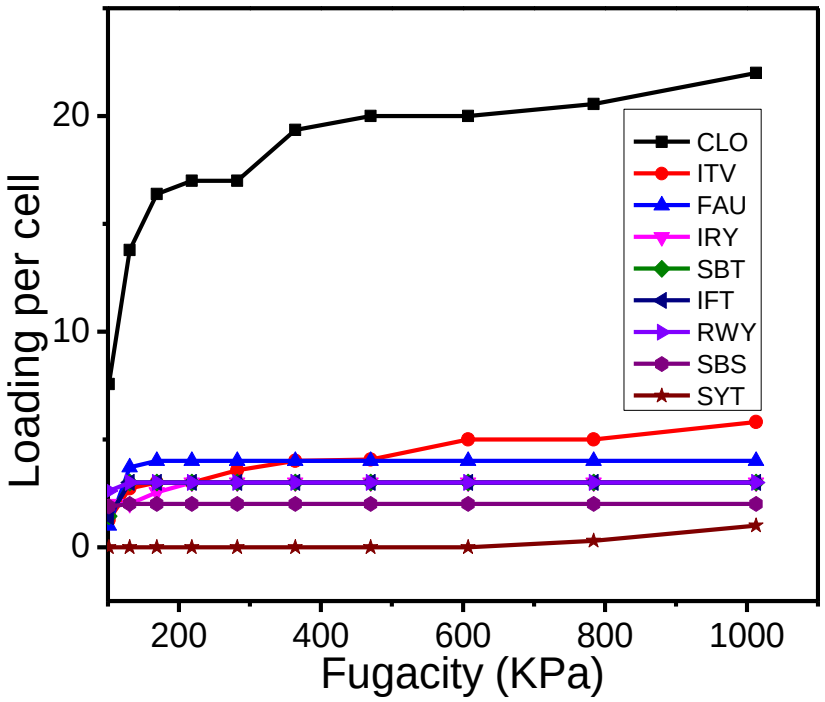

Figure 4.5: *HCB adsorption isotherms on the best performing zeolites.*

It was shown that a fairly rapid rise in adsorbed quantity with increasing pressure up to saturation occurred; thus, they were characterized by a plateau that was nearly horizontal. For this type of isotherms, the site is occupied by one molecule or empty[145] as shown in **Figure 4.3**. It was assumed that any given receptor site can be empty or occupied by one part molecule in accordance with the monolayer model. The grand canonical partition function in this case, for only one site, has the form as shown in **Eq. 4.3**

grand canonical partition function, $Z_{gc} = 1 + e^{\beta(\varepsilon+\mu)}$ 4.3

Where ε is the magnitude of the adsorption energy level of one receptor site, μ is the chemical potential, and β is the Boltzmann factor (1.380649 × 10−23 joule per kelvin). Using the definition of the adsorbed quantity expression against the concentration of the adsorbed molecules, we obtain the formula in **Eq. 4.4**

$$N_a = \frac{nN_M}{1 + \left(\frac{C_{1/2}}{C}\right)^n} \quad 4.4$$

Where n is the number of adsorbed molecule(s) per site, N_M is the receptor site density, N_a is the adsorbed quantity and $C_{1/2}$ is the concentration at half saturation. The parameter $C_{1/2}$ is related to the adsorption energy as reported by Lamine and Bouazra[146,] Khalfaoui et al [145] by the **eq. 4.5**;

$$C_{1/2} = \beta P_{vs} e^{\frac{-\Delta E_a}{RT}} \quad 4.5$$

Where P_{vs} is the saturated vapor pressure, R is the ideal gaseous constant, and T is the room temperature. $-\Delta E_a$ is the molar adsorption energy from the dissolved state. **Eq. 4.5** takes the following form in the case of a liquid system,

$$C_{1/2} = C_s e^{\frac{-\Delta E_a}{RT}} \quad 4.6$$

Where C_s is the solubility of the adsorbate. We can note that the adsorption is governed by a law similar to that of Fermi and Dirac [147, 148] since the site is empty or occupied by only one molecule. If we take n equal to unity, we obtain the expression of Langmuir which is usually used to model this type of isotherm. This model was established by Lamine and Bouazra[146] and was enough to model this type of isotherms.

The stoichiometric coefficient n describes and interprets the adsorption equilibrium. Khalfaoui and his collaborators[145] showed that the higher the concentrations, ($C>C_{1/2}$) the higher n is, and the less important the adsorbed molecule quantity is. For low concentrations, the inverse phenomenon occurs; i.e., when n decreases, the anchorage number, which is defined as the inverse of n, increases, so it is more difficult to find a great number of empty sites near saturation at the same time. The steric coefficient N_M is related to the adsorbed quantity at saturation $N_{a\,sat}$ by the expression in **Eq. 4.7**;

$$N_{a\,sat} = N_M n N_{i\,max} \quad 4.7$$

Where Na sat is the quantity adsorbed at saturation; Nm is the steric coefficient; n is the stoichiometric coefficient; and N_i max is the layer number.

In equation 4.7, for fixed n and Ni max parameters, the increase of N_M can improve the adsorption capacity at saturation. The energetic parameter $C_{1/2}$ is closely related to the adsorption energy level. It is shown by Khalfaoui et al[149] that at a fixed concentration value, the lower $C_{1/2}$ is, the higher the adsorbed quantity is. This fact is valuable for all concentration values far from the saturation. So, we can conclude that the receptor sites which have the stronger energy will be rapidly and easily occupied. Experimental isotherms that possess the shape similar to the one obtained in this study is the one for the case of adsorption of iodine from aqueous potassium iodine solution on zinc chloride activated carbons [150] and the adsorption of ethane on Ajax activated carbons [149].

Further investigations were done to deeply understand the adsorption mechanisms for the best and the least loading zeolites and the results are shown in **Figure 4.6**. For the best performing zeolites CLO and TSC, the adsorption sites are distributed evenly throughout the framework. These sites are attributed to the number of oxygen atoms which are the active sites providers. However, for the least performing zeolites, the active sites are specifically distributed as shown in **Figure 4.6 c** and **d**. For comparison, the adsorption of DDT and HCH was also studied. From our findings, the adsorption of DDT and HCH also follows the same mechanisms as discussed for HCB. It therefore indicates that for OCPs the process that takes place does not involve bond formation as the molecules are attached on the surface of the zeolites and in the cages of the zeolite. The adsorption thermodynamics for OCPs, **Figure Ap 4.2a**, follows pseudo second order kinetic plots. The pseudo second order mechanism is however presumed for lower concentrations of the pollutant, the reaction mechanism may switch to pseudo second order under high concentrations of the pollutant.

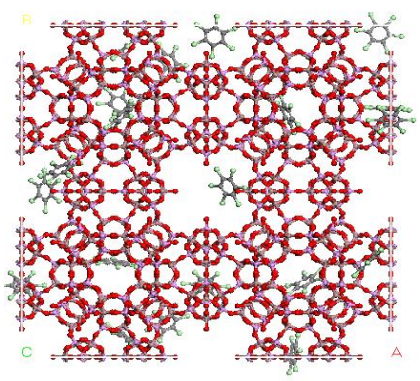

a) Adsorption sites for HCB on CLO

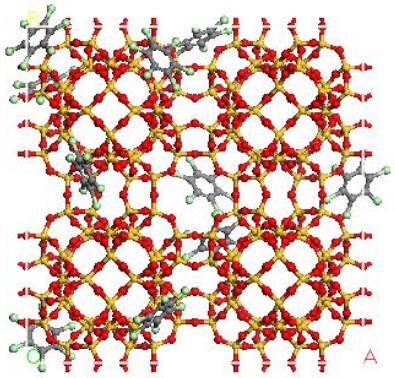

b) Adsorption sites for HCB on TSC

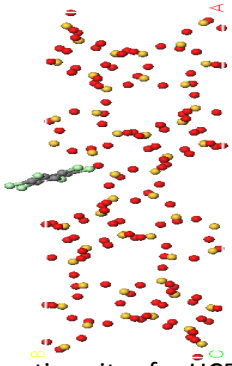

c) Adsorption sites for HCB on IWW

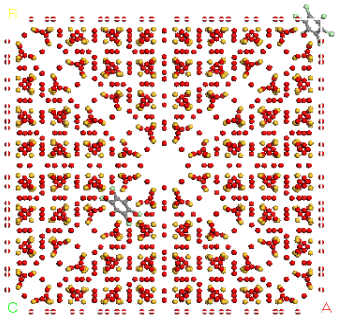

d) Adsorption sites for HCB on MWF

Figure 4.6: *a,b,c,d Adsorption sites for hexachlorobenzene (HCB) for the best a, b and the worst c, d zeolites.*

4.2 Adsorption of chlorinated paraffins (CPs)

The adsorption results in this study for the selected CPs show that zeolite CLO could offer the best adsorbent for separation of CPs from water. From **Tables 4.7 – 4.9**, the loading results for the studied MCCPs are 21, 22, and 19 molecules per cell on CLO zeolite for hexachlorotetradecane ($C_{14}H_{24}Cl_6$), heptachlorotetradecane ($C_{14}H_{23}Cl_7$) and Octachlorotetradecane ($C_{14}H_{22}Cl_8$) respectively with the adsorption energies of -124, -239 and -102 kcal/mol.

Table 4.7; *Loading of hexachlorotetradecane on selected zeolites, activation energies (Ea) and isosteric heats at a temperature of 298K and a pressure range of between 101.325KPa and 1013KPa*

S/NO	ZEOLITE	LOADING	TOTAL ENERGY	ISOSTERIC HEAT	TIME
1	CLO	21	-124.893	50.592	1280
2	ITV	6	-46.723	47.492	619
3	TSC	5	-65.981	55.592	321
4	FAU	5	-95.849	58.792	417
5	IFT	5	-108.903	61.892	210
6	IRY	4	-68.593	58.492	395
7	RWY	4	-47.078	56.792	263
8	SBT	3	-72.463	55.992	314
9	SYT	2	-40.867	52.592	212
10	EMT	2	-51.185	57.292	302
11	SBS	2	-49.348	56.092	352
12	DFO	1	-7.252	48.092	519
13	LTA	0	0	-	20
14	LTN	0	0	-	18
15	MWF	0	0	-	20

Table 4.8*: Loading of heptachlorotetradecane on selected zeolites, activation energies (E_a) and isosteric heats at a temperature of 298K and a pressure range of between 101.325KPa and 1013KPa*

S/NO	ZEOLITE	LOADING	TOTAL ENERGY	ISOSTERIC HEAT	TIME
1	CLO	22	-239.367	52.292	1080
2	ITV	6	-81.929	54.092	719
3	FAU	4	-118.522	61.592	201
4	IRY	3	-63.711	58.692	337
5	SBT	3	-101.693	62.292	222
6	IFT	3	-73.767	60.692	365
7	RWY	3	-51.286	50.892	216
8	SBS	2	-64.237	60.992	324
9	SYT	1	-13.426	40.992	362
10	DFO	1	-28.128	55.992	312
11	EMT	1	-27.691	56.192	342
12	TSC	0	0	-	18
13	LTA	0	0	-	20
14	LTN	0	0	-	20
15	MWF	0	0	-	20

Table 4.9: *Loading of Octachlorotetradecane on selected zeolites, activation energies (E_a) and isosteric heats at a temperature of 298K and a pressure range of between 101.325KPa and 1013KPa*

S/NO	ZEOLITE	LOADING	TOTAL ENERGY	ISOSTERIC HEAT	TIME
1	CLO	19	-102.471	56.292	1150
2	ITV	6	-10.882	57.292	329
3	FAU	4	-74.751	60.492	231
4	IFT	4	-65.356	61.892	417
5	IRY	3	-39.851	61.292	242
6	RWY	3	-22.947	57.392	385
7	SBT	2	-41.968	60.492	223
8	EMT	2	-43.618	69.192	376
9	SBS	2	-42.093	60.792	318
10	TSC	1	-6.284	45.292	352
11	SYT	1	-11.836	51.292	322
12	DFO	1	-16.652	56.592	418
13	LTA	0	0	-	20
14	LTN	0	0	-	20
15	MWF	0	0	-	20

The isosteric heats for this group of compounds were found to be higher than OCPs. This could be attributed to a greater number of atomistic composition of adsorbates. See **Figure Ap 4.12 (a).** Similarly, the studied SCCPs (shown in **Figure Ap 4.12** (b)), were hexachlorodecane, heptachlorodecane and octachlorodecane which had a total loading of 47, 30 and 22 molecules per cell, respectively, on CLO zeolite, as in **Table 4.10**, **4.11, and 4.12**. From these results the trend indicates that an increase in the number of chlorine atoms in the structure of the sorbate, which increases the number of chlorine carbon bonds, reduced the loading into the zeolites. This could be attributed to the increase in size of the sorbate material which makes it quite difficult for the sorbate to access the active adsorption sites.

On the other hand, the results in **Table 4.10. 4.11. and 4.12** based on the best zeolite shows that with addition of chlorine molecules in the sorbate structure would reduce the isosteric heat of adsorption.

Table 4.10: *Loading of hexachlorodecane on selected zeolites, activation energies (E_a) and isosteric heats at a temperature of 298K and a pressure range of between 101.325KPa and 1013KPa*

S/NO	ZEOLITE	LOADING	TOTAL ENERGY	ISOSTERIC HEAT	TIME
1	CLO	47	-2.007	52.692	1120
2	TSC	12	383.581	41.092	314
3	FAU	8	-45.199	59.092	222
4	ITV	7	51.257	39.592	318
5	IFT	7	-16.431	51.592	218
6	RWY	6	22.343	48.992	336
7	IRY	5	3.74	52.092	203
8	SBT	4	-29.235	53.492	384
9	SBS	4	-19.701	53.892	362
10	SYT	3	-4.741	45.692	342
11	DFO	3	-15.656	53.292	322
12	EMT	3	-8.952	46.692	618
13	LTA	0	0	-	20
14	LTN	0	0	-	19
15	MWF	0	0	-	20

Table 4.11: *Loading of heptachlorodecane on selected zeolites, activation energies (E_a) and isosteric heats at a temperature of 298K and a pressure range of between 101.325KPa and 1013KPa*

S/NO	ZEOLITE	LOADING	TOTAL ENERGY	ISOSTERIC HEAT	TIME
1	CLO	30	-109.095	53.092	1186
2	ITV	10	-62.863	51.092	312
3	TSC	9	-106.52	42.192	228
4	IFT	7	-108.827	56.292	316
5	FAU	6	-108.921	54.292	230
6	IRY	5	-62.2	53.692	338
7	RWY	5	-45.178	50.392	215
8	SYT	4	-60.1	51.492	384
9	SBT	3	-61.991	50.392	382
10	DFO	3	-52.859	50.792	332
11	EMT	3	-50.97	55.592	342
12	SBS	2	-38.222	49.192	538
13	LTA	0	0	-	20
14	LTN	0	0	-	20
15	MWF	0	0	-	20

Table 4.12: *Loading of octachlorobenzene on selected zeolites, activation energies (E_a) and isosteric heats at a temperature of 298K and a pressure range of between 101.325KPa and 1013KPa*

S/NO	ZEOLITE	LOADING	TOTAL ENERGY	ISOSTERIC HEAT	TIME
1.	CLO	22	-189.342	45.292	1160
2.	ITV	7	-124.868	58.592	369
3.	FAU	6	-165.267	59.892	231
4.	RWY	5	-103.055	55.892	357
5.	IRY	4	-77.559	51.792	312
6.	IFT	4	-97.07	54.392	375
7.	SBT	3	-80.387	51.092	223
8.	SYT	3	-75.124	55.192	334
9.	EMT	2	-49.472	48.992	392
10.	SBS	2	-60.742	56.192	352
11.	DFO	1	-19.717	50.892	312
12.	TSC	0	0	-	20
13.	LTA	0	0	-	20
14.	LTN	0	0	-	20
15.	MWF	0	0	-	20

The adsorption mechanisms as illustrated by **Fig. Ap 4.6** clearly shows that the sorption of MCCPs on zeolites is physical, similar to SCCPs as in **Figure Ap 4.118**. There is no bond formation in the process. The oxygen atoms provide the active sites for adsorption as shown by **Figure 4.10**. There are electrostatic attraction forces between the chlorine and oxygen atoms. This means that the presence of oxygen atoms in the zeolite structure is of great importance for adsorption. The thermodynamics of CPs adsorption on zeolites follow a pseudo second order as shown in **Figure Ap 4.2**, (d) for MCCPs and (b) for SCCPs**.** The adsorption isotherms for CPs revealed two types of behavior on different zeolites. For instance, octachlorotetradecane displays an H-shaped adsorption isortherm with CLO and step wise isotherms with other zeolites (**Figure 4.7**).

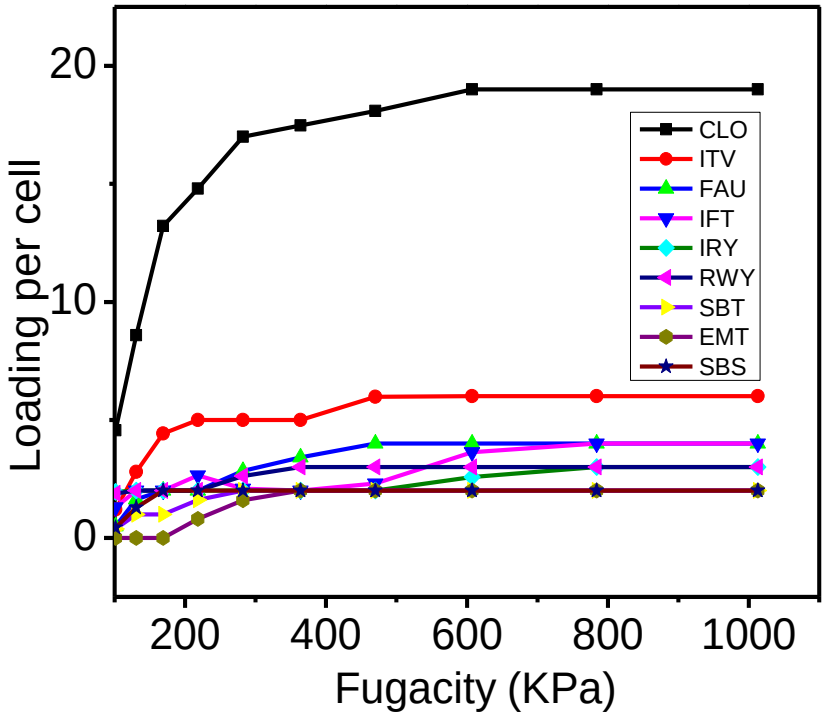

Figure 4.7: *Adsorption isotherms for octachlorotetradecane on various zeolites.*

From **Fig. 4.8** a and b show the best two zeolites for MCCP adsorption has, like OCPs, adsorption sites distributed evenly throughout the framework. However, the least adsorbing material has less adsorption sites which are at specific locations as shown in **Fig. 4.7** c.

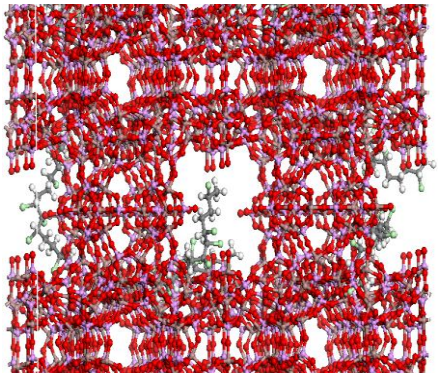

a) Loading of hexachlorodecane on CLO

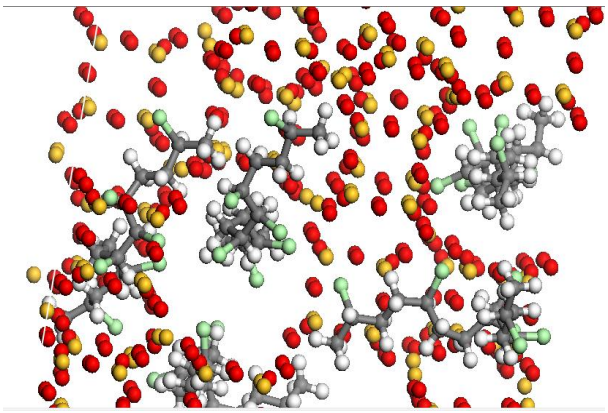

b) Loading of hexachlorodecane on ITV

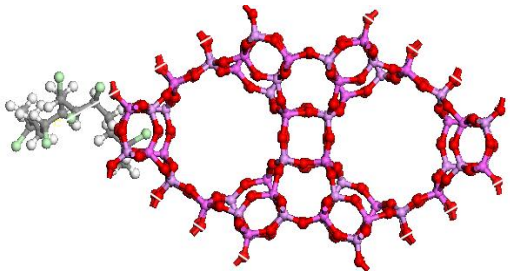

c) Loading of hexachlorodecane on DFO

Figure 4.8: *Adsorption sites for Medium-Chain Chlorinated Paraffins (MCCPs).*

4.3 Adsorption of polycyclic aromatic hydrocarbons (PAHs)

In this current study, the adsorption of selected PAHs was investigated. The results show that among the zeolites studied, zeolite CLO had the highest removal of 132, 105 and 167 molecules per cell for Phenanthrene, Fluoranthene and Acenaphthylene, respectively. This is shown in tables Ap 4.4, 4.5 and 4.6. Despite CLO showing potential ability for application, the process involving PAHs studied here requires much heat from the environment. This makes it less economical than the other zeolite which releases the heat into the environment. Interestingly among the 15 zeolites investigated for PAHs separation, a good number of them involved exothermic process. These include zeolites FAU, IFT, SBT, LTA, SYT, LTN and EMT. This is for acenaphthylene adsorption. However, the rest of the zeolites indicated endothermic adsorption process for PAHs studied in this work **(see Table 4.4, 4.5, 4.6).** The structure of PAHs studied here comprises of carbons and hydrogen atoms. This therefore enabled assessment of adsorption mechanisms basing on the number of carbon atoms. It was then found that for

group of pollutants, increasing the number of carbon atoms reduces the number of adsorbed molecules. From **Tables 4.5-4.6,** it is evident that fluoranthene with 16 carbon atoms in its structure has the least number of its molecules being adsorbed in zeolites. However, acenaphthylene with 12 carbon atoms has the highest number of molecules which are adsorbed in zeolites followed by phenanthrene which has 13 carbon atoms. The above results could be attributed to the fact that more atoms in the adsorbate structure increases the size of the adsorbate hence hindering it from accessing the microspores of the adsorbent. It thus clear that even a difference of one atom in the adsorbates structure counts. However, the number of active sites atoms plays a key role in adsorption. For instance, it is evident from the present study that oxygen atoms in zeolites structure provide the active sites for adsorption of organic compounds (**Table 4.13**). As such, CLO zeolite among all the 245 studied zeolites has the highest number of oxygen atoms. This therefore explains why it is having the highest loading for all the organic compounds studied in this work. **Table 4.13** below shows the number of atoms in adsorbates and adsorbents (few selected). The adsorption mechanism involved in this process revealed physical adsorption as demonstrated in the supporting information (F**ig. Ap 4.3**) and the thermodynamics of adsorption showed pseudo second order plots as shown in supporting information (**Fig. Ap 4.2**). Similarly, just like SCCPs, MCCPs and OCPs, oxygen atoms provided the active sites for adsorption. The adsorption isotherm for PAHs shown below reveals that all the studied PAHs compounds had similar behavior during their interactions with all zeolites. They showed H-shaped isotherms with all the zeolites. See **Fig 4.9.**

From figure 4.5, 4.7 and 4.9, it is clear that the adsorption of hexachlorobenzene, octachlorotetradecane and phenanthrene have same site distribution on surface of the zeolites. This evidenced by the shape of the isotherms for the studied zeolites.

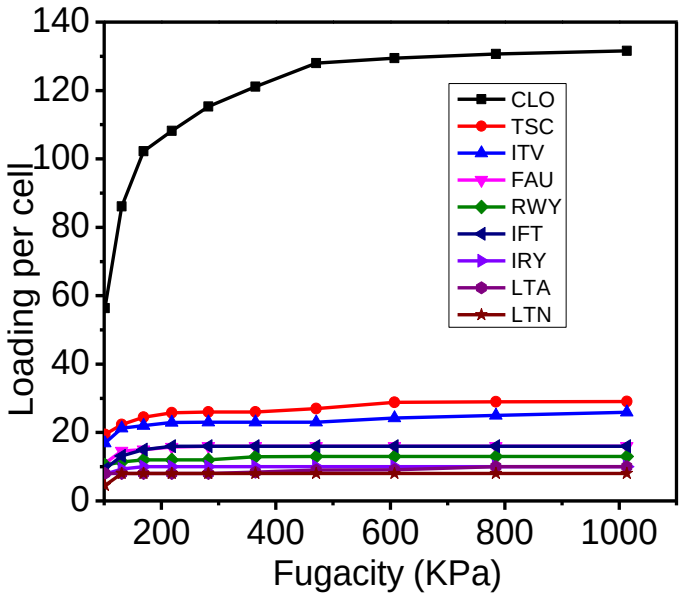

Figure 4.9: *Adsorption isotherms for phenanthrene on various zeolites.*

Table 4.13: *Correlation of oxygen atoms in adsorbate to high pollutant loading rate*

Pollutant	Carbon atoms	Chlorine atoms	Zeolite	No. of oxygen atoms	Reference (Oxygen atoms)	Loading per cell	Average adsorption energy (kcal)
Hexachlnzene	6	6	CLO	5152	[151]	120	-641
			RWY	-	[152]	12	-98
			ITV	379	[153]	21	-130
			IFU	260	[154]	13	-178
			LTA	600	[155]	13	-229
Phenanthrene	14	0	CLO	5152	[151]	132	999
			TSC	897	[156]	30	3
			ITV	379	[153]	26	131
			FAU	624	[157]	16	-3
			IFT	317	[158]	16	-18
Hexachlorotetradecane	14	6	CLO	5152	[151]	21	-124
			ITV	379	[153]	6	-46
			TSC	897	[156]	5	-65
			FAU	624	[157]	5	-95
			IFT	317	[158]	5	-108
Octachlorotetradecane	14	8	CLO	5152	[151]	19	-102
			ITV	379	[153]	6	-10
			FAU	624	[157]	4	-74
			IFT	317	[158]	4	-65
			IRY	154	[152]	3	-39

To justify our data provided in **Table 4.13**, a person's correlation analysis was done. The value of **r** obtained from the linear fit was 0.8 indicating that our data could explain 80% of our findings. This is attributed to the fact there are other available parameters(structural) that could explain the 20%. **See Figure 4.10**.

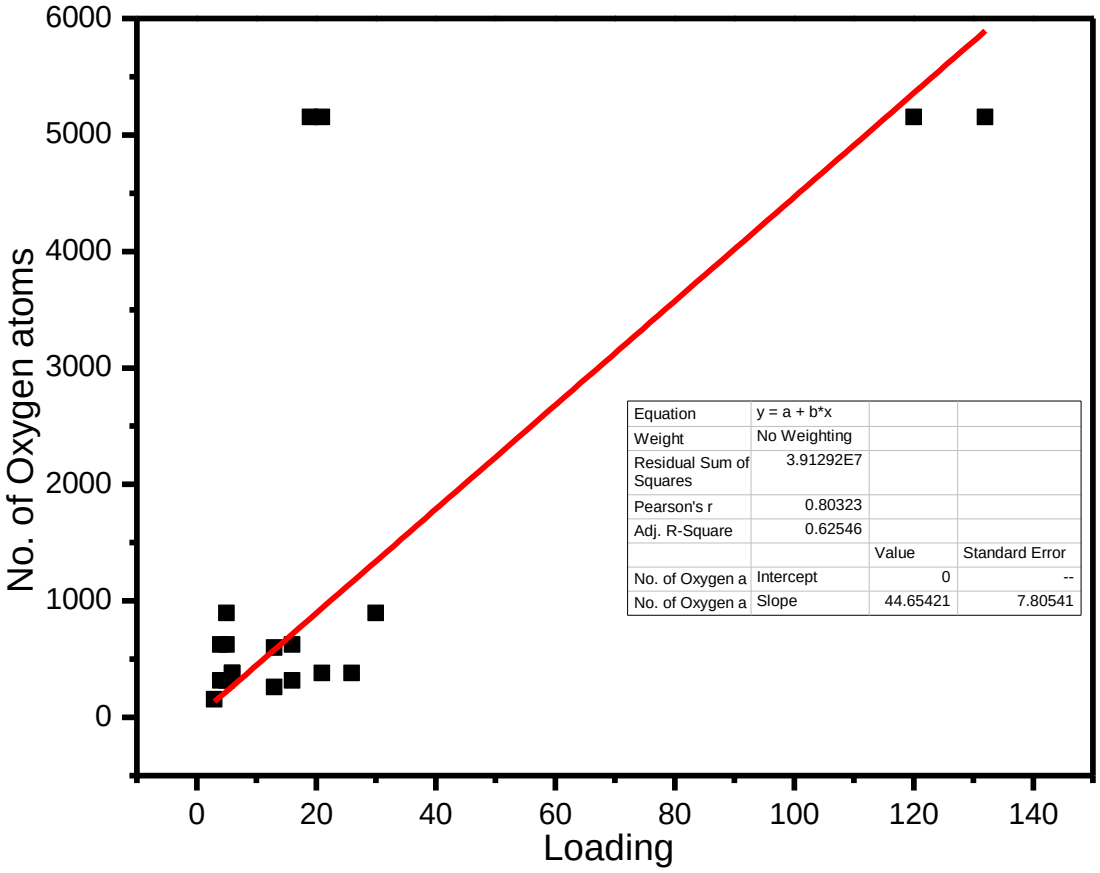

Figure 4.10: *Person correlation plot of oxygen atoms in adsorbate to high pollutant loading rate.*

The experimental research done by Xiaofang You et al[159] on removal of nonylphenol pollutants by Molecular dynamics simulations revealed that the organic pollutants adsorbed on the adsorbent surface through oxygen-containing functional group. This strongly agrees with our present study in which oxygen atoms have played a key role in adsorption of organic pollutants.

4.4 HOMO-LUMO orbitals

We also displayed the contaminants' optimized structures and frontier orbitals, as shown in **Figure 4.11**. The global hardness can be computed using the HOMO orbital energy (E_{HOMO}), which is often correlated with a molecule's ability to donate electrons, and the LUMO orbital energy (E_{LUMO}), which is correlated with a molecule's ability to accept electrons. Lesser energies denote stronger reactivity and lower stability, and the energy difference between HOMO and LUMO also contributes to the description of the chemical behavior and electrical characteristics of molecules. Contrary to the LUMO, which is more evident and concentrated across the entire structure, the HOMO of hexachlorobenzene is localized on the atoms, chlorine, and carbon leaving the bond surfaces. The HOMO is focused on middle atoms in hexachlorotetradecane, similar to the LUMO but more prominent. In hexachlorodecane, the LUMO is localized at one end of the molecule and covers the end with chlorine atoms. The HOMO is located on the center upper part of the molecule and appears on hydrogen and chlorine atoms. In contrast to LUMO, which is concentrated on the entire molecule and covers all the atoms, HOMO in hexachlorocyclohexane is concentrated on the bulk of the atoms while leaving some chlorine and hydrogen atoms unscathed. Similar to LUMO, which is more apparent, heptacholrodecane possesses a confined HOMO spanning chlorine, hydrogen, and carbon atoms at one end. The HOMO orbital for the compound octachlorodecane revolves around the chlorine, hydrogen, and carbon atoms on one end. Contrarily, the LUMO is dispersed, covering the two ends while leaving the center atoms unaffected.

The dichlorodiphenyl trichloroethane's LUMO is situated on the top atoms, which leaves the lower ones empty. The bonds' excretions are likewise not included in the HOMO. On the other hand, all of the atoms, including the bond surfaces, are where the LUMO is concentrated. Like octachlorodecane, heptachlorotetradecane's HOMO is located at one end of the molecule. Similarly, just like octachlorodecane, the HOMO of heptachlorotetradecane is localised at both ends though more pronounced. Finally, octachlorotetradecane has HOMO at the end with distributed chlorine atoms. The other end with closely distributed chlorine atoms is avoided. However, the one carbon atom in the HOMO end with hydrogen atoms but no chlorine is left out. In contrast, the LUMO of

octachlorotetradecane is localized at the opposite end of the molecule with more closely distributed chlorine atom. Similarly, the cabon atom with no chlorine atom is also left unoccupied.

The calculations of the energy levels of the electron orbitals, **Table 4.14**, allowed quantifying the value of the HOMO and LUMO energies, whereby hexachlorodecane has the lowest HOMO energy (- 0.2558 eV) while dichloro diphenyl trichloroethane has a relatively higher HOMO energy (-0.1832 eV).

Table 4.14 *The HOMO LUMO energy values for various studied compounds with calculated HOMO LUMO energy gap.*

Compound	HOMO Energy (eV)	LUMO energy (eV)	HOMO-LUMO energy gap (eV)
Hexachlorodecane	-0.2558	-0.0717	0.1841
Dichloro diphenyl trichloroethane	-0.1832	-0.0777	0.1406
Hexachlorobenzene	-0.2294	-0.0838	0.1456
Hexachlorotetradecane	-0.2341	-0.0389	0.1952
Hexachlorocyclohexane	-0.2553	-0.0776	0.1777
Heptachlorodecane	-0.2427	-0.0515	0.1912
Octachlorodecane	-0.2495	-0.0734	0.1761
Heptachlorotetradecane	-0.2388	-0.0692	0.1696
Octachlorotetradecane	-0.2395	-0.0418	0.1977

These energies are very significant in determining the stability/reactivity and hardness of a molecule. Previous studies have established that the larger the HOMO–LUMO energy gap, the harder and more stable/less reactive the molecule[160,161]. There our results show that octachlorotetradecane has a higher stability. It has relatively a higher chemical hardness of 0.1977 eV, while dichloro diphenyl trichloroethane is less stable and has a relatively low chemical harness of 0.1406 eV.

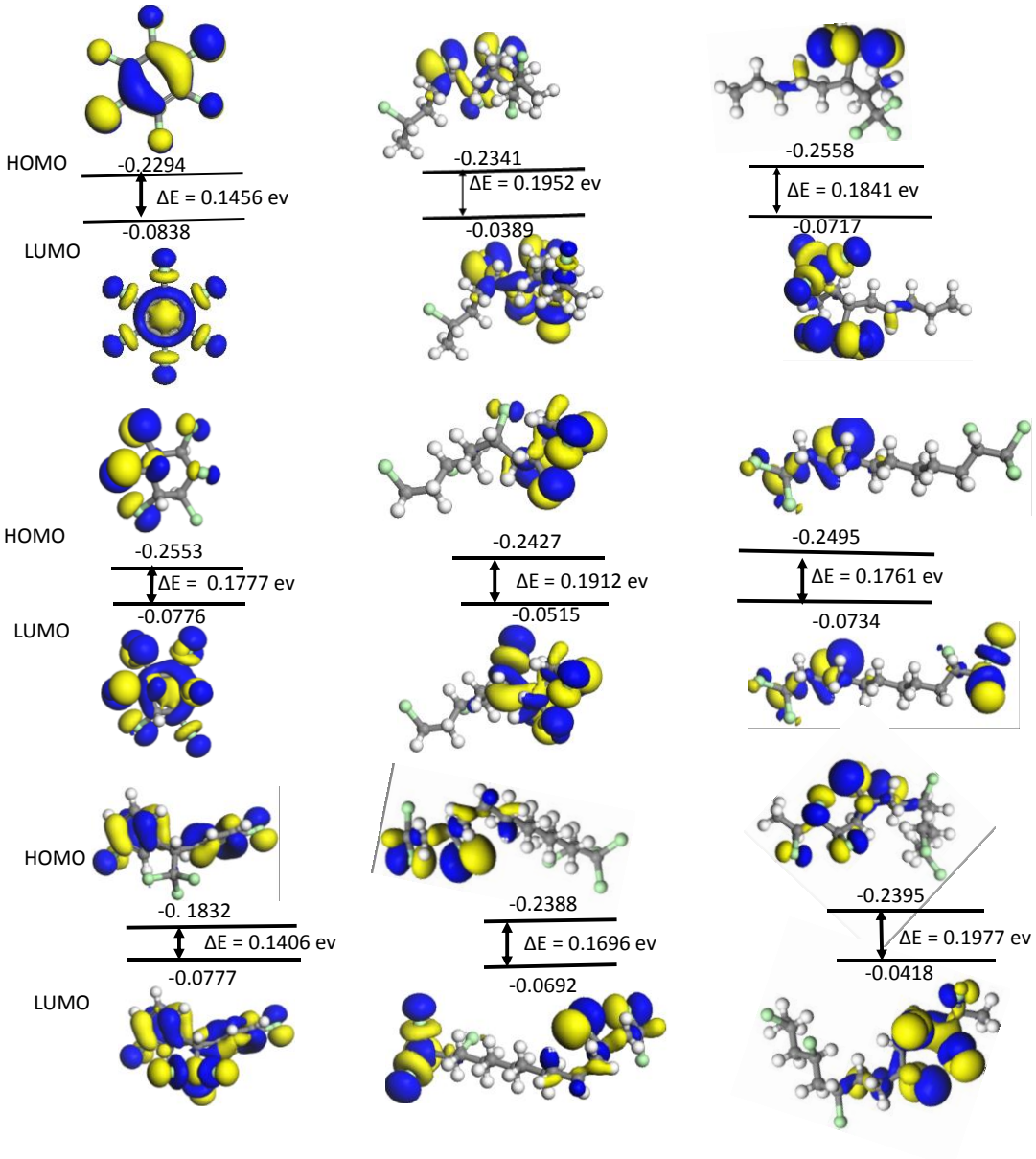

Figure 4.11: *optimized structures of hexachlorobenzene, hexachlorotetradecane, hexachlorodecane hexachlorocyclohexane, heptachlorodecane, octachlorodecane, dichloro diphenyl trichloroethane heptachlorotetradecane and octachlorotetradecane respectively; grey, white and green colors represent carbon, hydrogen and chlorine atoms respectively. Yellow and blue regions correspond to positive and negative values of the orbital.*

4.5 Reaction Pathways

The most stable configuration of the HCB in the CLO zeolite was also identified alongside the corresponding adsorption energies. This is as shown in **Figure 4.12** below

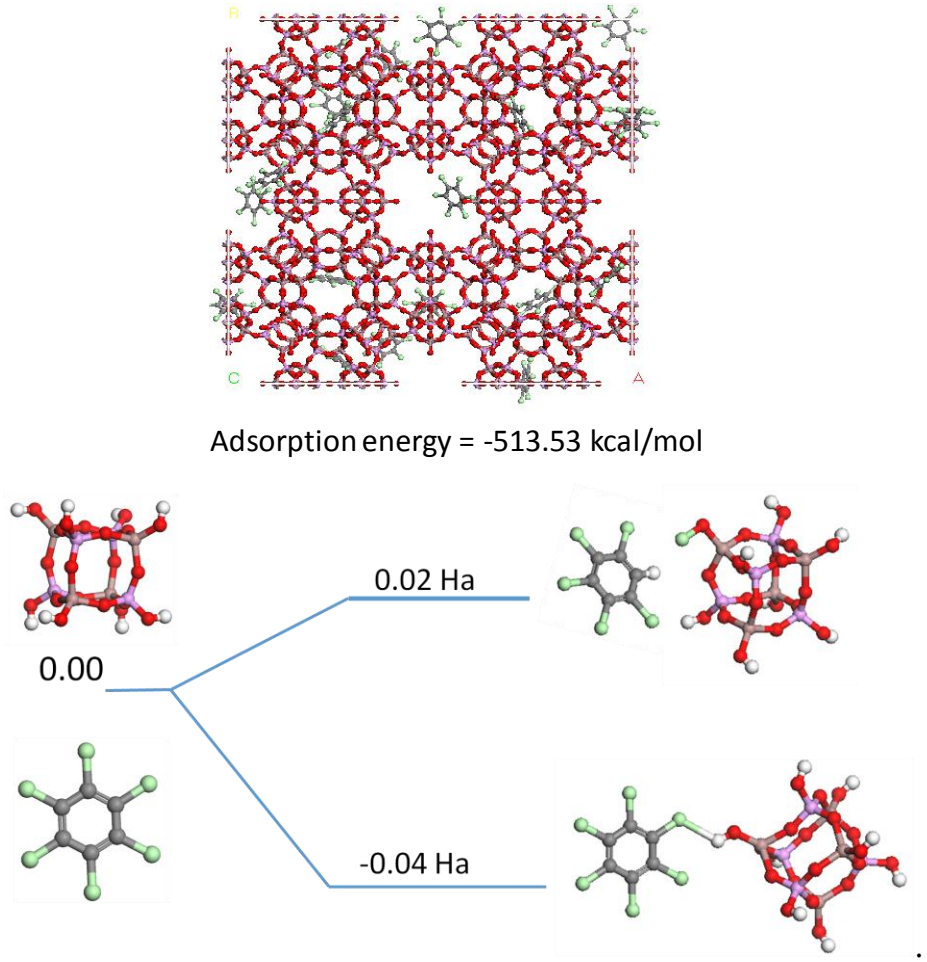

Figure 4.12 *The most stable configuration of hexachlorobenzene adsorbed on CLO zeolite with the corresponding energy; CLO cluster interaction with hexachlorobenene energy and their products energy in predicting the most probable mechanism.*

A system with an adsorption energy of -513.53 kcal/mol was found to be the most stable. To forecast the most stable interactions between HCB and the zeolite, a CLO cluster from the complete structure was obtained in this viewpoint. According to the aforementioned findings, the interaction behavior that showed the least amount of energy shift between the reactants and the product energy was the most appropriate and stable. In that regard, the interaction behavior that involves the bonding of chlorine to oxygen via hydrogen

was the most likely. Gibbs free energy was utilized to identify the most likely path that the reactants would take in addition to the reaction options mentioned above. A rise in the system's entropy would imply a potential spontaneous process in the scenario where the reactants possessed more energy than the products. The process is known as exergonic if the change in Gibb's free energy, G, is negative, which indicates that the process will happen spontaneously.

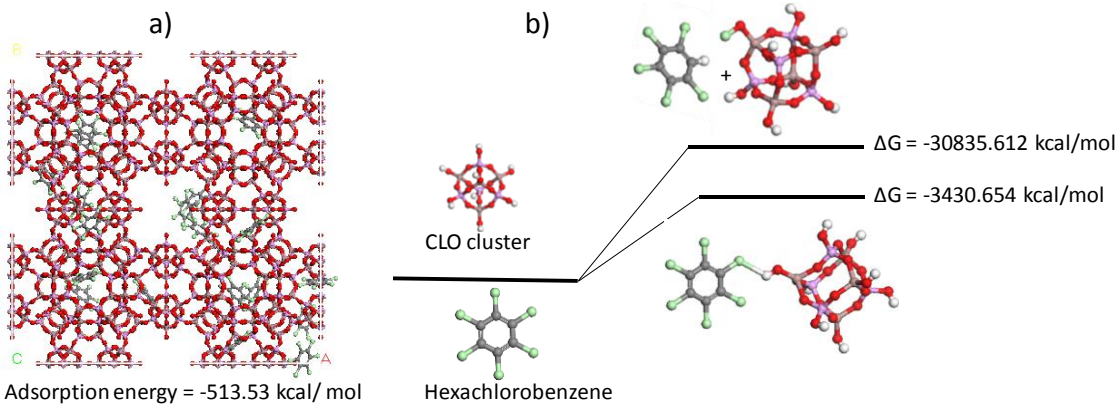

Figure 4.13: *a) Structure of the most stable configuration of hexachlorobenzene adsorbed on the CLO. b) The calculated Gibbs free energy of formation of various products relative to hexachlorobenzene in CLO.*

Most of hexachlorobenzene molecules were seen inside the channels of the zeolite.most of the outer channels were left vacant. This can be a clear indication that the adsorption process for hexachlorobenzene takes place inside the zeolite structure. For the most stable configuration, adsorption energy of -513.53kcal/mol was observed. This highly negative energy clearly indicates the exorthermic nature of the process thus economical. On the other hand, **Figure 4.13 b** shows the calculated Gibbs free energy of formation of various products relative to Hexachlorobenzene in CLO. Differences in Gibbs free energy of formation of various products determine the equilibrium concentration of the various reaction intermediates[162]. In this case the free energy for the reaction between chlorine is smaller compared to the free energy for the reaction of chlorine with oxygen through hydrogen, (-30835.612 kcal/mol vs -3430.654 kcal/mol) respectively. Thus, the interaction between chlorine and oxygen is likely to be suppressed.

4.6. Mulliken charge distribution

Table 4.15: . *Mulliken charge distribution (au) on HCB, CLO and HCB-CLO before and after adsorption calculated from DMOL3 module using medium quality and GGA – PW91 functional.*

HCB (Before adsorption)		**CLO before adsorption**		**HCB - CLO after adsorption**	
C	0.06	Ga	1.296	Ga	1.295
C	0.06	P	1.582	P	1.579
C	0.06	O	-0.817	O	-0.816
C	0.06	O	-0.742	O	-0.757
C	0.06	O	-0.761	O	-0.742
C	0.06	O	-0.752	O	-0.754
Cl	-0.06	O	-0.74	O	-0.75
Cl	-0.06	O	-0.695	O	-0.701
Cl	-0.06	O	-0.744	O	-0.75
Cl	-0.06	Ga	1.298	Ga	1.304
Cl	-0.06	P	1.579	P	1.582
Cl	-0.06	O	-0.815	O	-0.818
		O	-0.76	O	-0.739
		O	-0.744	O	-0.741
		O	-0.754	O	-0.745
		O	-0.76	O	-0.759
		O	-0.699	O	-0.698
		O	-0.748	O	-0.757
		P	1.585	P	1.58
		P	1.578	P	1.583
		Ga	1.301	Ga	1.290
		O	-0.698	O	-0.696
		O	-0.753	O	-0.749
		O	-0.743	O	-0.755
		O	-0.697	O	-0.690
		O	-0.816	O	-0.815
		Ga	1.288	Ga	1.287
		O	-0.816	O	-0.817
		H	0.459	H	0.461
		H	0.423	H	0.425
		H	0.429	H	0.428
		H	0.459	H	0.459
		H	0.429	H	0.435
		H	0.459	H	0.459
		H	0.461	H	0.458
		H	0.430	H	0.425
				C	**0.055**
				C	0.053
				C	0.054
				C	0.053
				C	0.050
				C	0.054
				Cl	-0.037
				Cl	-0.061
				Cl	-0.057
				Cl	-0.055
				Cl	-0.052
				Cl	-0.056

We further analyzed the Mulliken charge distribution on HCB before and after binding on the CLO cluster as shown in **Table 4.15** above. The results showed that before adsorption, the chlorine atoms in the HCB structure have a charge of -0.06 each while carbon atoms have a charge of 0.06 each. Thus before adsorption, chlorine molecule has zero charge, ie it is electrically stable. After adsorption, it is interesting to note that there is a charge transfer between CLO and HCB atom where the chlorine atoms attains a new charge of -0.037, -0.061, -0.057, -0.055, -0.052 and -0.056 while the carbon atoms have a charge of 0.055, 0.053, 0.054, 0.053, 0.050 and 0.054. The net charge on HCB becomes 0.001. On the other hand, the CLO cluster has a charge of 0.002 before adsorption. After adsorption, it attains a charge of 0.001. The values of Mulliken charges suggest that the CLO cluster acts as electron donor while the HCB molecule acts as electron acceptor.

4.7 Effect of doping zeolites to adsorption

An investigation was done into how doping CLO zeolite affected loading capacity. Aluminum, sodium, and silicon are separately exchanged for the phosphorus atoms at various locations with varying symmetrical attributes in the CLO unit cell, and optimization is then carried out. It's noteworthy to notice that the loading of hexachlorobenzene increases from 120 to 133,126 and 127 molecules per cell, respectively, when CLO is doped with aluminum, sodium, and silicon. This is equivalent to 68.0, 67.6, 67.0, 66.8, and 67.0 wt% in terms of weight percent, respectively. It is noted that dopping CLO zeolite provides improved results in terms of both loading and wt%. However among the dopants studied, aluminum provided the best results when an extra frame work is included. The extra framework is used to balance the charges on the aluminum atoms inside the zeolite structure (**see Figure 4.14**). However, Changes in masses and other structural characteristics, such as pore diameters, may be accountable for this improvement in performance. Because silicon, sodium, and aluminum have different atomic radii from gallium atoms, the pore diameters rise. In general, the doping of zeolites led to an increase in the adsorption capacity of hexachlorobenzene. This demonstrates that even for zeolites that perform poorly, altering them through doping can increase the loading of organic contaminants. This is in agreement with the experimental work performed by Magdalena et al. in their study, they suggested that a zeolite with

more defects and impurities in the more accessible mesopores for organic compounds than a pure zeolite.

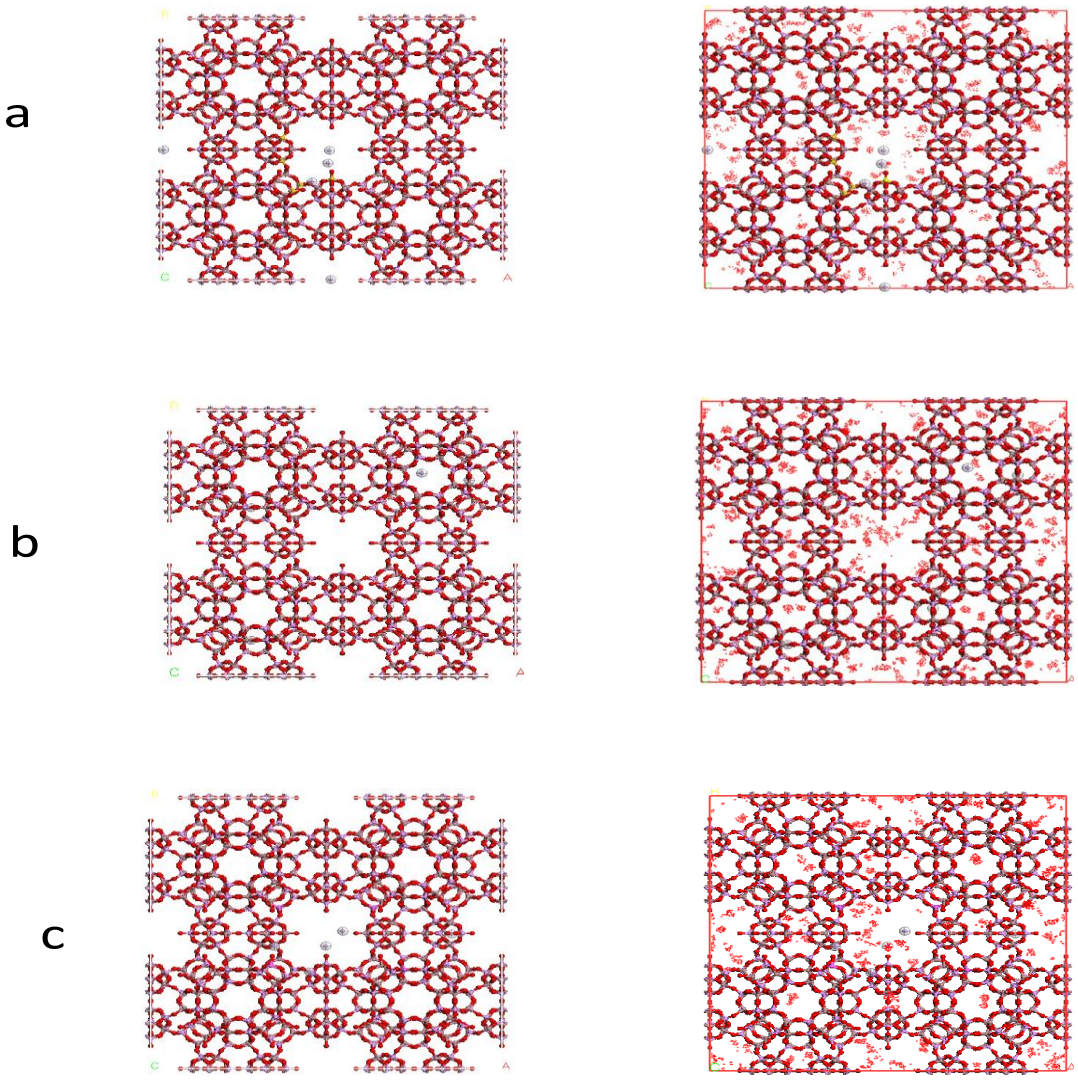

Figure 4.14: *Adsorption capacities of CLO when doped with silicon (a), sodium (b) and Aluminium(c).*

Table 4.16: *Effects of doping on adsorption capacity of CLO zeolite.*

Doping atom	**Loading**	**Wt%**	**Energy (kcal/mol)**	**Isosteric heat (kcal/mol)**
Al with extra framework	133	68.0	-341.178	44.892
Al without extra framework	130	67.6	-317.273	39.292
Si with extra framework	127	67.0	-360.479	127
Si without extra framework	125	66.8	-326.392	124
Na	126	67.0	-362.833	44.992

Table 4.17*: Effect of doping on Mulliken charge distribution (au) on HCB, CLO and HCB-CLO before and after adsorption calculated from DMOL3 module using medium quality and GGA – PW91 functional.*

HCB before adsorption		**doped CLO cluster before adsorption**		**Doped CLO–HCB after adsorption**	
C	0.060	Ga	1.281	Ga	1.19
C	0.060	Al	1.157	Al	1.229
C	0.060	O	-0.717	O	-0.633
C	0.060	O	-0.722	O	-0.613
C	0.060	O	-0.674	O	-0.644
C	0.060	O	-0.686	O	-0.6
Cl	-0.060	O	-0.673	O	-0.649
Cl	-0.060	O	-0.654	O	-0.635
Cl	-0.060	O	-0.691	O	-0.609
Cl	-0.060	Ga	1.246	Ga	1.123
Cl	-0.060	P	1.506	P	1.194
Cl	-0.060	O	-0.713	O	-0.673
		O	-0.677	O	-0.609
		O	-0.684	O	-0.607
		O	-0.733	O	-0.661
		O	-0.713	O	-0.588
		O	-0.647	O	-0.602
		O	-0.677	O	-0.645
		P	1.516	P	1.174
		P	1.511	P	1.174
		Ga	1.273	Ga	1.119
		O	-0.643	O	-0.602
		O	-0.717	O	-0.611
		O	-0.682	O	-0.600
		O	-0.651	O	-0.595
		O	-0.719	O	-0.635
		Ga	1.289	Ga	1.111
		H	-0.717	H	-0.632
		H	0.379	H	0.372
		H	0.374	H	0.369
		H	0.376	H	0.373
		H	0.373	H	0.358
		H	0.37	H	0.438
		H	0.386	H	0.374
		H	0.378	H	0.378
		H	0.376	H	0.371
				C	-0.001
				C	-0.001
				C	0.000
				C	-0.009
				C	-0.036
				C	-0.002
				Cl	0.072
				Cl	0.031
				Cl	0.033
				Cl	0.028
				Cl	0.024
				Cl	0.028

The effect of doping on Muliken charge distribution was investigated (**see Table 4.17**). The charge on each atom before and after adsorption was calculated as 0.060 on each carbon atom and -0.060 on each chlorine atom before adsorption; -0.001, -0.001, 0.000, -0.009, -0.036 and -0.002 for carbon atoms and 0.072, 0.031, 0.033, 0.028, 0.024 and 0.028 for chlorine atoms after adsorption. From **Table 4.17** above, it is noted that, HCB molecule has a zero charge before adsorption just a similar case as in **Table 4.15**. After adsorption, HCB molecule inside the zeolite becomes positively charged with a net charge of 0.167. On the other hand, a doped CLO cluster has a charge of 0.001 before adsorption which defines it as positively charged. After adsorption, it becomes negatively charged with a net charge of -0.096. These Muliken charge values for doped CLO cluster suggest that, for a doped CLO zeolite, its interaction with HCB makes it an electron acceptor while HCB becomes an electron donor. This may be attributed to the fact that aluminium being a trivalent element substitutes phosphorus, which a pentavalent, leaving the material more electronically imbalanced, and hence the need to accept electrons. Thus, it is good to note that charge transfer that takes place between a pure zeolite and HCB is opposite to that of a doped zeolite and HCB.

The energy difference between the reactants and the products when the CLO is doped was further investigated. This was done by substituting phosphorus atom with a single aluminum atom. The interaction between chlorine and oxygen atom in the zeolite through a virtual hydrogen bond showed a higher energy of -12.251116 Ha which is equivalent to -333.37 eV, while the energy of the product involving displacement of chlorine is -12.628273 Ha which is equivalent to -343.6330 eV. These results shows that adsorption of HCB on a doped zeolite would involve displacement of chlorine atom from the compound. This phenomenon is attributed to the fact that doping increases the system energy and this aids in dislocation of chlorine atom from the compound.

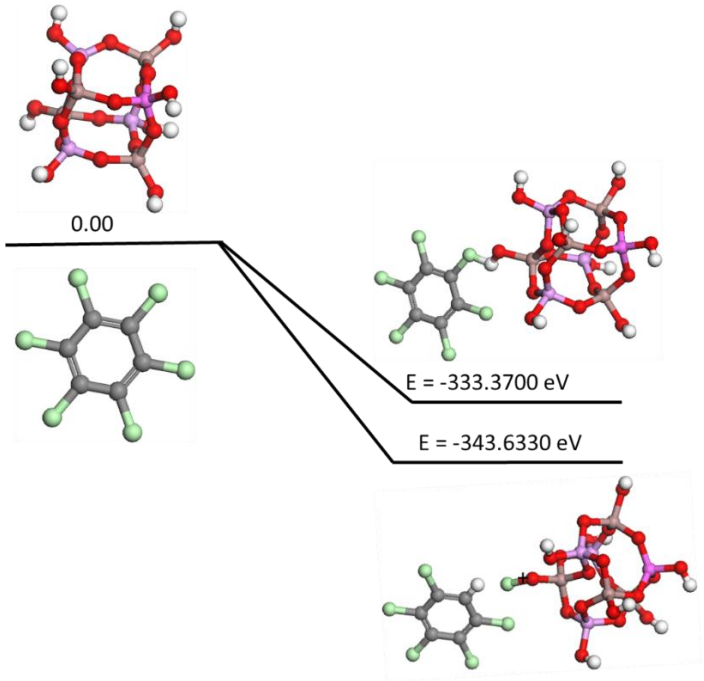

Figure 4.15. *The most stable configuration of hexachlorobenzene adsorbed on doped CLO zeolite with the corresponding energy; doped CLO cluster interaction with hexachlorobenene energy and their products energy in predicting the most probable mechanism*

We further investigated the adsorption isotherm for the dopped CLO and it was evident that, when doped with Aluminum, the zeolite maintains a stepwise isotherm, implying that there exist different types of adsorption sites. On the other hand, doping with sodium changes the adsorption isortherm into an H-shaped isotherm. This simply means that sodium doped CLO material has a higher affinity for Organic pollutants. In addition this could mean also that the sodium makes the CLO zeolite to adsorb like a monolayer and at a low pressure.

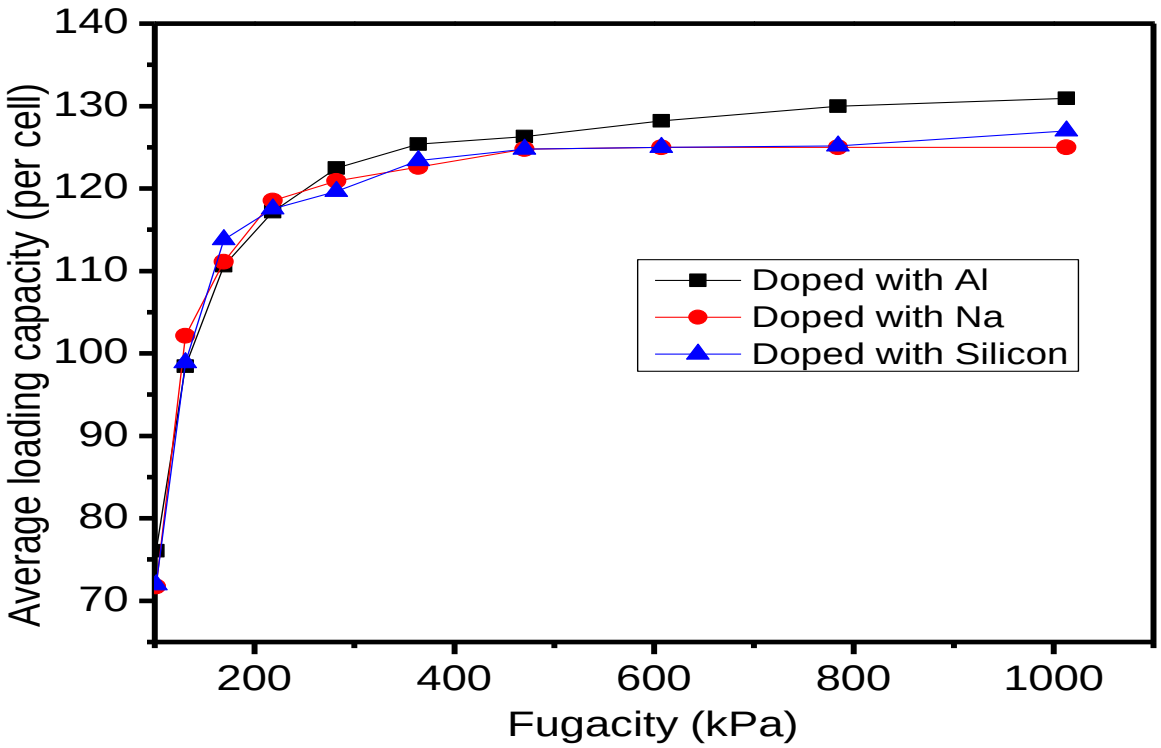

Figure 4.16 : *Effect of doping on adsorption isotherm of zeolite CLO*

4.8 Thermodynamic parameters

Gibb's free energy, entropy, enthalpy and heat capacity were investigated in this study. The results shown in **figure 4.17** below show that the Gibb's free energy decreases with increase in temperature. Gibbs free energy (G) is a measure of the energy available to do useful work in a system at constant pressure and temperature. For a chemical reaction to occur spontaneously, the Gibbs free energy change (ΔG) of the reaction must be negative, indicating that the products have less free energy than the reactants. In other words, the reaction releases free energy and can proceed without the addition of external energy. If ΔG is positive, the reaction is non-spontaneous and requires an input of energy to proceed. If ΔG is zero, the system is in equilibrium, and the reaction neither proceeds forward nor backward. Therefore, Gibbs free energy affects a reaction by determining whether it can occur spontaneously or requires an input of energy to proceed[163]. On the other hand, the entropy of the system for all compounds investigated was noted to increase with increase in temperature. This positive entropy change indicates that there is increase in randomness at the solid-solid interface during adsorption. In addition, the enthalpy of both compounds was noted to increase with increase in temperature leading

to a positive change. See **figure 4.1 a-d** in the appendix and **Table 4.13**. From these results, the adsorption process was found to be spontaneous, feasible and endothermic. The energy of activation calculated by the monte Carlo algorithm, **Table Ap 4.1** was found to range between 0 to 59 which indicated an adsorption process to be physical adsorption. In comparison with the work done by Michael Fischer on Simulation-based evaluation of zeolite adsorbents for the removal of emerging contaminants[164], the values obtained in the current study (0-59 kcal/mol) are closer those from Michael's work (27-46 kcal/mol). The slight difference could be due the structures of the pollutants investigated. However the conclusion from the two studies was that organic pollutants interact with the zeolites through physical adsorption.

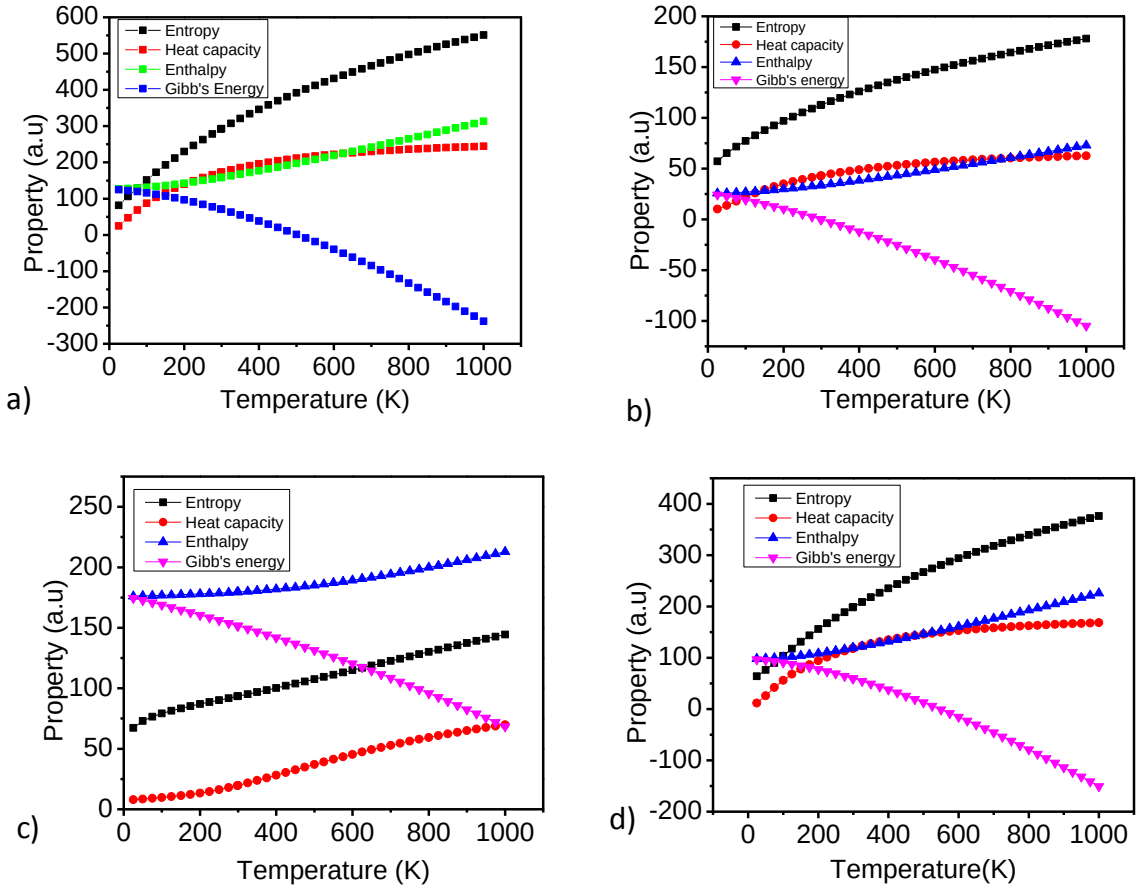

Figure 4.17: *Adsorption thermodynamics of hexachlorobenzene (a), heptachlorodecane (b), heptachlorotetradecane (c) and hexachlorocychlohexane (d) chlorinated pollutants.*

4.8 Extended work on mechanisms of hydrogen storage by zeolites

In order to understand more on adsorption mechanisms of zeolites and whether the mechanisms on liquid adsorption mirrors gas adsorption, a study was carried out on hydrogen adsorption by zeolites. In this particular case, the zeolites with highest hydrogen storage capacity include Linde type A (LTA): 4.8 %wt, JBW: 3.25 % wt, and RTH: 2.89 % wt. The results show that Di, D and M have a negative effect on the percentage weight capacity, while GSA and VSA have the highest positive contribution to the percentage weight. As such, one can improve hydrogen loading capacity of zeolites by reducing the mass and density while increasing both gravimetric and volumetric surface area (**appendix 5**).

4.9 Experimental results

The computational results provide CLO as the best adsorbent for organic pollutants studied. Various mechanisms have been predicted to take place during adsorption process in this study. The adsorption sites have also been predicted. Oxygen atoms have been predicted to provide the active adsorption sites for all the studied compounds. In this section, experiments have been performed using both natural and synthetic zeolites. Each of the adsorbents have been treated special for adsorption process. The aim is to compare the experimental results with computational findings.

The calibration graph, absorbance against concentration is shown in **figure 4.18**. From the graph, a coefficient of determination, R- squared, was used to determine how well the data fit the regression model. The R-squared value from our fit was 0.95898, which shows a good fit. The ratio between the covariance of concentration and absorbance, and the product of their standard deviations, r, was 0.98226. The equation of the calibration tool used is shown below **(eq 4.8**)

$$y = 0.00884x \qquad 4.8$$

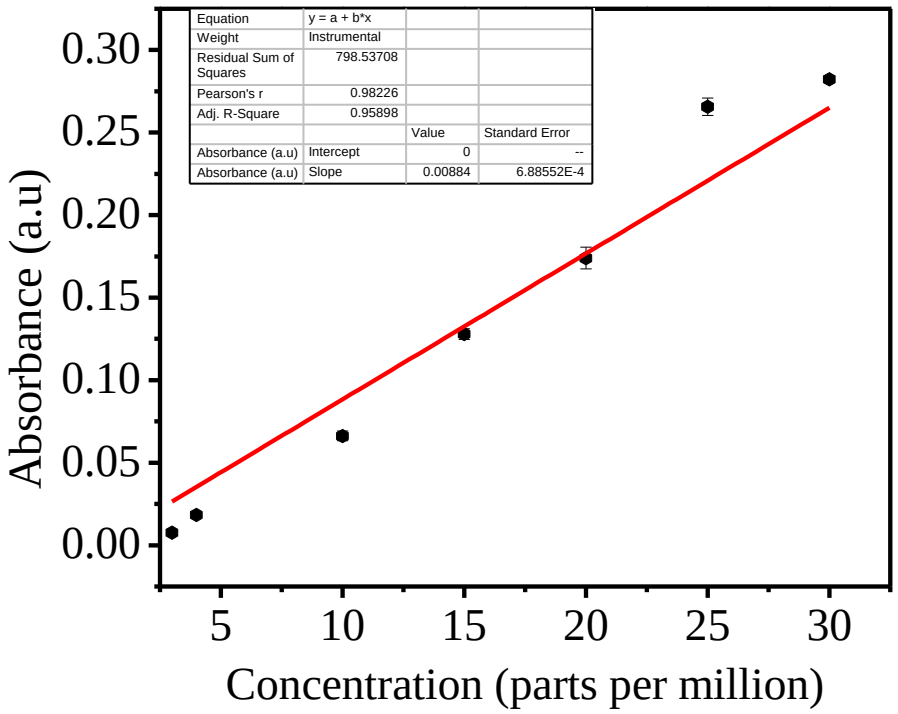

Figure 4.18: *Pearson's correlation between absorbance and HCB concentration.*

From the adsorption results, it was observed that zeolite X, both treated and untreated was less hydrophobic and thus it solidified immediately it came in contact with water. This was due to less Si/Al ratio. This material could therefore not be used for adsorption using columns. However, in order to use it for adsorption in columns, there was a need to increase Si/Al ratio in order to make it hydrophobic. The addition of silica gel to this zeolite in the ratio 5:3 was the most effective way. On the other hand, clinoptilolite zeolite was found to be less hydrophobic and thus it was easy to make a slurry. Thus, there was no addition of silica gel required. However, clinoptilolite zeolite could not be used for adsorption in columns since it clogged inside the column and thus it could not allow water to pass through. This was the case even after mixing with silica gel. A solution to this could therefore be avoiding very fine powdery particles though not investigated in this study. The results provided in this study therefore are the adsorption by treated zeolite x and untreated zeolite x (FAU topology).

Table 4.18: *Absorbance values of a HCB sample adsorbed on zeolite x, (both treated and untreated) and silica gel.*

Material	**Average absorbance of HCB**				
	1	**2**	**3**	**4**	**5**
Treated zeolite x	0.024	0.021	0.002	0.002	0.001
Untreated zeolite x	0.013	0.0085	0.002	0	ND
Silica gel	0.039	0.039	0.038	0.039	0.038

The absorbance values (**Table 4.18**) were used to get related concentrations using **Figure 4.18**. The concentrations of the unknown are reported in **Table 4.19.** From **Table 4.18**, the absorbance values shown are less than the expected values, implying that adsorption took place in all the set ups. However, it is clear that the untreated zeolite x had a higher adsorption capacity compared to the one that had undergone special treatment. This is seen from the absorbance values. It is also clear that the specially treated zeolite becomes saturated easily unlike the treated one. Using the results in **Table 4.18** and the equation of the correlation graph, **equation 4.9.1,** the concentration at every stage is calculated (see **Table 4.19**)

Table 4.19: *The concentration of the pollutant solution at every stage as calculated from the calibration curve.*

Material	**Concentration of HCB**				
	1	**2**	**3**	**4**	**5**
treated zeolite x	2.7149	2.3756	0.2262	0.2262	0.1131
untreated zeolite x	1.4706	0.9615	0.2262	0	ND
silica gel	4.4118	4.4118	4.2986	4.4118	4.2986

From **Table 4.19**, it is evident the concentration after every run in the column packed with silica gel was almost constant, though lower than the expected concentration, 5ppm. For treated zeolite x packed column, the maximum concentration expected was 6ppm and 6.8 ppm for the column packed with untreated zeolite x. These concentrations were calculated from the amount of water that remained in the columns after packing the zeolites. The amount of pollutant concentration removed at every stage was further calculated and this is seen in **Table 4.20**.

Table 4.20: *The pollutant removal capacity at every run stage*

Material	**Removed concentration of HCB**				
	1	**2**	**3**	**4**	**5**
treated zeolite x	3.2851	0.3393	2.149	ND	0.2149
untreated zeolite x	5.3294	0.5091	0.7353	0.2262	N.D
silica gel	0.5882	ND	0.1132	-0.1132	ND

From **Table 4.20**, it is clear that the removal rate for silica gel is very small and thus this could not affect the adsorption capability of zeolites.

The best performing zeolite, untreated zeolite x, was further investigated to find the optimal removal. This was done by using a solution with higher concentration which was run through the column several times until the saturation point was reached.

Table 4.21: *Adsorption capacities for untreated zeolite x*

No. of runs	**1**	**2**	**3**	**4**	**5**
Average absorbance	0.009	0.006	0.005	0.048	0.0046
Concentration (ppm)	1.018	0.679	0.566	0.543	0.515
Amount removed (ppm)	10.982	0.339	0.113	0.023	0.028
Percentage removal	91.5	33.3	16.6	4.1	5.2

The results from **Table 4.21** shows that untreated zeolite x could be reused several times before it gets saturated. However, the percentage removal reduces. The removal capacity was finally calculated using the original concentration and the final concentration. The initial concentration of the solution was 12ppm and the final concentration was 0.515 ppm. From this the removal percentage was calculated as 95.71%. This best performance of untreated zeolite is attributed to presence of terrestrial water which contributes the oxygen atoms. From the simulated results it was clear that the higher the number of oxygen atoms the better the adsorption capability of zeolites for organic pollutants (**see Table 4.13**). Comparing these results with other works that have focused on removal of organic pollutants from water by sorption, the present values are better than the previously reported. This means that the adsorbents used in the present study could offer

a better solution. For instance, Eman Hashim Khader and co-workers[165] used clinoptilolite natural zeolite to eliminate organic pollutants from produced water. They found out that zeolites could remove chemical oxygen demand (COD), oil and turbidity up to 84.8%, 63.8% and 85.06%. This indicates that untreated zeolite X could be applied for better removal of organic pollutants with up 95.71% removal.

CHAPTER FIVE
CONCLUSION AND RECOMMENDATION

5.1 Summary

In this study, the objective was to investigate the thermodynamics and mechanisms of adsorption of organochlorine pollutants on zeolites. The first objective was successfully achieved, with cloverite zeolite identified as the most effective adsorbent for organochlorines. This finding is consistent with the work of Wanyoyi et al.[166], who also found cloverite to be the best adsorbent for pharmaceutical pollutants, demonstrating a maximum adsorption energy of 84 kcal/mol due to strong electrostatic interactions between the pollutants and the zeolites. The favorable mechanism of electrostatic attraction was predicted in this study. To accomplish the first objective, molecular dynamic simulations were employed as the primary tool, with the universal force field yielding the best results for loading pollutants onto zeolites.

This force field has previously been utilized in pharmaceutical adsorption studies[166]. Additionally, it was observed that the adsorption of organic pollutants on zeolites increases with an increase in the number of oxygen atoms in the zeolite structure. This finding is not limited to the organic pollutants investigated in this study, as previous research has reported the adsorption of various organic pollutants on zeolites facilitated by oxygen-containing functional groups[165]. Modifying the structural compositions of zeolites through aluminum doping was found to enhance their adsorption abilities. Charge transfer between the zeolites and the adsorbate was observed during the adsorption process. The simulations also indicated that adsorption followed a pseudo-second-order kinetics at lower concentrations, exhibited physiosorption characteristics, optimized at respective activation energies of the pollutants, and conformed to a Langmuir isotherm model. The second objective of this study, which involved applying the predicted zeolites for adsorption in the laboratory, was successfully achieved. Natural and synthetic zeolites were obtained and activated for use in adsorption columns. The choice of adsorption columns was based on their successful application in the removal of heavy metals from water and waste materials[167]. High silica ratio zeolites were crucial for effective column packing. The addition of silica gel to the zeolite in a 5:3 ratio was

determined to be the most favorable condition. Through sorption experiments, it was found that untreated synthetic zeolite exhibited the highest removal percentage, achieving up to 95% removal. These findings were compared to previous literature to evaluate their significance. In comparison to the experimental work by Eman Hashim Khader and colleagues, who reported a removal ability of up to 85.06% for the selected zeolites, the present research demonstrated a higher removal percentage of up to 95%.

5.2 Conclusion

In conclusion, this research provides a comprehensive investigation into the thermodynamics and mechanisms of organochlorine adsorption on zeolites. The findings align with previous studies, particularly in terms of cloverite zeolite's superior adsorption capacity for both organochlorine and pharmaceutical pollutants. The use of molecular dynamics simulations with the universal force field proved successful, although alternative force fields have also yielded reliable outcomes in related studies. The importance of oxygen atoms in zeolite structures for adsorbing organic pollutants was confirmed, and the enhancement of adsorption abilities through aluminum doping was highlighted. The experimental application of predicted zeolites in adsorption columns achieved exceptional removal capabilities. Overall, this research demonstrates a higher removal percentage and contributes valuable insights into the field of zeolite-based adsorption.

5.3 Recommendations

We recommend the use of untreated zeolite for adsorption of chlorinated compounds. However, other treatment methods other than the one employed in the current study should be investigated.

For computation studies, we recommend the use of high performing computer in order to simulate massive compounds for studies. We further recommend the use of universal force field for organic compounds.

5.4 Recommendation for Further Studies

We recommend further studies to investigate how clinoptilolite zeolite can be used for adsorption in columns without clogging. Hydrophilic nature of various zeolites should be studied.

Other groups of compounds should be simulated in order to classify them with their associated adsorbents.

Further studies should also focus on how other zeolite treatment methods could affect the adsorption of chlorinated compounds.

REFERENCES

1 Cejka, J. Introduction to zeolite science and practice. *E-book accessed at: https://books.google.co.ke/books/about/Introduction_to_Zeolite_Science_and_Prac.html?id=a79yAa9_pH4C&printsec=frontcover&source=kp_read_button&hl=en&redir_esc=y#v=onepage&q&f=false* **Date accessed: 3rd Nov. 2022.** (2007).

2 Wu, W. & Weitz, E. Modification of acid sites in ZSM-5 by ion-exchange: An in-situ FTIR study. *Applied surface science* **316**, 405-415 (2014).

3 Suzuki, I., Oki, S. & Namba, S. Determination of external surface areas of zeolites. *Journal of Catalysis* **100**, 219-227 (1986).

4 Giaya, A., Thompson, R. W. & Denkewicz Jr, R. Liquid and vapor phase adsorption of chlorinated volatile organic compounds on hydrophobic molecular sieves. *Microporous and mesoporous materials* **40**, 205-218 (2000).

5 Pasti, L. *et al.* The role of water in DCE adsorption from aqueous solutions onto hydrophobic zeolites. *Microporous and Mesoporous Materials* **160**, 182-193 (2012).

6 Rossner, A. & Knappe, D. R. MTBE adsorption on alternative adsorbents and packed bed adsorber performance. *Water research* **42**, 2287-2299 (2008).

7 Arletti, R. *et al.* Location of MTBE and toluene in the channel system of the zeolite mordenite: Adsorption and host–guest interactions. *Journal of Solid State Chemistry* **194**, 135-142 (2012).

8 Martucci, A. *et al.* Adsorption mechanism of 1, 2-dichloroethane into an organophilic zeolite mordenite: a combined diffractometric and gas chromatographic study. *Microporous and Mesoporous Materials* **151**, 358-367 (2012).

9 Abu-Lail, L., Bergendahl, J. A. & Thompson, R. W. Adsorption of methyl tertiary butyl ether on granular zeolites: batch and column studies. *Journal of hazardous materials* **178**, 363-369 (2010).

10 Martucci, A. *et al.* Adsorption of pharmaceuticals from aqueous solutions on synthetic zeolites. *Microporous and Mesoporous Materials* **148**, 174-183 (2012).

11 Ötker, H. M. & Akmehmet-Balcıoğlu, I. Adsorption and degradation of enrofloxacin, a veterinary antibiotic on natural zeolite. *Journal of Hazardous Materials* **122**, 251-258 (2005).

12 Braschi, I. *et al.* Removal of sulfonamide antibiotics from water: evidence of adsorption into an organophilic zeolite Y by its structural modifications. *Journal of Hazardous Materials* **178**, 218-225 (2010).

13 Thiebault, T. & Boussafir, M. Adsorption mechanisms of psychoactive drugs onto montmorillonite. *Colloid and Interface Science Communications* **30**, 100183 (2019).

14 Langmi, H. *et al.* Hydrogen storage in ion-exchanged zeolites. *Journal of alloys and compounds* **404**, 637-642 (2005).

15 Du, X. Molecular-Dynamics Simulation of self-diffusion of molecular hydrogen in x-type zeolite. *Journal of Chemistry* **2013** (2013).

16 Nachtigall, P., Delgado, M. R., Nachtigallova, D. & Areán, C. O. The nature of cationic adsorption sites in alkaline zeolites—single, dual and multiple cation sites. *Physical Chemistry Chemical Physics* **14**, 1552-1569 (2012).

17 Torres, F. J., Civalleri, B., Terentyev, A., Ugliengo, P. & Pisani, C. Theoretical study of molecular hydrogen adsorption in Mg-exchanged chabazite. *The Journal of Physical Chemistry C* **111**, 1871-1873 (2007).

18 Palomino, G. T., Carayol, M. L. & Areán, C. O. Thermodynamics of hydrogen adsorption on the zeolite Ca-Y. *Catalysis Today* **138**, 249-252 (2008).

19 Shi, J. *et al.* Preparation and application of modified zeolites as adsorbents in wastewater treatment. *Water Science and Technology* **2017**, 621-635 (2018).

20 Oliveira, L. C., Petkowicz, D. I., Smaniotto, A. & Pergher, S. B. Magnetic zeolites: a new adsorbent for removal of metallic contaminants from water. *Water research* **38**, 3699-3704 (2004).
21 Bouaziz, N., Manaa, M. B., Aouaini, F. & Lamine, A. B. Investigation of hydrogen adsorption on zeolites A, X and Y using statistical physics formalism. *Materials Chemistry and Physics* **225**, 111-121 (2019).
22 Byun, Y., Je, S. H., Talapaneni, S. N. & Coskun, A. Advances in porous organic polymers for efficient water capture. *Chemistry–A European Journal* **25**, 10262-10283 (2019).
23 Omwoma, S. *et al.* Comparative exposomics of persistent organic pollutants (pcbs, ocps, mccps and sccps) and polycyclic aromatic hydrocarbons (pahs) in Lake Victoria (africa) and Three Gorges Reservoir (China). *Science of the Total Environment* **695**, 133789 (2019).
24 Nakhjiri, A. T., Sanaeepur, H., Amooghin, A. E. & Shirazi, M. M. A. Recovery of precious metals from industrial wastewater towards resource recovery and environmental sustainability: A critical review. *Desalination* **527**, 115510 (2022).
25 Abdelrasoul, A., Zhang, H., Cheng, C.-H. & Doan, H. Applications of molecular simulations for separation and adsorption in zeolites. *Microporous and Mesoporous Materials* **242**, 294-348 (2017).
26 Kellouai, W. *et al.* Gas Adsorption in Zeolite and Thin Zeolite Layers: Molecular Simulation, Experiment, and Adsorption Potential Theory. *Langmuir* (2022).
27 Rashed, M. N. Adsorption technique for the removal of organic pollutants from water and wastewater. *Organic pollutants-monitoring, risk and treatment* **7**, 167-194 (2013).
28 Adasme, M. F. *et al.* PLIP 2021: Expanding the scope of the protein–ligand interaction profiler to DNA and RNA. *Nucleic acids research* **49**, W530-W534 (2021).
29 Cavicchioli, R. *et al.* Scientists' warning to humanity: microorganisms and climate change. *Nature Reviews Microbiology* **17**, 569-586 (2019).
30 Rodriguez-Narvaez, O. M., Peralta-Hernandez, J. M., Goonetilleke, A. & Bandala, E. R. Treatment technologies for emerging contaminants in water: A review. *Chemical Engineering Journal* **323**, 361-380 (2017).
31 Henninger, S. K. *et al.* New materials for adsorption heat transformation and storage. *Renewable Energy* **110**, 59-68 (2017).
32 Gomez-Maldonado, D., Erramuspe, I. B. V. & Peresin, M. S. Natural polymers as alternative adsorbents and treatment agents for water remediation. *BioResources* **14**, 10093-10160 (2019).
33 Satoh, A. *Introduction to practice of molecular simulation: molecular dynamics, Monte Carlo, Brownian dynamics, Lattice Boltzmann and dissipative particle dynamics*. (Elsevier, 2010).
34 Lísal, M., Smith, W. R. & Kolafa, J. Molecular simulations of aqueous electrolyte solubility: 1. The expanded-ensemble osmotic molecular dynamics method for the solution phase. *The Journal of Physical Chemistry B* **109**, 12956-12965 (2005).
35 Plazinska, A. & Plazinski, W. Comparison of Carbohydrate Force Fields in Molecular Dynamics Simulations of Protein–Carbohydrate Complexes. *Journal of chemical theory and computation* **17**, 2575-2585 (2021).
36 Wang, H., Zhang, L., Han, J. & Weinan, E. DeePMD-kit: A deep learning package for many-body potential energy representation and molecular dynamics. *Computer Physics Communications* **228**, 178-184 (2018).
37 Dawes, R. & Quintas-Sánchez, E. The construction of ab initio-based potential energy surfaces. *Reviews in Computational Chemistry* **31**, 199-263 (2018).

38 Zhang, L., Han, J., Wang, H., Saidi, W. & Car, R. End-to-end symmetry preserving inter-atomic potential energy model for finite and extended systems. *Advances in neural information processing systems* **31** (2018).
39 GONG, J.-O. A Harmonic Oscillator Universe. *AAPPS Bulletin* **28** (2018).
40 Lu, Z., Zhou, N., Wu, Q. & Zhang, Y. Directional dependence of hydrogen bonds: A density-based energy decomposition analysis and its implications on force field development. *Journal of chemical theory and computation* **7**, 4038-4049 (2011).
41 Weiner, P. K. & Kollman, P. A. AMBER: Assisted model building with energy refinement. A general program for modeling molecules and their interactions. *Journal of Computational Chemistry* **2**, 287-303 (1981).
42 Halgren, T. A. Merck molecular force field. II. MMFF94 van der Waals and electrostatic parameters for intermolecular interactions. *Journal of Computational Chemistry* **17**, 520-552 (1996).
43 Visscher, K. M. & Geerke, D. P. Deriving force-field parameters from first principles using a polarizable and higher order dispersion model. *Journal of chemical theory and computation* **15**, 1875-1883 (2019).
44 Cornell, W. D. *et al.* A second generation force field for the simulation of proteins, nucleic acids, and organic molecules. *Journal of the American Chemical Society* **117**, 5179-5197 (1995).
45 Graen, T., Hoefling, M. & Grubmüller, H. AMBER-DYES: characterization of charge fluctuations and force field parameterization of fluorescent dyes for molecular dynamics simulations. *Journal of Chemical Theory and Computation* **10**, 5505-5512 (2014).
46 Raiteri, P., Gale, J. D., Quigley, D. & Rodger, P. M. Derivation of an accurate force-field for simulating the growth of calcium carbonate from aqueous solution: A new model for the calcite− Water interface. *The Journal of Physical Chemistry C* **114**, 5997-6010 (2010).
47 González, M. Force fields and molecular dynamics simulations. *École thématique de la Société Française de la Neutronique* **12**, 169-200 (2011).
48 Tavares, C. A., Santos, T. M., da Cunha, E. F. & Ramalho, T. C. Molecular dynamics-assisted interaction of vanadium complex–AMPK: from force field development to biological application for Alzheimer's treatment. *The Journal of Physical Chemistry B* **127**, 495-504 (2023).
49 He, X., Man, V. H., Yang, W., Lee, T.-S. & Wang, J. A fast and high-quality charge model for the next generation general AMBER force field. *The Journal of Chemical Physics* **153**, 114502 (2020).
50 Goloviznina, K., Gong, Z. & Padua, A. A. The CL &Pol polarizable force field for the simulation of ionic liquids and eutectic solvents. *Wiley Interdisciplinary Reviews: Computational Molecular Science* **12**, e1572 (2022).
51 Greff da Silveira, L., Livotto, P. R., Padula, D., Vilhena, J. & Prampolini, G. Accurate Quantum-Mechanically Derived Force-Fields through a Fragment-Based Approach: Balancing Specificity and Transferability in the Prediction of Self-Assembly in Soft Matter. *Journal of Chemical Theory and Computation* **18**, 6905-6919 (2022).
52 Lay, W. K. *Optimizing computer simulation models for carbohydrates and proteins at the atomistic and coarse-grained level*, University of Iowa, (2018).
53 Buckner, J. *et al.* pyCHARMM: Embedding CHARMM Functionality in a Python Framework. (2023).
54 Nester, K., Gaweda, K. & Plazinski, W. A GROMOS force field for furanose-based carbohydrates. *Journal of Chemical Theory and Computation* **15**, 1168-1186 (2019).
55 Woods, R. J. Predicting the structures of glycans, glycoproteins, and their complexes. *Chemical reviews* **118**, 8005-8024 (2018).

56 Sun, H. COMPASS: an ab initio force-field optimized for condensed-phase applications overview with details on alkane and benzene compounds. *The Journal of Physical Chemistry B* **102**, 7338-7364 (1998).
57 Foloppe, N. & MacKerell, J., Alexander D. All- atom empirical force field for nucleic acids: I. Parameter optimization based on small molecule and condensed phase macromolecular target data. *Journal of computational chemistry* **21**, 86-104 (2000).
58 Brooks, B. R. *et al.* CHARMM: a program for macromolecular energy, minimization, and dynamics calculations. *Journal of computational chemistry* **4**, 187-217 (1983).
59 Dzubiella, J., Swanson, J. M. & McCammon, J. Coupling hydrophobicity, dispersion, and electrostatics in continuum solvent models. *Physical review letters* **96**, 087802 (2006).
60 Inakollu, V. S., Geerke, D. P., Rowley, C. N. & Yu, H. Polarisable force fields: what do they add in biomolecular simulations? *Current Opinion in Structural Biology* **61**, 182-190 (2020).
61 Dauber- Osguthorpe, P. *et al.* Structure and energetics of ligand binding to proteins: Escherichia coli dihydrofolate reductase- trimethoprim, a drug- receptor system. *Proteins: Structure, Function, and Bioinformatics* **4**, 31-47 (1988).
62 Beachy, M. D., Chasman, D., Murphy, R. B., Halgren, T. A. & Friesner, R. A. Accurate ab initio quantum chemical determination of the relative energetics of peptide conformations and assessment of empirical force fields. *Journal of the American Chemical Society* **119**, 5908-5920 (1997).
63 Wang, Y. *et al.* End-to-end differentiable construction of molecular mechanics force fields. *Chemical Science* **13**, 12016-12033 (2022).
64 Chakraborty, T., Hens, A., Kulashrestha, S., Murmu, N. C. & Banerjee, P. Calculation of diffusion coefficient of long chain molecules using molecular dynamics. *Physica E: Low-dimensional Systems and Nanostructures* **69**, 371-377 (2015).
65 Shi, Y. *et al.* Polarizable atomic multipole-based AMOEBA force field for proteins. *Journal of chemical theory and computation* **9**, 4046-4063 (2013).
66 Ballone, P. Modeling potential energy surfaces: From first-principle approaches to empirical force fields. *Entropy* **16**, 322-349 (2013).
67 Ghadyani, G. & Rahmandoust, M. Computational nanomechanics investigation techniques. *Advanced Computational Nanomechanics*, 99-122 (2016).
68 Knee, G. C. *et al.* Violation of a Leggett–Garg inequality with ideal non-invasive measurements. *Nature communications* **3**, 606 (2012).
69 Amaro, R. E. *et al.* Ensemble docking in drug discovery. *Biophysical journal* **114**, 2271-2278 (2018).
70 Tuckerman, M. *Statistical mechanics: theory and molecular simulation*. (Oxford university press, 2010).
71 Harshe, R. P. & De, R. Corrected Analysis of Microcanonical Ensemble Model of Mixture of Fermions and Bosons at the Low-Temperature Limit. *Int. J. Sci. Res. in Mathematical and Statistical Sciences Vol* **7** (2020).
72 Mey, A. S., Geissler, P. L. & Garrahan, J. P. Rare-event trajectory ensemble analysis reveals metastable dynamical phases in lattice proteins. *Physical Review E* **89**, 032109 (2014).
73 Dubbeldam, D., Calero, S., Ellis, D. E. & Snurr, R. Q. RASPA: molecular simulation software for adsorption and diffusion in flexible nanoporous materials. *Molecular Simulation* **42**, 81-101 (2016).
74 Abbasi, E., Moghaddam, M. R. A. & Kowsari, E. A systematic and critical review on development of machine learning based-ensemble models for prediction of adsorption process efficiency. *Journal of Cleaner Production*, 134588 (2022).

75 Belhaj, A. F. *et al.* Experimental investigation, binary modelling and artificial neural network prediction of surfactant adsorption for enhanced oil recovery application. *Chemical Engineering Journal* **406**, 127081 (2021).
76 Yousef, R. I., El-Eswed, B. & Ala'a, H. Adsorption characteristics of natural zeolites as solid adsorbents for phenol removal from aqueous solutions: kinetics, mechanism, and thermodynamics studies. *Chemical engineering journal* **171**, 1143-1149 (2011).
77 Barasa, G. O. *et al.* Electrochemical training of nanoporous Cu-In catalysts for efficient CO2-to-CO conversion and high durability. *Electrochimica Acta* **295**, 584-590 (2019).
78 Böhringer, W., Kotsiopoulos, A., de Boer, M., Knottenbelt, C. & Fletcher, J. in *Studies in surface science and catalysis* Vol. 163 345-365 (Elsevier, 2007).
79 Surdam, R. C. & Eugster, H. P. Mineral reactions in the sedimentary deposits of the Lake Magadi region, Kenya. *Geological Society of America Bulletin* **87**, 1739-1752 (1976).
80 Kodikara, G. R. *et al.* Hyperspectral remote sensing of evaporate minerals and associated sediments in Lake Magadi area, Kenya. *International Journal of Applied Earth Observation and Geoinformation* **14**, 22-32 (2012).
81 LeVan, M. D., Carta, G. & Yon, C. M. Adsorption and ion exchange. *Energy* **16**, 17 (1997).
82 Sun, M.-H. *et al.* Applications of hierarchically structured porous materials from energy storage and conversion, catalysis, photocatalysis, adsorption, separation, and sensing to biomedicine. *Chemical society reviews* **45**, 3479-3563 (2016).
83 Tailor, R. V. Adaptation of Bagasse fly ash into zeolites for the removal of phenols from aqueous solution. (2011).
84 Zeng, Y. Fundamental study of adsorption and desorption process in porous materials with functional groups. (2016).
85 Lamia, M., Fatiha, D., Mohammed, B., Mustapha, D. & Ayada, D. Design and modeling adsorption kinetics of methylene blue on zeolite adsorbents and clay. *International Journal of Clothing Science and Technology* (2016).
86 Yuna, Z. Review of the natural, modified, and synthetic zeolites for heavy metals removal from wastewater. *Environmental Engineering Science* **33**, 443-454 (2016).
87 Najjar, R., Heidari, S. & Tazerout, M. Formulation of an economical microemulsion of diesel/colza oil fuel and investigation of some physical parameters for its stability. *Environmental Progress & Sustainable Energy* **37**, 1762-1769 (2018).
88 Kalló, D. Applications of natural zeolites in water and wastewater treatment. *Reviews in mineralogy and geochemistry* **45**, 519-550 (2001).
89 Ritter, L., Solomon, K., Forget, J., Stemeroff, M. & O'Leary, C. Persistent organic pollutants: an assessment report on: DDT, aldrin, dieldrin, endrin, chlordane, heptachlor, hexachlorobenzene, mirex, toxaphene, polychlorinated biphenyls, dioxins and furans. *International Programme on Chemical Safety (IPCS)* (1995).
90 Chasek, P. S. NGOs and state capacity in international environmental negotiations: The experience of the Earth Negotiations Bulletin. *Rev. Eur. Comp. & Int'l Envtl. L.* **10**, 168 (2001).
91 Guo, Z. Literature review of remediation methods for PCBs in building. (2012).
92 Hung, H. *et al.* Temporal trends of Persistent Organic Pollutants (POPs) in arctic air: 20 years of monitoring under the Arctic Monitoring and Assessment Programme (AMAP). *Environmental Pollution* **217**, 52-61 (2016).
93 Kuiper, J. Failure of hexachlorobenzene to control common bunt of wheat. *Nature* **206**, 1219-1220 (1965).
94 Jing, R., Fusi, S. & Kjellerup, B. V. Remediation of polychlorinated biphenyls (PCBs) in contaminated soils and sediment: state of knowledge and perspectives. *Frontiers in Environmental Science* **6**, 79 (2018).

95 Wu, J. *et al.* Short-and medium-chain chlorinated paraffins in multi-environmental matrices in the Tibetan Plateau environment of China: A regional scale study. *Environment International* **140**, 105767 (2020).
96 Gomes, H. I., Dias-Ferreira, C. & Ribeiro, A. B. Overview of in situ and ex situ remediation technologies for PCB-contaminated soils and sediments and obstacles for full-scale application. *Science of the Total Environment* **445**, 237-260 (2013).
97 Glüge, J., Wang, Z., Bogdal, C., Scheringer, M. & Hungerbühler, K. Global production, use, and emission volumes of short-chain chlorinated paraffins–A minimum scenario. *Science of the Total Environment* **573**, 1132-1146 (2016).
98 Bettina, H., Hermann, F., Wolfgang, V. l. & Mehmet, C. Effects of chain length, chlorination degree, and structure on the octanol− water partition coefficients of polychlorinated n-alkanes. *Environmental science & technology* **45**, 2842-2849 (2011).
99 Tomy, G. T., Muir, D. C., Stern, G. A. & Westmore, J. B. Levels of C10− C13 polychloro-n-alkanes in marine mammals from the Arctic and the St. Lawrence River Estuary. *Environmental science & technology* **34**, 1615-1619 (2000).
100 Iozza, S., Müller, C. E., Schmid, P., Bogdal, C. & Oehme, M. Historical profiles of chlorinated paraffins and polychlorinated biphenyls in a dated sediment core from Lake Thun (Switzerland). *Environmental science & technology* **42**, 1045-1050 (2008).
101 Zeng, L. *et al.* Distribution and trophic transfer of short-chain chlorinated paraffins in an aquatic ecosystem receiving effluents from a sewage treatment plant. *Environmental science & technology* **45**, 5529-5535 (2011).
102 Zeng, L. *et al.* Spatial and vertical distribution of short chain chlorinated paraffins in soils from wastewater irrigated farmlands. *Environmental science & technology* **45**, 2100-2106 (2011).
103 Houde, M. *et al.* Bioaccumulation and trophic magnification of short-and medium-chain chlorinated paraffins in food webs from Lake Ontario and Lake Michigan. *Environmental science & technology* **42**, 3893-3899 (2008).
104 Fisk, A. T., Tomy, G. T. & Muir, D. C. Toxicity of C, C, C, and C Polychlorinated alkanes to Japanese medaka (Oryzias latipes) embryos. *Environmental Toxicology and Chemistry: An International Journal* **18**, 2894-2902 (1999).
105 Warnasuriya, G. D., Elcombe, B. M., Foster, J. R. & Elcombe, C. R. A mechanism for the induction of renal tumours in male Fischer 344 rats by short-chain chlorinated paraffins. *Archives of toxicology* **84**, 233-243 (2010).
106 Gao, W. *et al.* Elimination of short-chain chlorinated paraffins in diet after Chinese traditional cooking-a cooking case study. *Environment international* **122**, 340-345 (2019).
107 Wang, X.-T., Xu, S.-Y., Wang, X.-K., Hu, B.-P. & Jia, H.-H. Occurrence, homologue patterns and source apportionment of short-and medium-chain chlorinated paraffins in suburban soils of Shanghai, China. *Chemosphere* **180**, 302-311 (2017).
108 Wang, Y., Gao, W. & Jiang, G. (ACS Publications, 2017).
109 Glüge, J., Schinkel, L., Hungerbühler, K., Cariou, R. & Bogdal, C. Environmental risks of medium-chain chlorinated paraffins (MCCPs): a review. *Environmental science & technology* **52**, 6743-6760 (2018).
110 Mackay, D. & Wania, F. Transport of contaminants to the Arctic: partitioning, processes and models. *Science of the total environment* **160**, 25-38 (1995).
111 Zeng, L. *et al.* Behavior, fate, and mass loading of short chain chlorinated paraffins in an advanced municipal sewage treatment plant. *Environmental science & technology* **47**, 732-740 (2013).
112 Zeng, L. *et al.* Spatial distributions and deposition chronology of short chain chlorinated paraffins in marine sediments across the Chinese Bohai and Yellow Seas. *Environmental science & technology* **47**, 11449-11456 (2013).

113 Zeng, L., Lam, J. C., Wang, Y., Jiang, G. & Lam, P. K. Temporal trends and pattern changes of short-and medium-chain chlorinated paraffins in marine mammals from the South China Sea over the past decade. *Environmental Science & Technology* **49**, 11348-11355 (2015).
114 Gutierrez-Urbano, I., Villen-Guzman, M., Perez-Recuerda, R. & Rodriguez-Maroto, J. M. Removal of polycyclic aromatic hydrocarbons (PAHs) in conventional drinking water treatment processes. *Journal of Contaminant Hydrology* **243**, 103888 (2021).
115 He, Y. *et al.* Suspended particulate matter (SPM)-bound polycyclic aromatic hydrocarbons (PAHs) in lakes and reservoirs across a large geographical scale. *Science of The Total Environment* **752**, 142863 (2021).
116 Karyab, H. *et al.* Polycyclic aromatic hydrocarbons in drinking water of Tehran, Iran. *Journal of Environmental Health Science and Engineering* **11**, 1-7 (2013).
117 Mojiri, A., Zhou, J. L., Ohashi, A., Ozaki, N. & Kindaichi, T. Comprehensive review of polycyclic aromatic hydrocarbons in water sources, their effects and treatments. *Science of the total environment* **696**, 133971 (2019).
118 Fu, H., Wang, Y., Zhang, T., Yang, C. & Shan, H. Adsorption and Separation Mechanism of Thiophene/Benzene in MFI Zeolite: A GCMC Study. *The Journal of Physical Chemistry C* **121**, 25818-25826 (2017).
119 Sharma, S., Kumar, P. & Chandra, R. Applications of BIOVIA materials studio, LAMMPS, and GROMACS in various fields of science and engineering. *Molecular Dynamics Simulation of Nanocomposites Using BIOVIA Materials Studio, Lammps and Gromacs*, 329-341 (2019).
120 Akkermans, R. L., Spenley, N. A. & Robertson, S. H. Monte Carlo methods in materials studio. *Molecular Simulation* **39**, 1153-1164 (2013).
121 Deschenes, L. A. & David A. Vanden BoutUniversity of Texas, A. (ACS Publications, 2000).
122 Edwards, P. M. Origin 7.0: scientific graphing and data analysis software. *Journal of chemical information and computer sciences* **42**, 1270-1271 (2002).
123 Joshi, S. Y. *et al.* New insights into the mechanism of NH3-SCR over Cu-and Fe-zeolite catalyst: Apparent negative activation energy at high temperature and catalyst unit design consequences. *Applied Catalysis B: Environmental* **226**, 565-574 (2018).
124 Bezerra, D. P., Oliveira, R. S., Vieira, R. S., Cavalcante, C. L. & Azevedo, D. C. Adsorption of CO 2 on nitrogen-enriched activated carbon and zeolite 13X. *Adsorption* **17**, 235-246 (2011).
125 Guzman, A. *et al.* Influence of the activation temperature on the physicochemical properties and catalytic activity of La-X zeolites for isobutane/cis-2-butene alkylation. *Microporous and mesoporous materials* **97**, 49-57 (2006).
126 Tsitsishvili, V. *et al.* Dehydration and structural transformations during thermal treatment of Georgian, Kazakhstani and Armenian natural heulandite-clinoptilolites. *Scientific Collection «InterConf»*, 356-364 (2022).
127 Cai, W. *et al.* Thermal structural transitions and carbon dioxide adsorption properties of zeolitic imidazolate framework-7 (ZIF-7). *Journal of the American Chemical Society* **136**, 7961-7971 (2014).
128 Liang, Z. & Ni, J. Improving the ammonium ion uptake onto natural zeolite by using an integrated modification process. *Journal of Hazardous Materials* **166**, 52-60 (2009).
129 Mishra, R. K. *et al.* cemff: A force field database for cementitious materials including validations, applications and opportunities. *Cement and Concrete Research* **102**, 68-89 (2017).
130 Yeddou, N. & Bensmaili, A. Equilibrium and kinetic modelling of iron adsorption by eggshells in a batch system: effect of temperature. *Desalination* **206**, 127-134 (2007).

131 Kuete, I.-H. T., Tchuifon, D. R. T., Ndifor-Angwafor, G. N., Kamdem, A. T. & Anagho, S. G. Kinetic, isotherm and thermodynamic studies of the adsorption of thymol blue onto powdered activated carbons from Garcinia cola nut shells impregnated with H3PO4 and KOH: non-linear regression analysis. *Journal of Encapsulation and Adsorption Sciences* **10**, 1-27 (2020).
132 Aksu, Z. & Tezer, S. Biosorption of reactive dyes on the green alga Chlorella vulgaris. *Process Biochemistry* **40**, 1347-1361 (2005).
133 Sedláček, Z. Isosteric adsorption heats in correlation with activation energy of diffusion. *Chem. zvesti* **29**, 344-349 (1975).
134 Kondo, J. N. *et al.* Activation energies for the reaction of ethoxy species to ethene over zeolites. *The Journal of Physical Chemistry C* **114**, 20107-20113 (2010).
135 Boerth, D. W. & Arvanites, A. C. Nucleophilic aromatic substitution in chlorinated aromatic systems with a glutathione thiolate model. *Journal of Physical Organic Chemistry* **30**, e3640 (2017).
136 Horváthová, H., Lászlová, K. & Dercová, K. Bioremediation vs. nanoremediation: Degradation of polychlorinated biphenyls (PCBS) using integrated remediation approaches. *Water, Air, & Soil Pollution* **230**, 1-11 (2019).
137 Bae, Y.-S. & Snurr, R. Q. Optimal isosteric heat of adsorption for hydrogen storage and delivery using metal–organic frameworks. *Microporous and Mesoporous Materials* **132**, 300-303 (2010).
138 Gupta, V. K. Equilibrium uptake, sorption dynamics, process development, and column operations for the removal of copper and nickel from aqueous solution and wastewater using activated slag, a low-cost adsorbent. *Industrial & Engineering Chemistry Research* **37**, 192-202 (1998).
139 Johnson, T. A., Jain, N., Joshi, H. & Prasad, S. Agricultural and agro-processing wastes as low cost adsorbents for metal removal from wastewater: A review. (2008).
140 Ye, G. *et al.* Optimizing spatial pore-size and porosity distributions of adsorbents for enhanced adsorption and desorption performance. *Chemical Engineering Science* **132**, 108-117 (2015).
141 Liu, S. A Second Discussion on Cosmic Space in Zero Dimension—A Discussion on Spatial Questions According to Classical Physics. *Journal of Applied Mathematics and Physics* **9**, 556-564 (2021).
142 Ziółkowski, P. *et al.* Comprehensive thermodynamic analysis of steam storage in a steam cycle in a different regime of work: A zero-dimensional and three-dimensional approach. *Journal of Energy Resources Technology* **144** (2022).
143 Banaschewski, B. & Brümmer, G. STRONG ZERO-DIMENSIONALITY OF BIFRAMES AND BISPACES: For the sixtieth birthday of Keith Hardie. *Quaestiones Mathematicae* **13**, 273-290 (1990).
144 Magdalena, W. *et al.* Experimental Study on the Removal of VOCs and PAHs by Zeolites and Surfactant-Modified Zeolites. (2017).
145 Khalfaoui, M., Baouab, M., Gauthier, R. & Lamine, A. B. Statistical physics modelling of dye adsorption on modified cotton. *Adsorption Science & Technology* **20**, 17-31 (2002).
146 Lamine, A. B. & Bouazra, Y. Application of statistical thermodynamics to the olfaction mechanism. *Chemical senses* **22**, 67-75 (1997).
147 Elqahtani, Z., Ben Yahia, M., Alfryyan, N., Aldaghfag, S. & Aouaini, F. Statistical Physics Modeling of Sorption Isotherms of Aluminum, Iron, and Indium on Tetraphenylporphyrin (H2TPP) and Tetrakis (4-tolylphenyl) porphyrin (H2TTPP): Phenomenological Investigation of Metalloporphyrins at the Molecular Level. *Adsorption Science & Technology* **2021** (2021).

148 Assef, M. Statistical Theory of Two-Component Crystal I-Case of One Dimensional Crystal. *Open Access Library Journal* **8**, 1-14 (2021).
149 Khalfaoui, M., Knani, S., Hachicha, M. & Lamine, A. B. New theoretical expressions for the five adsorption type isotherms classified by BET based on statistical physics treatment. *Journal of colloid and interface science* **263**, 350-356 (2003).
150 Alaya, M., Hourieh, M., Youssef, A. & El-Sejariah, F. Adsorption properties of activated carbons prepared from olive stones by chemical and physical activation. *Adsorption Science & Technology* **18**, 27-42 (2000).
151 Estermann, M., McCusker, L., Baerlocher, C., Merrouche, A. & Kessler, H. A synthetic gallophosphate molecular sieve with a 20-tetrahedral-atom pore opening. *Nature* **352**, 320-323 (1991).
152 Zheng, N., Bu, X., Wang, B. & Feng, P. Microporous and photoluminescent chalcogenide zeolite analogs. *Science* **298**, 2366-2369 (2002).
153 Sun, J. *et al.* The ITQ-37 mesoporous chiral zeolite. *Nature* **458**, 1154-1157 (2009).
154 Jiang, J., Yun, Y., Zou, X., Jorda, J. L. & Corma, A. ITQ-54: a multi-dimensional extra-large pore zeolite with 20× 14× 12-ring channels. *Chemical science* **6**, 480-485 (2015).
155 Gramlich, V. & Meier, W. The crystal structure of hydrated NaA: A detailed refinement of a pseudosymmetric zeolite structure. *Zeitschrift für Kristallographie-Crystalline Materials* **133**, 134-149 (1971).
156 Effenberger, H., Giester, G., Krause, W. & Bernhardt, H. Tschortnerite, a copper-bearing zeolite from the Bellberg volcano, Eifel, Germany. *American Mineralogist* **83**, 607-617 (1998).
157 Baur, W. H. On the cation and water positions in faujasite. *American Mineralogist: Journal of Earth and Planetary Materials* **49**, 697-704 (1964).
158 Yun, Y. *et al.* The first zeolite with a tri-directional extra-large 14-ring pore system derived using a phosphonium-based organic molecule. *Chemical Communications* **51**, 7602-7605 (2015).
159 You, X. *et al.* Molecular dynamics simulations of removal of nonylphenol pollutants by graphene oxide: Experimental study and modelling. *Applied Surface Science* **475**, 621-626 (2019).
160 Stefaniu, A. & Pintilie, L. Molecular Descriptors and Properties of Organic Molecules. *Symmetry (Group Theory) and Mathematical Treatment in Chemistry*, 161 (2018).
161 Mebi, C. A. DFT study on structure, electronic properties, and reactivity of cis-isomers of [(NC 5 H 4-S) 2 Fe (CO) 2]. *Journal of Chemical Sciences* **123**, 727-731 (2011).
162 Schenk, M., Smit, B., Vlugt, T. J. & Maesen, T. L. Shape selectivity in hydrocarbon conversion. *Angewandte Chemie International Edition* **40**, 736-739 (2001).
163 Logan, B. E. *et al.* Microbial electrolysis cells for high yield hydrogen gas production from organic matter. *Environmental science & technology* **42**, 8630-8640 (2008).
164 Fischer, M. Simulation-based evaluation of zeolite adsorbents for the removal of emerging contaminants. *Materials Advances* **1**, 86-98 (2020).
165 Khader, E. H. *et al.* Removal of organic pollutants from produced water by batch adsorption treatment. *Clean Technologies and Environmental Policy* **24**, 713-720 (2022).
166 Wanyonyi, F. S., Pembere, A., Mutua, G. K., Orata, F. & Louis, H. Computational screening of zeolites for the adsorption of selected pharmaceutical pollutants. *SN Applied Sciences* **2**, 1-9 (2020).
167 Nsaif, M. & Saeed, F. The feasibility of rice husk to remove minerals from water by adsorption and avail from wastes. *WSEAS Trans Environ Dev* **9**, 301-313 (2013).

APPENDICES
Appendix 1: Loading of organic pollutants on zeolites

Tables Ap4.1; Loading of hexachlorobenzene on zeolites, activation energies (E_a) and isosteric heats at a temperature of 298K and a pressure range of between 101.325KPa and 1013KPa

S/NO	Zeolite	Mass [g/mol]	D [kg/m^3]	HVF	APV [cm^3/g]	VSA [m^2/cm^3]	GSA [m^2/g]	DPS	Di	Loading	Wt%	Total energy	Isosteric heats
1.	CLO	17728	1129	0.55	0.49	2070	1834	3	10.06	120	65.84	-641.824	37.892
2.	RWY	2884	854.6	0.66	0.77	2040	2387	3	14	12	54.23	-98.812	42.392
3.	ITV	11792	1075	0.55	0.51	2110	1963	3	8.54	21	33.65	-130.917	36.192
4.	IFU	7755	1221	0.53	0.44	1703	1395	3	10.46	13	32.41	-178.525	51.092
5.	LTA	1442	1414	0.47	0.33	1675	1184	3	10.24	13	32.31	-229.821	46.392
6.	IRR	3124	1173	0.57	0.48	1626	1386	3	13.92	5	31.31	-33.648	36.292
7.	FAU	11536	1328	0.49	0.37	1616	1217	3	10.69	16	28.32	-207.802	46.592
8.	SBT	8652	1368	0.47	0.34	1585	1159	3	10.41	12	28.32	-179.148	48.092
9.	VFI	2163	1444	0.4	0.28	1154	799	1	11.41	3	28.32	-34.18	36.592
10.	TSC	23072	1319	0.49	0.37	1473	1117	3	15.87	28	25.69	-315.237	42.892
11.	SBS	5768	1369	0.47	0.34	1586	1158	3	10.97	7	25.69	-99.867	44.392
12.	AFS	3365	1460	0.44	0.3	1720	1178	3	9.11	4	25.29	-67.409	44.792
13.	ITT	2764	1280	0.52	0.41	1573	1229	3	12.77	3	23.61	-20.902	31.392
14.	IFO	1923	1724	0.32	0.19	1144	663.4	1	7.42	2	22.85	-44.203	41.992
15.	AFY	961.4	1409	0.48	0.34	2103	1492	3	7.42	1	22.85	-7.673	27.292
16.	DFO	7931	1486	0.43	0.29	1626	1094	3	10.89	8	22.32	-93.706	40.792
17.	MEI	2043	1464	0.43	0.29	1681	1148	1	7.66	2	21.8	-31.131	38.792
18.	SBE	7691	1370	0.46	0.34	1514	1105	3	12.09	7	20.59	-80.248	40.292
19.	EMT	7931	1486	0.43	0.29	1626	1094	3	10.89	7	20.09	-97.62	45.392
20.	OBW	4566	1270	0.47	0.37	1992	1568	3	8.86	4	19.97	-47.672	33.692
21.	USI	2403	1587	0.39	0.25	1666	1050	2	6.32	2	19.16	-40.21	39.692
22.	UFI	3845	1517	0.43	0.29	1568	1034	2	9.69	3	18.18	-58.354	47.592
23.	BOZ	5528	1291	0.46	0.36	2018	1563	3	8.31	4	17.09	-55.057	35.292
24.	IRN	5528	1528	0.41	0.27	1503	983.5	2	8.62	4	17.09	-74.834	40.692
25.	ETR	2884	1541	0.37	0.24	1350	876.4	3	9.61	2	16.49	-25.33	38.992
26.	RHO	2884	1442	0.45	0.31	1711	1186	3	10.03	2	16.49	-29.573	35.892
27.	SAV	2884	1458	0.39	0.27	1726	1184	3	8.28	2	16.49	-40.465	40.292
28.	UTL	4566	1556	0.41	0.26	1457	936.8	2	8.7	3	15.76	-42.929	44.792
29.	SSF	3245	1642	0.32	0.19	1191	725.4	2	7.26	2	14.93	-35.974	40.292
30.	IWR	3365	1561	0.41	0.26	1610	1032	3	6.9	2	14.48	-28.11	33.892
31.	SAO	3365	1415	0.48	0.34	1736	1227	3	8.21	2	14.48	-23.41	31.592
32.	SFS	3365	1659	0.35	0.21	1407	847.7	2	7.05	2	14.48	-17.382	37.192
33.	BPH	1682	1459	0.44	0.3	1688	1157	3	9.11	1	14.48	-5.321	24.692
34.	MSO	5408	1779	0.26	0.15	1002	563.2	0	0	3	13.64	-79.525	47.192
35.	IWV	9133	1499	0.41	0.27	1455	971.1	2	8.14	5	13.49	-87.511	41.592
36.	KFI	5768	1494	0.41	0.28	1639	1097	3	10.16	3	12.9	-38.293	45.692
37.	JSR	5768	1226	0.52	0.42	2271	1853	3	7.43	3	12.9	-39.938	34.492
38.	DON	3845	1708	0.29	0.17	955.6	559.4	1	8.18	2	12.9	-25.173	33.392
39.	IFW	3845	1576	0.37	0.24	1411	895.5	3	7.22	2	12.9	-38.663	40.092
40.	ISV	3845	1501	0.43	0.28	1637	1091	3	6.37	2	12.9	-30.318	35.892
41.	POS	3845	1551	0.41	0.26	1611	1039	3	6.71	2	12.9	-29.807	34.992
42.	BEC	1923	1509	0.42	0.28	1634	1083	3	6.24	1	12.9	-14.602	34.092
43.	SFN	1923	1652	0.32	0.19	1168	706.9	1	7.47	1	12.9	-21.485	41.192
44.	SFO	1923	1513	0.41	0.27	1601	1058	2	7.49	1	12.9	-19.407	39.092
45.	IWS	8171	1476	0.43	0.29	1624	1100	3	7.63	4	12.24	-46.362	32.092
46.	EWT	4302	1483	0.42	0.28	1814	1223	3	7.35	2	11.69	-15.682	29.392
47.	AET	4326	1817	0.24	0.13	863.3	475.1	1	7.76	2	11.63	-26.738	33.392
48.	LTL	2163	1668	0.29	0.18	1002	600.6	1	9.61	1	11.63	-12.648	32.892
49.	SFH	3333	1426	0.29	0.21	1203	843.6	1	7.66	1	7.87	-18.34	37.992
50.	ITG	3365	1654	0.36	0.22	1509	912.4	3	6.44	1	7.8	-15.113	34.696
51.	UOV	10575	1620	0.37	0.23	1485	917	3	6.58	3	7.48	-52.432	37.992
52.	UWY	3605	1627	0.36	0.22	1480	909.9	3	8.38	1	7.32	-11.62	31.192

S/NO	Zeolite	Mass [g/mol]	D [kg/m^3]	HVF	APV [cm^3/g]	VSA [m^2/cm$^{3]}$	GSA [m^2/g]	DPS	Di	Loading	Wt%	Total energy	Isosteric heats
53.	MWW	4326	1590	0.39	0.25	1542	970.1	2	9.29	1	6.18	-12.797	32.792
54.	IRY	4598	1115	0.6	0.54	1702	1526	3	10.69	10	5.81	-99.887	43.692
55.	TUN	11536	1757	0.32	0.18	1275	725.5	3	8.04	2	4.78	-37.297	38.392
56.	LTN	46145	1695	0.31	0.18	1182	697.1	0	0	8	4.71	-141.598	38.092
57.	MOZ	6489	1693	0.3	0.18	1122	662.8	1	9.63	1	4.2	-13.803	34.092
58.	IWW	6729	1659	0.35	0.21	1394	840.6	3	6.55	1	4.06	-14.876	34.692
59.	MSE	6729	1633	0.36	0.22	1420	869.7	3	6.5	1	4.06	-19.536	39.092
60.	PAU	40377	1586	0.36	0.23	1639	1034	3	10.08	2	1.39	-28.809	35.492
61.	MWF	86521	1604	0.35	0.22	1594	993.8	3	10.06	2	0.65	-32.297	36.592
62.	SFV	47106	1755	0.3	0.17	1248	711.2	3	7.07	1	0.6	-19.829	39.192
63.	IFT	-	-	-	-	-	-	-	-	11	-	-96.826	42.792
64.	SYT	-	-	-	-	-	-	-	-	8	-	-58.067	41.292
65.	CTH	-	-	-	-	-	-	-	-	4	-	-70.882	37.792
66.	YFI	-	-	-	-	-	-	-	-	4	-	-70.314	38.792
67.	SOV	-	-	-	-	-	-	-	-	3	-	-40.506	34.992
68.	PWN	-	-	-	-	-	-	-	-	2	-	-30.668	36.592
69.	PCS	-	-	-	-	-	-	-	-	1	-	-20.621	40.092
70.	SOR	-	-	-	-	-	-	-	-	1	-	-19.156	38.792
71.	SVY	-	-	-	-	-	-	-	-	1	-	-14.524	34.392
72.	ABW	480	1755	0.21	0.12	1086	618.8	1	3.61	0	-	0	-
73.	ACO	961.4	1643	0.32	0.19	1727	1052	3	3.92	0	-	0	-
74.	AEI	2884	1502	0.4	0.27	1735	1156	3	6.9	0	-	0	-
75.	AEL	2403	1914	0.19	0.1	840.1	438.9	1	5.23	0	-	0	-
76.	AEN	2884	2008	0.17	0.08	847.8	422.2	2	3.91	0	-	0	-
77.	AFG	2884	1689	0.29	0.17	1156	684.2	0	0	0	-	0	-
78.	AFI	1442	1685	0.29	0.17	1020	605.4	1	7.57	0	-	0	-
79.	AFN	1923	1736	0.25	0.14	1178	678.9	1	4.75	0	-	0	-
80.	AFO	2403	1916	0.2	0.11	854.2	445.7	1	5.03	0	-	0	-
81.	AFR	1923	1513	0.4	0.26	1600	1058	2	7.82	0	-	0	-
82.	AFT	4326	1503	0.4	0.26	1724	1147	3	7.14	0	-	0	-
83.	AFV	1803	1570	0.38	0.24	1638	1043	2	6.45	0	-	0	-
84.	AFX	2884	1502	0.4	0.27	1733	1154	3	7.12	0	-	0	-
85.	AHT	1442	1917	0.11	0.06	546.6	285.1	0	0	0	-	0	-
86.	ANA	2884	1918	0.1	0.05	426	222.1	0	0	0	-	0	-
87.	APC	1922	1765	0.19	0.11	875.6	496	1	3.83	0	-	0	-
88.	APD	1923	1795	0.21	0.12	1015	565.4	1	4.22	0	-	0	-
89.	AST	2403	1578	0.39	0.25	1438	911.4	0	0	0	-	0	-
90.	ASV	1202	1905	0.23	0.12	1036	543.055	1	4.95	0	-	0	-
91.	ATN	961.3	1778	0.23	0.13	1051	591.2	1	5.51	0	-	0	-
92.	ATO	2163.	1874	0.19	0.1	795.9	424.8	1	5.34	0	-	0	-
93.	ATS	1442	1603	0.33	0.21	1300	811.1	1	6.58	0	-	0	-
94.	ATT	721	1704	0.3	0.18	1512	887.3	2	4.9	0	-	0	-
95.	ATV	1442	1887	0.16	0.08	712.4	377.5	1	3.92	0	-	0	-

S/NO	Zeolite	Mass [g/mol]	D [kg/m^3]	HVF	APV [cm^3/g]	VSA [m^2/cm^3]	GSA [m^2/g]	DPS	Di	Loading	Wt%	Total energy	Isosteric heats
96.	AVL	2524	1579	0.37	0.23	1597	1011	2	6.58	0	-	0	-
97.	AWO	2884	1819	0.2	0.11	872.3	479.6	2	4.5	0	-	0	-
98.	AWW	1442	1689	0.31	0.18	1265	748.9	1	6.89	0	-	0	-
99.	BCT	480.7	1895	0.06	0.03	69.97	36.92	0	0	0	-	0	-
100.	BEA	3845	1528	0.42	0.27	1631	1068	3	6.12	0	-	0	-
101.	BIK	721	1862	0.16	0.09	816.4	438.4	1	3.76	0	-	0	-
102.	BOF	1442	1823	0.26	0.14	1208	662.8	1	5.16	0	-	0	-
103.	BOG	5768	1602	0.38	0.24	1486	927.7	3	7.49	0	-	0	-
104.	BRE	961.4	1827	0.23	0.13	1026	561.5	1	4.88	0	-	0	-
105.	BSV	5768	1865	0.23	0.12	1204	645.4	3	4.77	0	-	0	-
106.	CAN	721	1686	0.29	0.17	1184	702.3	1	5.76	0	-	0	-
107.	CAS	1442	1871	0.15	0.08	661.1	353.3	1	4.44	0	-	0	-
108.	CFI	2163	1801	0.25	0.14	1129	626.5	2	4.99	0	-	0	-
109.	CGF	1923	1673	0.29	0.18	1065	636.7	1	7.07	0	-	0	-
110.	CGS	2163	1896	0.21	0.11	882.7	465.7	1	5.04	0	-	0	-
111.	CHA	1923	1685	0.29	0.17	1412	837.6	3	5.32	0	-	0	-
112.	CHI	1051	591.2	0.24	0.13	1051	591.2	1	5.51	0	-	0	-
113.	CON	1746	2056	0.1	0.05	549.5	267.2	1	3.51	0	-	0	-
114.	CZP	1442	2126	0.17	0.08	872	410.2	1	3.76	0	-	0	-
115.	DAC	1442	1741	0.3	0.17	1428	819.9	2	4.79	0	-	0	-
116.	DDR	7210	1783	0.3	0.17	1174	658.7	2	7.07	0	-	0	-
117.	DFT	480.7	1767	0.26	0.15	1126	637	3	4.19	0	-	0	-
118.	DOH	2043	1692	0.34	0.2	1243	734.5	0	0	0	-	0	-
119.	EAB	2163	1592	0.37	0.23	1570	986.4	2	6.62	0	-	0	-
120.	EDI	300.4	1622	0.3	0.18	1373	846.6	3	4.88	0	-	0	-
121.	EEI	12017	1789	0.25	0.14	921.4	515	0	0	0	-	0	-
122.	EON	3605	1680	0.31	0.18	1245	741.3	2	7.27	0	-	0	-
123.	EPI	1442	1764	0.29	0.16	1351	766	2	4.93	0	-	0	-
124.	ERI	2163	1604	0.36	0.22	1498	933.7	3	6.31	0	-	0	-
125.	ESV	2884	1771	0.28	0.16	1162	656	1	5.67	0	-	0	-
126.	ETL	4326	1801	0.23	0.13	994.6	552.3	2	5.77	0	-	0	-
127.	EUO	6729	1708	0.29	0.17	1170	684.6	1	6.26	0	-	0	-
128.	EZT	2884	1716	0.3	0.18	1241	723.3	1	5.9	0	-	0	-
129.	FER	2163	1751	0.29	0.17	1289	736.1	2	5.42	0	-	0	-
130.	FRA	3605	1561	0.34	0.22	1381	884.5	0	0	0	-	0	-
131.	GIS	961.4	1636	0.31	0.19	1686	1031	3	4.57	0	-	0	-
132.	GME	1442	1502	0.4	0.26	1734	1155	3	7.12	0	-	0	-
133.	GON	1923	1887	0.2	0.11	805	426.6	1	5.67	0	-	0	-
134.	GOO	1923	1892	0.19	0.1	828.2	437.7	2	3.94	0	-	0	-
135.	HEU	2163	2163	0.29	0.17	1336	764	2	5.22	0	-	0	-
136.	IFR	1923	1712	0.35	0.21	1331	777.8	1	6.57	0	-	0	-

S/NO	Zeolite	Mass [g/mol]	D [kg/m^3]	HVF	APV [cm^3/g]	VSA [m^2/cm$^{3]}$	GSA [m^2/g]	DPS	Di	Loading	Wt%	Total energy	Isosteric heats
137.	IFY	2884	1761	0.3	0.17	1366	775.9	2	6.39	0	-	0	-
138.	IHW	6729	1843	0.26	0.14	1074	582.6	2	6.08	0	-	0	-
139.	IMF	17304	1744	0.3	0.17	1261	723.2	2	6.7	0	-	0	-
140.	ITE	3845	1568	0.37	0.24	1449	923.7	1	7.78	0	-	0	-
141.	ITH	3365	1739	0.3	0.17	1336	768.3	3	6.3	0	-	0	-
142.	ITR	6729	1731	0.3	0.17	1341	774.6	3	5.96	0	-	0	-
143.	ITW	1442	1768	0.27	0.15	1316	744.5	1	4.16	0	-	0	-
144.	JBW	360.5	1874	0.17	0.09	847.5	452.3	1	3.86	0	-	0	-
145.	JNT	1923	2048	0.13	0.06	586.3	286.3	0	0	0	-	0	-
146.	JOZ	1202	1633	0.24	0.15	1165	713.3	3	4.42	0	-	0	-
147.	JRY	1442	1843	0.23	0.12	1119	607.3	1	4.1	0	-	0	-
148.	JSN	961.4	1783	0.27	0.15	1206	676.2	1	4.53	0	-	0	-
149.	JST	2884	1428	0.38	0.27	2354	1649	3	4.95	0	-	0	-
150.	JSW	2884	1838	0.22	0.12	970	527.9	0	0	0	-	0	-
151.	LAU	1442	1796	0.27	0.15	1187	660.8	1	5.47	0	-	0	-
152.	LEV	3245	1589	37	0.24	1562	983.2	2	6.39	0	-	0	-
153.	LIO	2163	1759	0.27	0.15	1110	631	0	0	0	-	0	-
154.	LOS	1442	1682	0.31	0.18	1221	725.5	0	0	0	-	0	-
155.	LOV	1082	1677	0.27	0.16	1443	860.7	3	4.25	0	-	0	-
156.	LTF	1442	1414	0.47	0.33	1675	1184	3	10.24	0	-	0	-
157.	LTJ	6489	1685	0.29	0.18	1211	718.5	1	7.76	0	-	0	-
158.	MAZ	961.4	1850	0.15	0.08	607.8	328.5	3	3.63	0	-	0	-
159.	MEL	5768	1732	0.31	0.18	1282	740.4	3	6.87	0	-	0	-
160.	MEP	2764	1783	0.3	0.17	1130	633.7	0	0	0	-	0	-
161.	MER	1923	1634	0.32	0.2	1477	904.4	3	6.25	0	-	0	-
162.	MFI	5768	1838	0.27	0.14	1217	662.1	3	5.94	0	-	0	-
163.	MFS	2163	1740	0.28	0.16	1211	695.6	2	6.22	0	-	0	-
164.	MON	961.3	1761	0.23	0.13	1265	718.7	3	3.76	0	-	0	-
165.	MTF	2644	2069	0.2	0.1	799.9	386.6	1	5.59	0	-	0	-
166.	MTN	8171	1713	0.34	0.2	1223	713.7	0	0	0	-	0	-
167.	MTT	2565	3231	0.09	0.03	534.5	165.4	1	3.23	0	-	0	-
168.	MTW	1682	1819	0.24	0.13	985.6	541.8	1	5.31	0	-	0	-
169.	MVY	721	2093	0.06	0.03	163.9	78.28	1	3	0	-	0	-
170.	NAT	1202	1620	0.3	0.19	1495	922.4	3	3.95	0	-	0	-
171.	NES	8171	1641	0.34	0.21	1357	827.3	2	6.17	0	-	0	-
172.	NON	5287	1760	0.25	0.14	900.9	511.8	0	0	0	-	0	-
173.	NSI	721	1874	0.14	0.08	728.1	388.6	1	3.46	0	-	0	-
174.	OFF	1082	1606	0.36	0.22	1504	936.4	3	6.51	0	-	0	-
175.	OSI	1923	1770	0.23	0.13	893.9	505.1	1	6.26	0	-	0	-
176.	OSO	540.8	1329	0.44	0.33	1985	1493	3	5.67	0	-	0	-
177.	OWE	961.4	1709	0.32	0.18	1464	856.3	2	5.22	0	-	0	-

S/NO	Zeolite	Mass [g/mol]	D [kg/m^3]	HVF	APV [cm^3/g]	VSA [m^2/cm$^{3]}$	GSA [m^2/g]	DPS	Di	Loading	Wt%	Total energy	Isosteric heats
178.	PAR	1987	1878	0.13	0.07	740	394	1	3.69	0	-	0	-
179.	PHI	1923	1634	0.32	0.2	1601	979.8	3	5	0	-	0	-
180.	PSI	8652	2052	0.11	0.06	467.8	228	1	5.35	0	-	0	-
181.	PUN	2163	1493	0.38	0.26	2020	1353	3	4.99	0	-	0	-
182.	RON	3237	1829	0.23	0.13	1078	589.4	1	5.11	0	-	0	-
183.	RRO	1082	1782	0.24	0.13	1293	725.4	2	3.87	0	-	0	-
184.	RSN	2163	1677	0.25	0.15	1336	796.5	3	4.26	0	-	0	-
185.	RTE	1442	1712	0.31	0.18	1287	751.5	1	6.42	0	-	0	-
186.	RTH	541.8	1605	0.37	0.23	1441	897.7	1	7.64	0	-	0	-
187.	RUT	2163	1809	0.26	0.14	1097	606.5	0	0	0	-	0	-
188.	RWR	1923	1916	0.18	0.09	801.1	418.1	1	3.92	0	-	0	-
189.	SAF	3845	1896	0.22	0.11	801.4	422.8	1	6.24	0	-	0	-
190.	SAS	1923	1491	0.4	0.27	1448	971.3	1	8.55	0	-	0	-
191.	SAT	4326	1638	0.32	0.2	1296	791.4	3	6.18	0	-	0	-
192.	SEW	3966	1698	0.34	0.2	1433	844.1	2	6.24	0	-	0	-
193.	SFE	745.2	1496	0.26	0.18	1186	792.9	1	6.24	0	-	0	-
194.	SFF	1923	1781	0.32	0.18	1281	719.2	1	7.09	0	-	0	-
195.	SFG	4446	1760	0.26	0.15	1058	601.1	2	6.36	0	-	0	-
196.	SFW	6489	1505	0.4	0.26	1689	1122	3	7.14	0	-	0	-
197.	SGT	3845	1742	0.31	0.18	1107	635.5	0	0	0	-	0	-
198.	SIV	3845	1633	0.32	0.19	1640	1004	3	4.98	0	-	0	-
199.	SOD	721	1662	0.33	0.2	1298	781.1	0	0	0	-	0	-
200.	SOF	2403	1638	0.35	0.22	1793	1094	3	4.74	0	-	0	-
201.	SOS	1442	1693	0.27	0.16	1659	979.7	1	4.39	0	-	0	-
202.	SSY	1682	1684	0.28	0.17	1173	696.9	1	6.94	0	-	0	-
203.	STF	1923	1684	0.35	0.21	1363	809.4	1	7.22	0	-	0	-
204.	STI	4326	1666	0.35	0.21	1477	886.4	2	5.82	0	-	0	-
205.	STO	6729	1866	0.23	0.12	861.4	461.7	1	6.4	0	-	0	-
206.	STT	3845	1692	0.33	0.2	1386	819.1	1	6.57	0	-	0	-
207.	STW	3605	3605	0.37	0.22	3605	1052	3	4.91	0	-	0	-
208.	SVR	5656	1756	0.28	0.16	1259	717.3	3	5.34	0	-	0	-
209.	SVV	3365	1799	0.27	0.15	1116	620.7	0	0	0	-	0	-
210.	SZR	2163	1759	0.26	0.15	1166	662.8	3	5.59	0	-	0	-
211.	TER	4807	1700	0.32	0.19	1407	827.2	2	6.18	0	-	0	-
212.	THO	600.8	1571	0.31	0.2	1503	956.7	3	4.48	0	-	0	-
213.	TON	1442	1810	0.22	0.12	951.6	525.7	1	5.04	0	-	0	-
214.	UEI	2884	1742	0.22	0.13	998	572.9	2	5.12	0	-	0	-
215.	UOS	1442	1758	0.26	0.15	1246	708.9	2	5.32	0	-	0	-
216.	UOZ	2403	1950	0.21	0.11	976.4	500.8	0	0	0	-	0	-
217.	VET	1021	2013	0.18	0.09	777.4	386.1	1	5.98	0	-	0	-
218.	VNI	3605	1753	0.19	0.11	899.1	513	2	4.4	0	-	0	-

S/NO	Zeolite	Mass [g/mol]	D [kg/m^3]	HVF	APV [cm^3/g]	VSA [m^2/cm$^{3]}$	GSA [m^2/g]	DPS	Di	Loading	Wt%	Total energy	Isosteric heats
219.	VSV	2163	1676	0.24	0.14	1243	741.7	3	3.75	0	-	0	-
220.	WEI	1202	1647	0.28	0.17	1636	993.6	3	3.79	0	-	0	-
221.	WEN	1186	1630	0.32	0.2	1445	886.7	3	4.97	0	-	0	-
222.	YUG	961.4	1791	0.22	0.12	1044	583.1	2	4.02	0	-	0	-
223.	ZON	1923	1801	0.26	0.14	1150	638.8	1	5.21	0	-	0	-
224.	AVE	-	-	-	-	-	-	-	-	0	-	0	-
225.	ETV	-	-	-	-	-	-	-	-	0	-	0	-
226.	EWO	-	-	-	-	-	-	-	-	0	-	0	-
227.	EWS	-	-	-	-	-	-	-	-	0	-	0	-
228.	FAR	5047	1705	0.29	0.17	1148	673.5	0	0	0	-	0	-
229.	GIU	5768	1709	0.29	0.17	1118	653.9	0	0	0	-	0	-
230.	ITN	-	-	-	-	-	-	-	-	0	-	0	-
231.	LIT	1506	2004	0.01,	0.01	0	0	0	0	0	-	0	-
232.	MAR	4326	1773	0.27	0.15	1066	601.2	0	0	0	-	0	-
233.	MOR	2884	1694	0.31	0.18	1266	747.3	2	6.2	0	-	0	-
234.	MRE	2884	1961	0.17	0.09	698.9	356.4	1	5.74	0	-	0	-
235.	MRT	-	-	-	-	-	-	-	-	0	-	0	-
236.	NPO	360.5	1867	0.12	0.06	607	325.2	1	3.34	0	-	0	-
237.	POR	-	-	-	-	-	-	-	-	0	-	0	-
238.	PTO	-	-	-	-	-	-	-	-	0	-	0	-
239.	PTT	-	-	-	-	-	-	-	-	0	-	0	-
240.	PTY	-	-	-	-	-	-	-	-	0	-	0	-
241.	PWW	-	-	-	-	-	-	-	-	0	-	0	-
242.	SBN	600.8	1611	0.29	0.18	1564	971.1	2	4.41	0	-	0	-
243.	SWY	-	-	-	-	-	-	-	-	0	-	0	-
244.	TOL	4326	1782	0.26	0.15	1040	583.4	0	0	0	-	0	-
245.	UOE	-	-	-	-	-	-	-	-	0	-	0	-

Appendix 2: Adsorption thermodynamics for organic pollutants

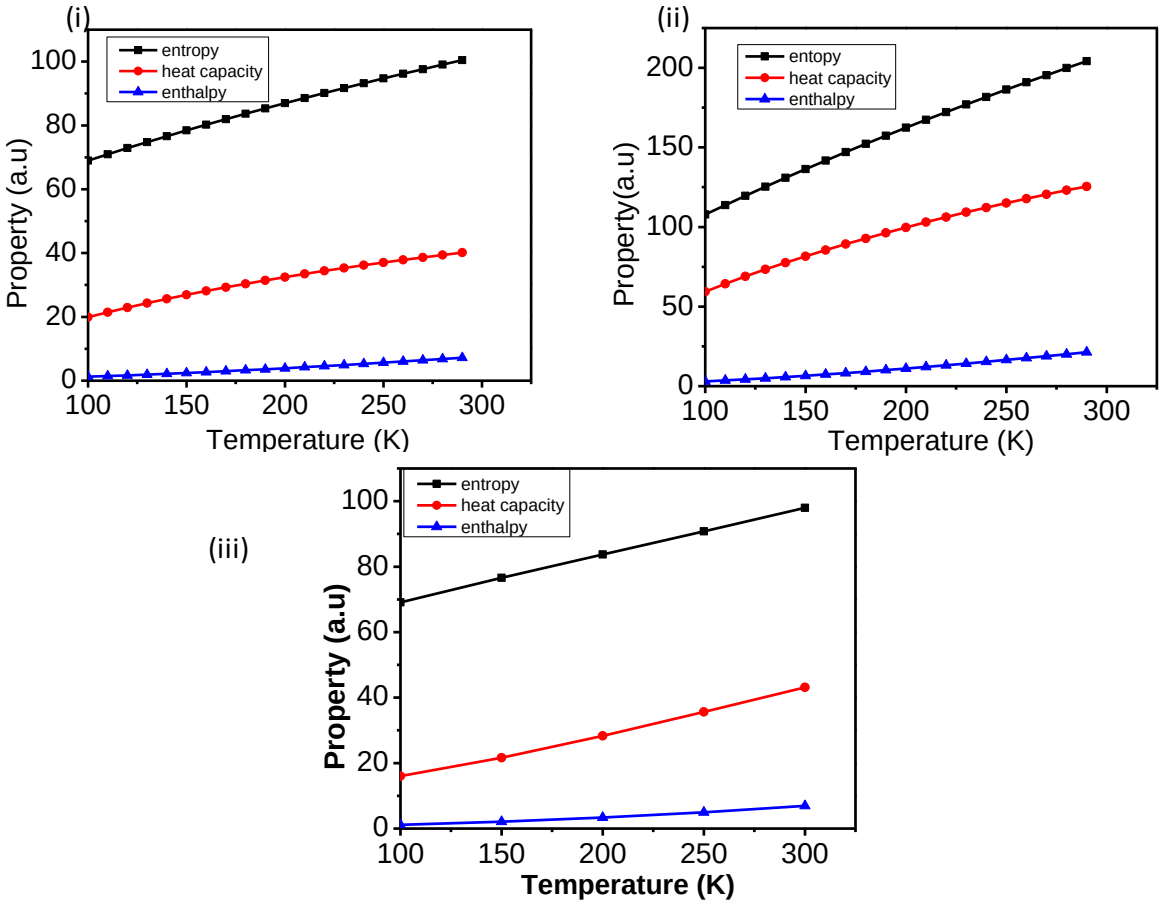

Figure Ap 4.1a Adsorption isotherms for organochlorine pesticides (OCPs); (i) hexachlorobenzene, (ii) hexachlorocyclohexane and (iii) Dichlorodiphenyltrichloroethane respectively

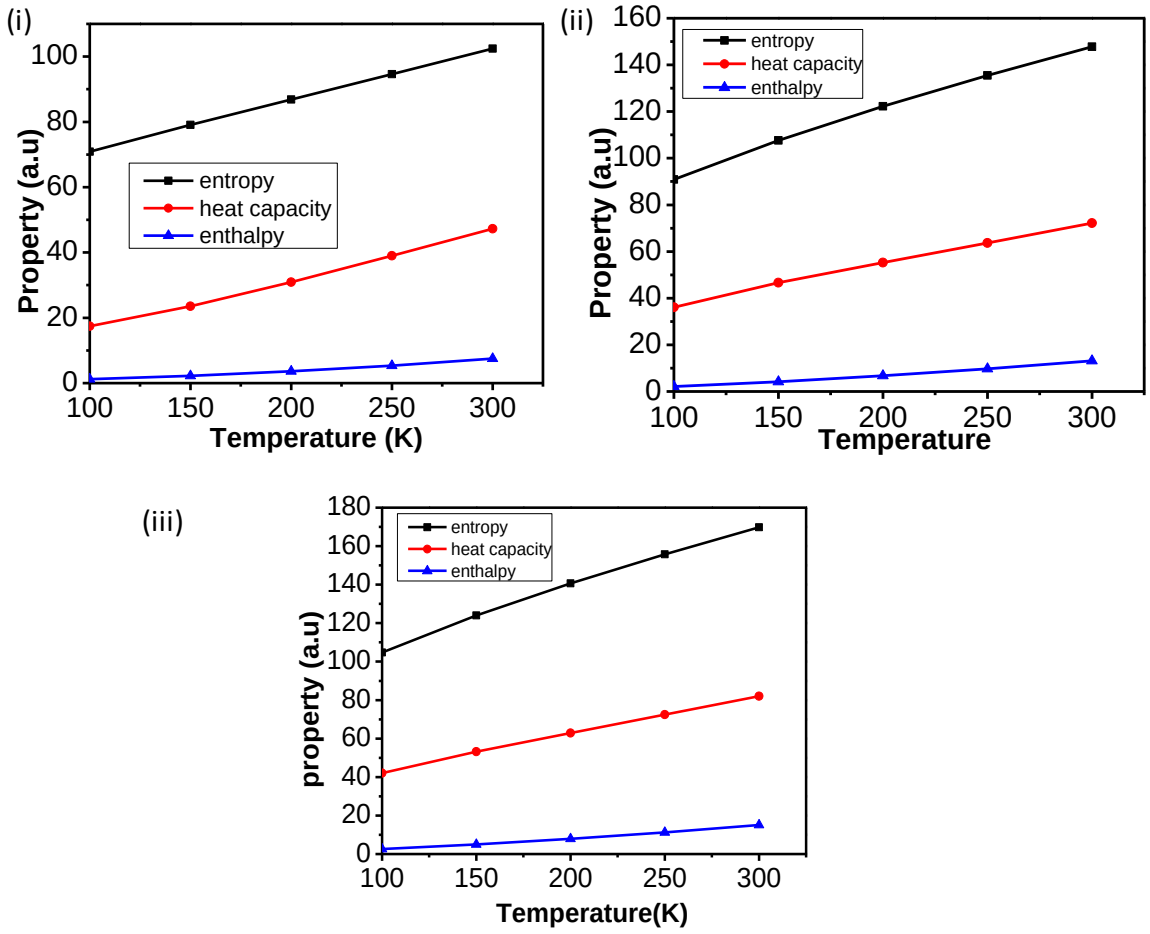

Figure Ap 4.1b Adsorption thermodynamics of short chain chlorinated paraffins (SCCPs); (i) $C_{10}H_{16}Cl_6$, (ii) $C_{10}H_{15}Cl_7$, (iii) $C_{11}H_{16}Cl_6$

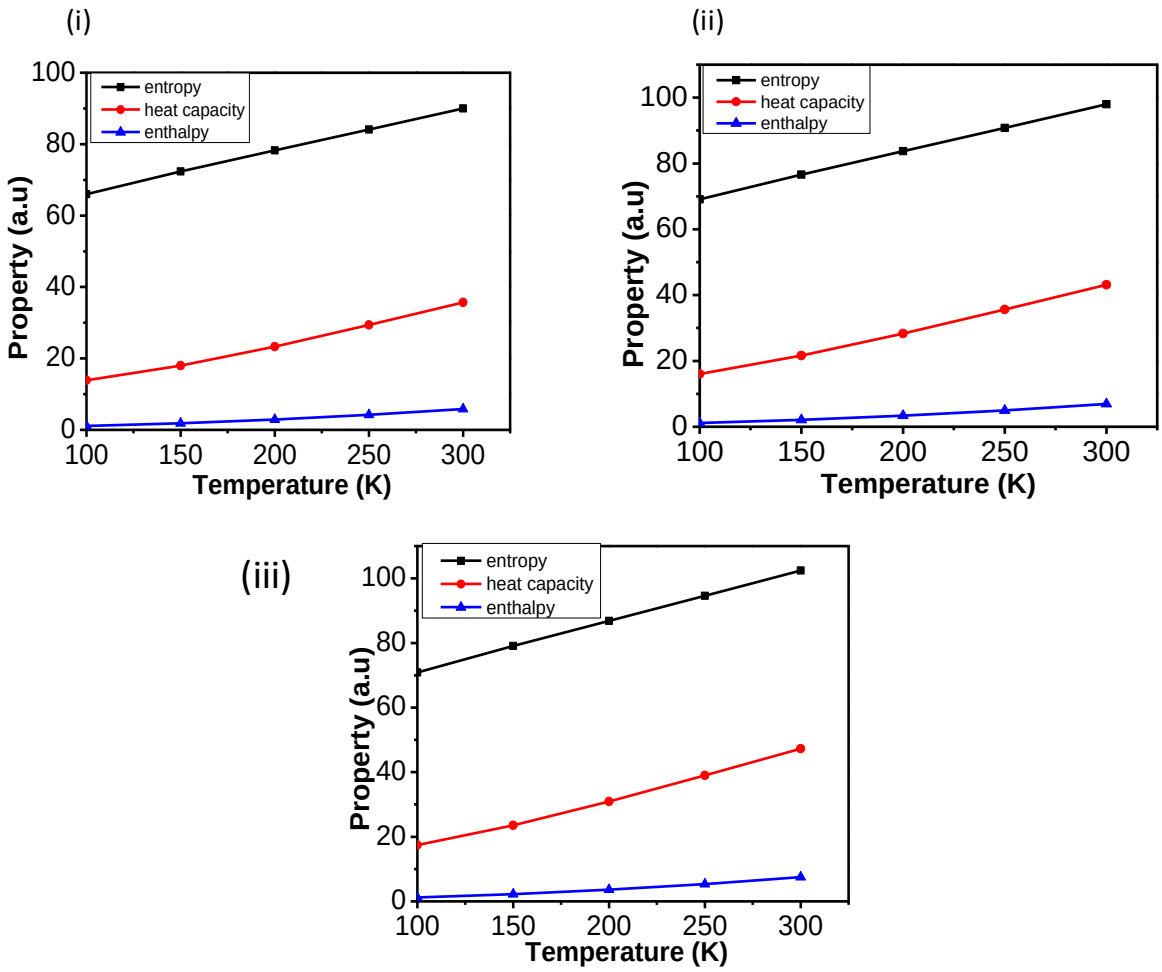

Figure 4.1c Adsorption thermodynamics of polycyclic aromatic hydrocarbons (PAHs);

(i) Phenanthrene, (ii) Fluoranthene, (iii) Acenaphthylene

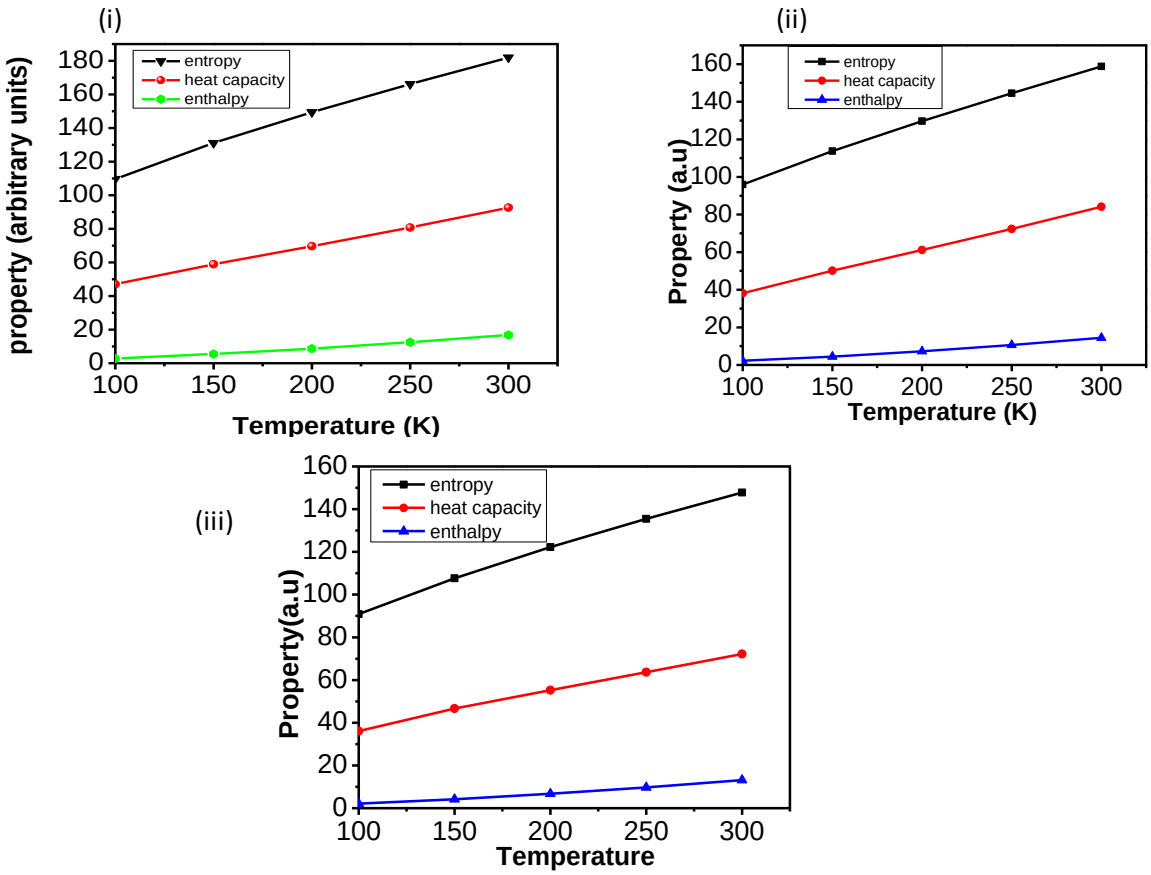

Figure 4.1d: Adsorption thermodynamics of medium chain chlorinated paraffins (MCCPs); (i) $C_{14}H_{24}C_{l6}$, (ii) $C_{14}H_{23}Cl_7$, (ii) $C_{14}H_{22}Cl_8$.

Appendix 3 Thermodynamic parameters

Table Ap 4.13 Organochlorine pesticides standard thermodynamic quantities computed from 25.00 to 1000.00 in steps of 25.00

Temperature T (K)	Entropy S (cal/mol.K)	Heat capacity C_p (cal/mol.K)	Enthalpy H (kcal/mol)	Free energy G (kcal/mol)
25	57.118	10.1	25.696	24.269
50	65.226	13.711	25.994	22.733
75	71.564	17.928	26.388	21.021
100	77.315	22.205	26.891	19.159
125	82.69	26.028	27.495	17.158
150	87.737	29.359	28.188	15.027
175	92.486	32.28	28.959	12.774
200	96.969	34.875	29.799	10.405
225	101.214	37.207	30.701	7.928
250	105.245	39.324	31.658	5.346
275	109.086	41.261	32.665	2.667
298.15	112.487	42.916	33.64	0.102
300	112.753	43.043	33.72	-0.106
325	116.264	44.688	34.816	-2.969
350	119.632	46.209	35.953	-5.918
375	122.869	47.617	37.126	-8.95
400	125.984	48.919	38.333	-12.061
425	128.987	50.124	39.571	-15.248
450	131.884	51.238	40.838	-18.509
475	134.682	52.268	42.132	-21.842
500	137.387	53.219	43.451	-25.243
525	140.006	54.099	44.793	-28.71
550	142.541	54.911	46.155	-32.242
575	144.999	55.662	47.538	-35.837
600	147.383	56.356	48.938	-39.492
625	149.697	56.998	50.355	-43.205
650	151.944	57.593	51.788	-46.976
675	154.128	58.144	53.234	-50.802
700	156.252	58.654	54.694	-54.682
725	158.318	59.128	56.167	-58.614

Temperature T (K)	Entropy S (cal/mol.K)	Heat capacity C_p (cal/mol.K)	Enthalpy H (kcal/mol)	Free energy G (kcal/mol)
750	160.33	59.568	57.651	-62.597
775	162.29	59.977	59.145	-66.63
800	164.201	60.358	60.649	-70.711
825	166.063	60.713	62.163	-74.84
850	167.881	61.044	63.685	-79.014
875	169.655	61.353	65.215	-83.233
900	171.387	61.641	66.752	-87.497
925	173.08	61.912	68.297	-91.802
950	174.734	62.165	69.847	-96.15
975	176.352	62.402	71.405	-100.539
1000	177.935	62.625	72.967	-104.968

Table Ap 4.14 Medium chain chlorinated paraffins standard thermodynamic quantities computed from 25.00 to 1000.00 in steps of 25.00

Temperature T (K)	Entropy S (cal/mol.K)	Heat capacity C_p (cal/mol.K)	Enthalpy H (kcal/mol)	Free energy G (kcal/mol)
25	81.575	25.057	126.75	124.71
50	105.76	47.399	127.654	122.366
75	129.084	68.726	129.11	119.429
100	151.487	87.443	131.068	115.92
125	172.762	103.402	133.459	111.864
150	192.853	117.078	136.219	107.292
175	211.817	129.026	139.299	102.231
200	229.753	139.657	142.66	96.709
225	246.765	149.238	146.273	90.751
250	262.946	157.93	150.114	84.378
275	278.375	165.837	154.163	77.61
298.15	292.049	172.525	158.081	71.006
300	293.118	173.034	158.4	70.465
325	307.231	179.583	162.809	62.959
350	320.761	185.536	167.374	55.108
375	333.749	190.945	172.082	46.926
400	346.232	195.859	176.918	38.425
425	358.242	200.325	181.871	29.618
450	369.809	204.384	186.93	20.516

Temperature T (K)	Entropy S (cal/mol.K)	Heat capacity C_p (cal/mol.K)	Enthalpy H (kcal/mol)	Free energy G (kcal/mol)
475	380.96	208.079	192.087	11.131
500	391.72	211.448	197.332	1.472
525	402.112	214.523	202.657	-8.452
550	412.158	217.338	208.056	-18.631
575	421.876	219.919	213.522	-29.057
600	431.287	222.292	219.05	-39.722
625	440.406	224.48	224.635	-50.619
650	449.25	226.502	230.272	-61.74
675	457.834	228.377	235.959	-73.079
700	466.172	230.119	241.69	-84.63
725	474.275	231.744	247.464	-96.386
750	482.158	233.262	253.277	-108.342
775	489.83	234.684	259.126	-120.492
800	497.302	236.02	265.01	-132.832
825	504.584	237.278	270.926	-145.356
850	511.685	238.465	276.873	-158.059
875	518.614	239.587	282.849	-170.938
900	525.379	240.651	288.852	-183.989
925	531.986	241.66	294.881	-197.206
950	538.444	242.62	300.935	-210.587
975	544.758	243.534	307.012	-224.127
1000	550.935	244.406	313.111	-237.824

Table Ap 4.15 Short chain chlorinated paraffins standard thermodynamic quantities

computed from 25.00 to 1000.00 in steps of 25.00

Temperature T (K)	Entropy S (cal/mol.K	Heat capacity C_p (cal/mol.K)	Enthalpy H (kcal/mol)	Free energy G (kcal/mol)
25	64.083	11.51	98.306	96.704
50	76.164	26.034	98.762	94.954
75	89.818	42.171	99.618	92.882
100	103.93	56.203	100.853	90.46
125	117.773	67.969	102.409	87.688
150	131.071	77.955	104.236	84.576
175	143.754	86.637	106.296	81.139
200	155.836	94.349	108.56	77.393
225	167.356	101.295	111.007	73.352
250	178.36	107.595	113.62	69.029

Temperature T (K)	Entropy S (cal/mol.K	Heat capacity C_p (cal/mol.K)	Enthalpy H (kcal/mol)	Free energy G (kcal/mol)
275	188.888	113.32	116.382	64.438
298.15	198.243	118.15	119.062	59.956
300	198.975	118.518	119.281	59.589
325	208.65	123.23	122.304	54.493
350	217.941	127.494	125.439	49.159
375	226.871	131.348	128.675	43.599
400	235.461	134.828	132.003	37.819
425	243.731	137.971	135.414	31.828
450	251.699	140.811	138.899	25.635
475	259.382	143.381	142.452	19.246
500	266.797	145.71	146.066	12.668
525	273.958	147.826	149.736	5.908
550	280.88	149.754	153.456	-1.028
575	287.576	151.515	157.222	-8.134
600	294.06	153.131	161.031	-15.405
625	300.341	154.617	164.878	-22.836
650	306.432	155.99	168.76	-30.421
675	312.344	157.262	172.676	-38.156
700	318.085	158.446	176.623	-46.036
725	323.664	159.551	180.598	-54.059
750	329.091	160.586	184.6	-62.218
775	334.372	161.559	188.627	-70.512
800	339.516	162.476	192.677	-78.936
825	344.529	163.344	196.75	-87.487
850	349.418	164.167	200.844	-96.161
875	354.188	164.949	204.958	-104.957
900	358.845	165.694	209.091	-113.87
925	363.395	166.405	213.242	-122.898
950	367.842	167.085	217.411	-132.039
975	372.19	167.737	221.597	-141.289
1000	376.445	168.363	225.798	-150.647

Appendix 4: Adsorption sites

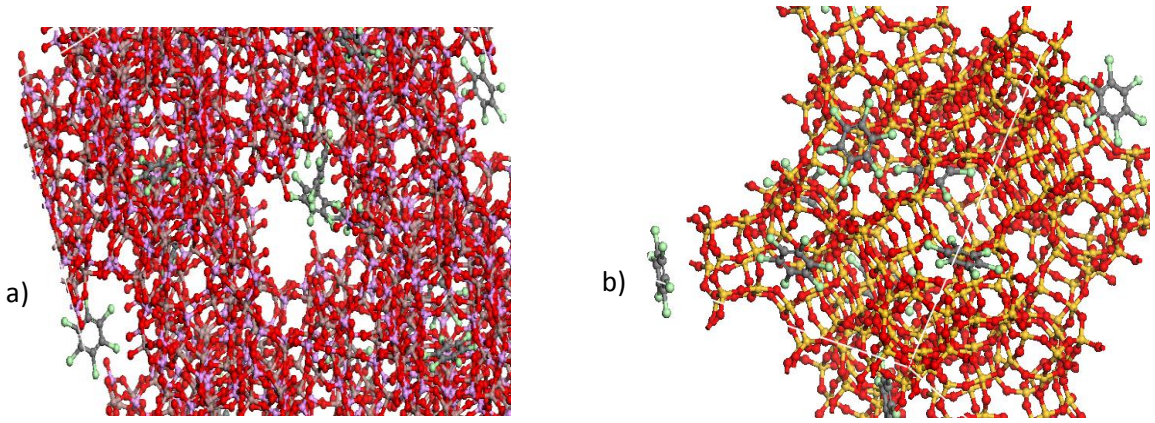

Figure Ap 4.3: Adsorption sites for HCB on CLO (a) and TSC (b).

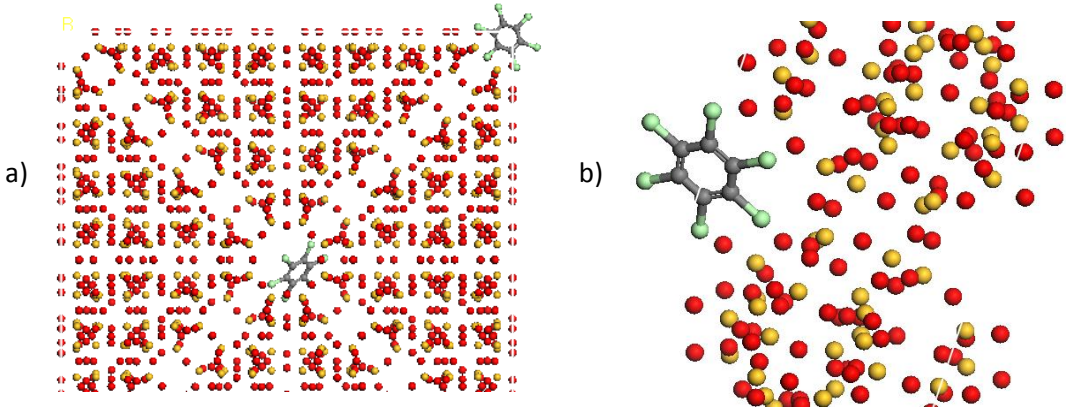

Figure: Ap 4.4: Adsorption locator for MWF (a) and IWW (b), respectively.

a)

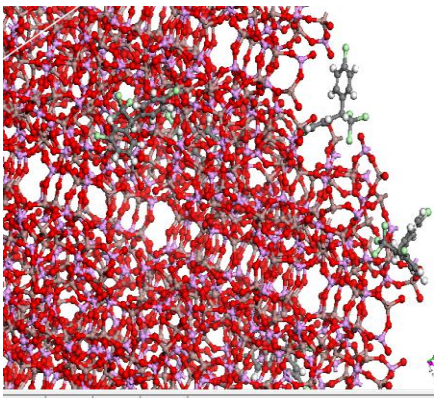

b)

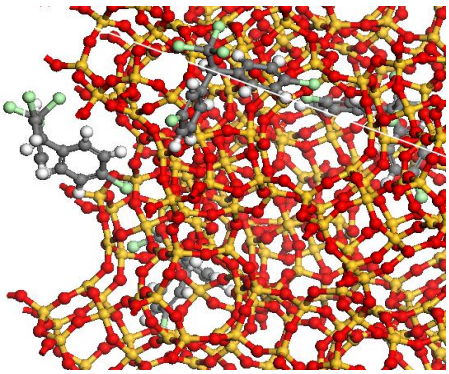

Figure Ap 4.5: Adsorption sites for DDT on CLO (a) and TSC (b) respectively

a)

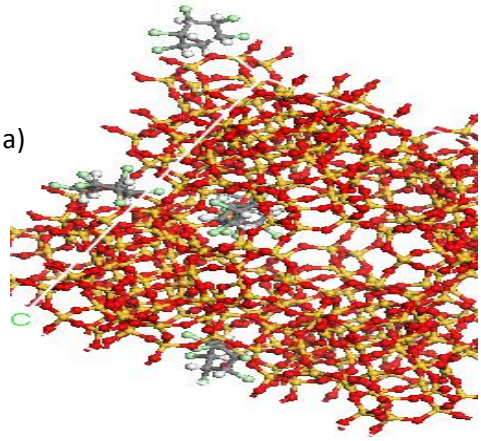

b)

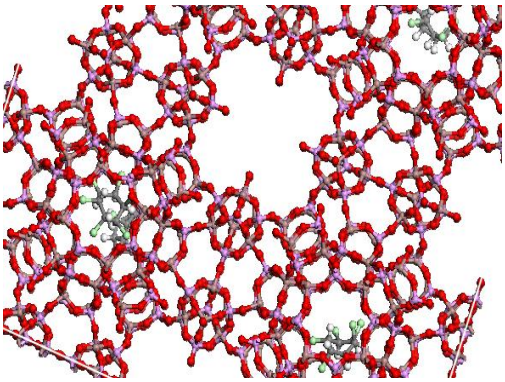

Figure Ap 4.6: Adsorption sites for HCH on TSC (a) and CLO (b) zeolite, respectively.

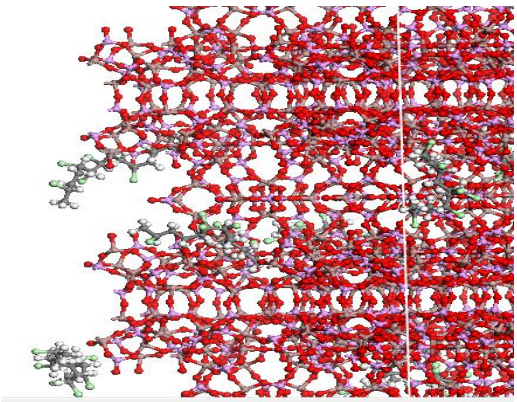

a) Adsorption of C14H24Cl6 on CLO

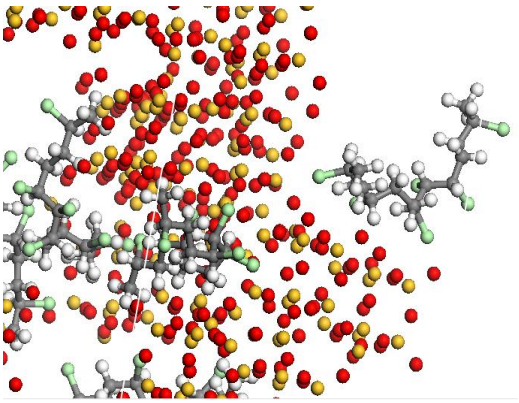

b) Adsorption of C14H23Cl7 on ITV

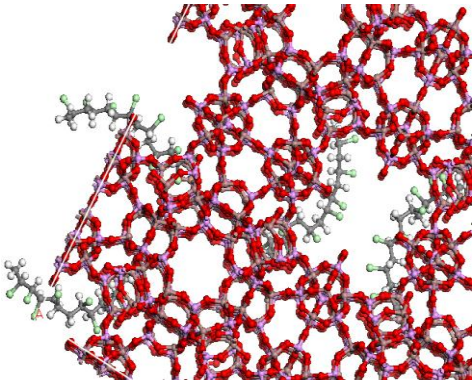

c) Adsorption of octachlorodecane on CLO

Figure Ap 4.7: Adsorption sites for MCCPs

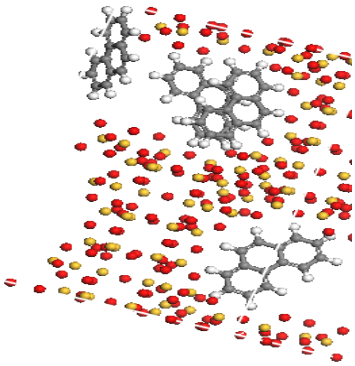

a) Adsorption of phenanthrene on SBS

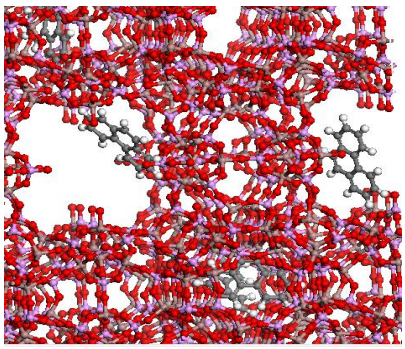

b) Adsorption of phenanthrene on CLO

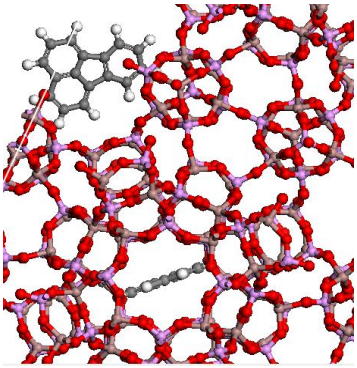

c) Adsorption of Fluoranthrene on CLO

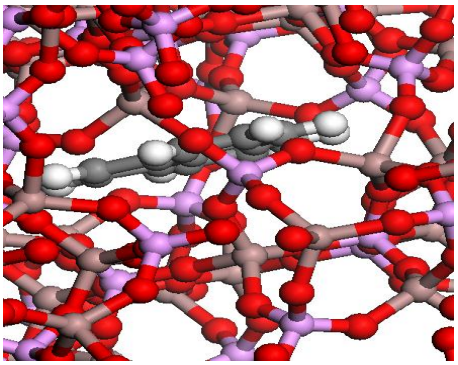

d) Adsorption of acenaphthylene on CLO

Figure Ap 4.8: Adsorption sites for PAHs.

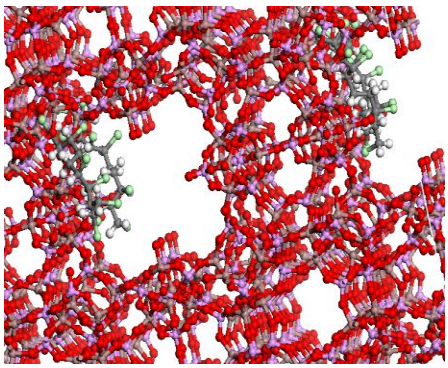

a) Adsorption of heptachlorodecane on CLO

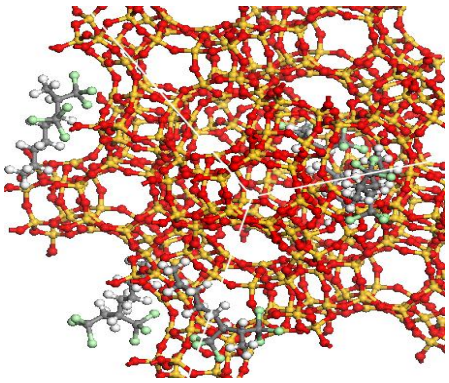

b) Adsorption of hexachlorodecane on TSC

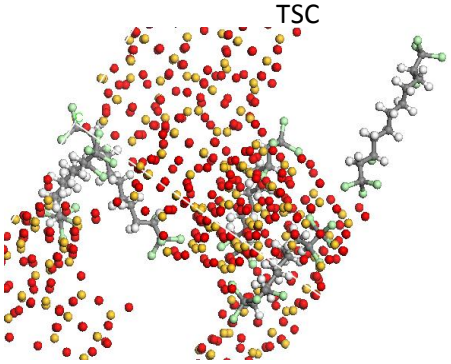

c) Adsorption of octachloroundecane on ITV

Figure Ap 4.9: Adsorption sites for SCCPs.

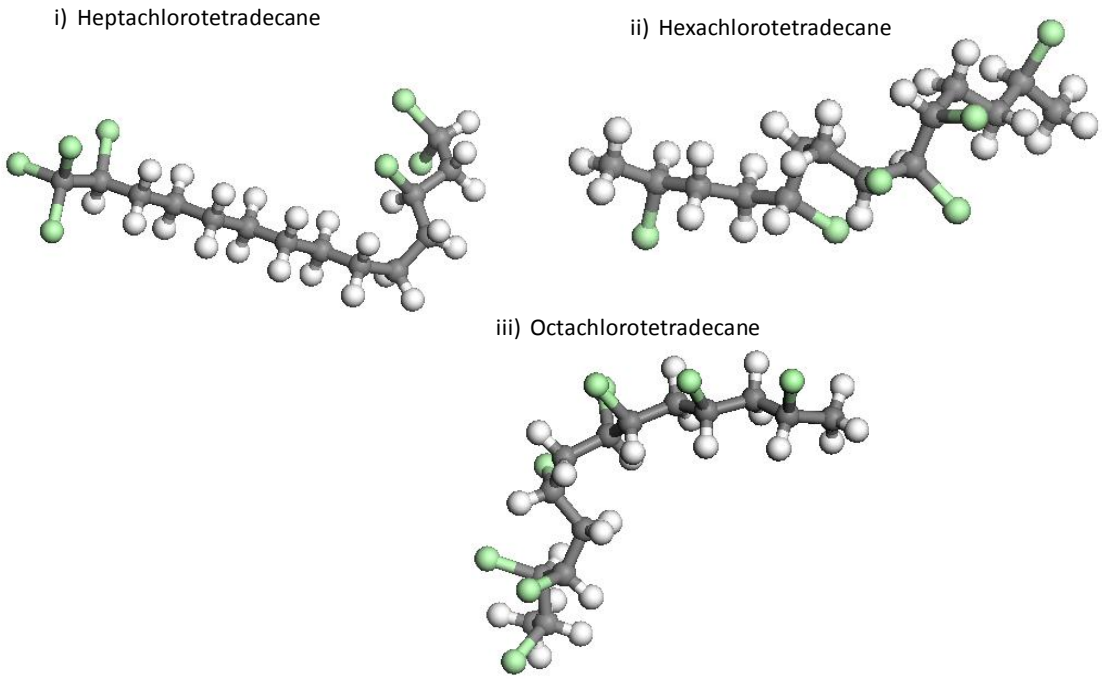

Figure Ap 4.10a: Studied medium chain chlorinated parraffins

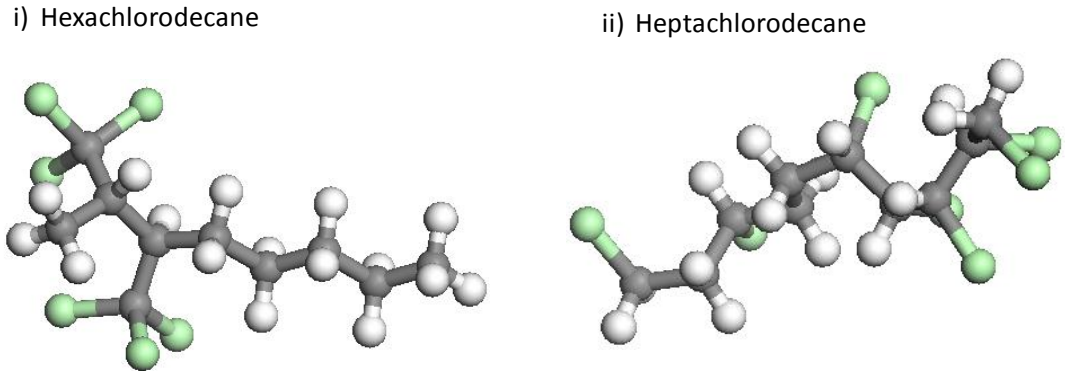

Figure Ap 4.10b Studied short chain chlorinated parraffins

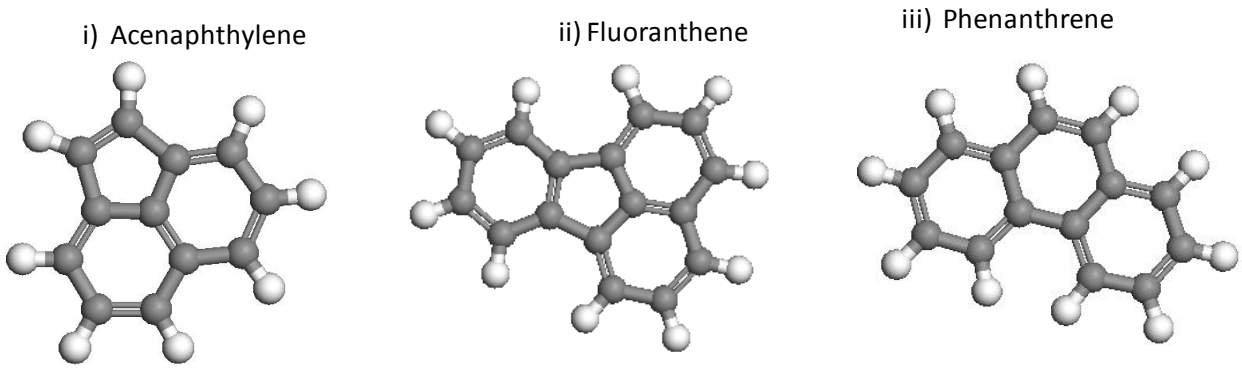

Figure Ap 4.10c: Studied Polycyclic aromatic hydrocarbons

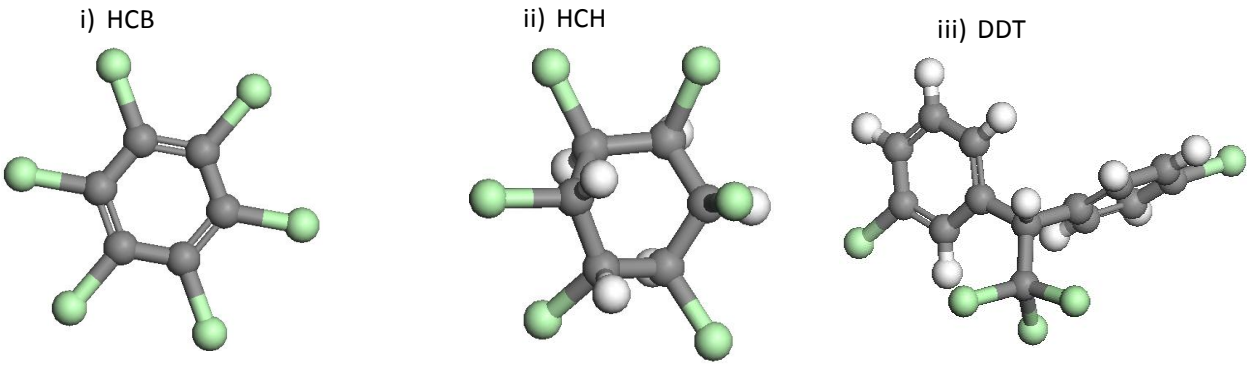

Figure Ap 4.10d Studied organochlorine pesticides

Appendix 5: A draft manuscript on Hydrogen storage by zeolites

A Data Guided Approach for the Evaluation of Zeolites for Hydrogen Storage with the Aid of Molecular Simulations

Timothy Manda [1], Godfrey Okumu Barasa[1], Hitler Louis[2], Ahmad Irfan[3], John Onyango Agumba[1], Solomon Omwoma Lugasi[1], Anthony M.S. Pembere[1*]*

[1]Department of Physical Sciences, Jaramogi Oginga Odinga University of Science and Technology, P.O Box 210, Bondo 40601, Kenya

[2]Computational Quantum Chemistry Research Group, Department of Pure and Applied Chemistry, Faculty of Physical Sciences, University of Calabar, 1115 Calabar, Nigeria
[3]Department of Chemistry, College of Science, King Khalid University, Abha 61413, Saudi Arabia.

*Correspondence Email: gobarasa@jooust.ac.ke/apembere@jooust.ac.ke

Abstract

Grand Canonical Monte Carlo (GCMC) simulations have been used to evaluate the hydrogen storage performance on 233 zeolites. LTA had the highest capacity with a hydrogen capacity of 4.8 %wt. The second ranked zeolite is JBW with a hydrogen uptake capacity of 3.25 % wt, while RTH was the third with 2.89 % wt. A machine learning algorithm was used to rank the importance of various structural features such as mass (M), density (D), helium void fraction (HVF), accessible pore volume (APV), gravimetric surface area (GSA), and largest overall cavity diameter (Di) and how they affect the capacity of the zeolites. The results show that Di, D and M have a negative effect on the percentage weight capacity, while GSA and VSA have the highest positive contribution to the percentage weight. From this, the best material could be achieved by reducing the mass and density while increasing both gravimetric and volumetric surface area. Further quantum chemical calculations were also performed to calculate the adsorption energy, global reactivity electronic descriptors, and natural bond orbital analysis in order to provide insights into the interaction of the zeolites with hydrogen.

Key words: Zeolites, Hydrogen Storage, Molecular Simulations, Machine learning

1.0 Introduction

Zeolites are nanoporous materials that are manmade or naturally occurring and have cavities that are well defined[1,2]. Based on their peculiar adsorption properties, they are interesting candidates for various applications[3–5], including hydrogen storage[3]. As a fuel, despite having low density, every unit mass of hydrogen has a very high energy of combustion. There are several storage modes that have been developed over years, for example high pressure gas storage, liquid hydrogen, glass microspheres and activated carbon[2]. The traditionally used materials for the storage of hydrogen are metals and alloys that are based on transition metals. The storage of hydrogen in zeolites has recently won the attention of many scientists. For example, the use of zeolites as hydrogen storage media has been experimentally investigated using several zeolites of different pore architecture and composition at temperatures from 293 to 573K and pressures from 2.5 to 10.0 MPa[6], whereby zeolites with sodalite cages are preferred[8]. Elsewhere, the hydrogen-storage of Na-LEV, H-OFF, Na-MAZ and Li-ABW have been studied at 77 K[7], with Na-LEV having the highest hydrogen storage capacity followed by H-OFF. It was revealed that a suitable diameter near to the kinetic diameter of a hydrogen molecule is the main factor that enhances the hydrogen-storage capacity[7].

On the other hand, molecular simulations have also been applied in evaluating the storage capacity of hydrogen on zeolites. For example, a study to investigate the performance of several zeolite templated carbons (ZTC) in the storage of hydrogen has been done[8]. RHO had the highest H_2 loading[8]. Among the studies that have been done up to date, there has been no research that has shown attempts to study all zeolites classifying them according to their loading capacity.

There are around 240 zeolites in the zeolite database of which a number of them could be of great importance in storage of hydrogen rather than a few selected. In this study, the adsorption of hydrogen inside the pores of zeolites was studied using molecular simulations and machine learning. Molecular simulations do provide a theoretical framework which is based on statistical mechanics. For example, with molecular simulations we can compute the number of particles that are absorbed into a surface pore at a given pressure. This properties of a much smaller system[9,10]. Thus, for the 242 zeolite structures, data showing loading capacity was generated by Monte Carlo simulations. A machine learning algorithm was employed to rank the importance of how and to what extent each of the descriptors influences the loading capacity of hydrogen on the zeolite framework.enables us to carry out investigation on a compound with a larger number of molecules by examining the statistical

2.0 Methods

The IZA structure database [11], was the source of the zeolite structures used in this study. They were optimized using material studio[12] Forcite module[13]. Openly available data repository, PubChem[14] was the source for the molecular structure of hydrogen. Geometry optimization and frontier molecular orbital analysis of hydrogen was done using DMol[3] module[15,16], prior to Monte Carlo simulations. The Monte Carlo simulations were performed using material studio 2017 software[12]. Various forcefields are embedded in material studio, including universal,[17] dreiding[13], compass[18] and the consistent-valence forcefield (cvff)[19]. In this study, we first compared the results of various forcefields as seen in Figure 1 a) and b). We found that the universal forcefield is relatively suitable for the systems used in this study.

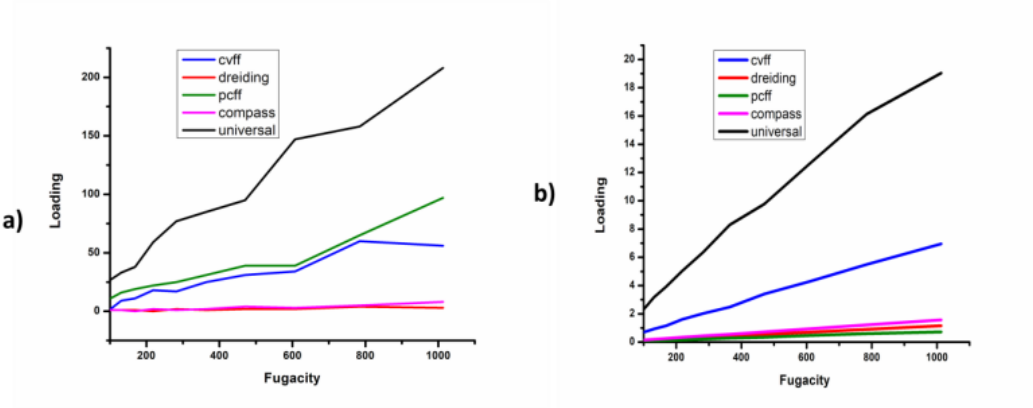

Figure 1: Loading results for representative zeolites using various forcefields; a) MWF zeolite, b) LTA zeolite.

To carry out sorption calculations of zeolites, the symmetry of the zeolites was changed to P1 since sorption calculations require structures without any symmetry[20,21]. There was a need to set the upper and lower fugacity at which calculations would be performed and the number of intervals between them, thus the lower fugacity of 1 atm and an upper fugacity of 10 atm were used. Sorption program in material studio software provides five different simulation tasks that model the adsorption of molecules into porous 3D frameworks[12]. First, the fixed pressure task is used to model the adsorption of sorbate molecules in a sorbent lattice using a grand canonical ensemble. Secondly, the fixed loading task is used to model the adsorption of sorbate molecules in a sorbent lattice using a canonical ensemble. Thirdly, the Henry constant task is used to calculate the Henry constant for a sorbate molecule in a sorbent lattice. Lastly, the adsorption isotherm task is used to derive a plot of average cell loading against pressure for sorbate molecules in a sorbent lattice and the locate task is used to find the global minimum energy sites for sorbate molecules in a sorbate lattice. During the course of the simulation, sorbate molecules within the framework are randomly rotated and translated, and, in addition, sorbates are randomly created in and deleted from the framework. The framework network of adsorbents

differentiates them and gives them a special application. For instance, LTA zeolite shown in figure 2 (a) below has different channels which are interconnected. The connected channels are all of same length, 4.1Å. This gives it a different energy requirement for adsorption.

Quantum chemical calculations to study the interaction between the zeolites, with hydrogen were also performed. All ground state computational calculations of the studied zeolite systems were performed within the framework of density functional theory with Gaussian 09[22]. Pre-geometry optimization of the metal-surfactant complexes were conducted with the help of molecular mechanic geometry optimization computer module embedded in the HyperChem program[23]. The output files were further utilized for geometry optimization by assigning 6-31+G(d) and LanL2DZ basis set for lighter (H and O-atoms) and heavy metal (Si) respectively. Natural bond orbital (NBO) calculation for the investigation of the stabilization energy and charge transfer was conducted with the help of the NBO 3.1 module entrenched in Gaussian[22]. Wave function analyses were done by the Multiwfn 3.7 dev[24]. Machine learning analysis was performed using Scikit-learn[25], an open-source library. Data set is divided into training and testing set with 90:10% ratios, respectively. Various machine learning models are used. The best model is further tuned by optimizing the hyper parameters.

3.0 Results and Discussion

The International Zeolite Association structure database provides structural information on all of the zeolite framework types that have been approved by the Structure Commission of the International Zeolite Association[11]. This includes crystallographic data (highest possible space group, cell constants of the idealized framework), coordination sequences, vertex symbols and composite building units. Taken together, the coordination sequences and the vertex symbols

define the framework type. Data for the type material (i.e. the real material on which the idealized framework type is based) is also given. The porous domains of zeolites are also characterized by several structural features such as mass (M), density (D), helium void fraction (HVF), accessible pore volume (APV), gravimetric surface area (GSA), and dimensionality of the pore system (Di). A GPU-accelerated visualization software iRASPA has been used to calculate Mass, Density, HVF, APV, GSA and Di as shown in table 1 and S1. The capability of hydrogen adsorption as determined from grand canonical Monte Carlo (GCMC) simulations is also shown in Table 1 (for the 20 best performing zeolites) and in table S1 (for the entire 233 zeolites). Loading (L) corresponds to the number of molecules per cell loaded in the pores of the zeolite. Percentage weight (%wt.) capacity is expressed as stored gas molecules per mass of zeolite. Among the 233 zeolites studied (Table S1, supporting information), it is noted that MWF has the largest M (86521 g/mol) with relatively higher D (1604 kg/m^3). It also has a Di of 10.06, APV of 0.22 and GSA of 993.8. It exhibits the highest loading of 225 hydrogen molecules per cell. However, in terms of percentage weight, LTA has the highest capacity of all studied materials with a hydrogen capacity of 4.8%wt. This capacity corresponds to the 36 molecules per cell loaded in the pores of this solid. This is quite surprising since it could be expected that the material with higher number of molecules per cell gives the higher percentage mass of the adsorbed molecules. LTA gains the lead as the best zeolite for hydrogen uptake due to its relatively low mass of 1442g/mol. This best performance of zeolite LTA could also be attributed to the fact that it has different types of rings in its structure as shown in figure 2(a). LTA possesses 8, 10 and 16 rings which are connected by different channels both of 4.1Å.

Table 1: The structural characteristics and loading capacity of the best performing zeolites at fixed temperature of 298K and lower fugacity of 1atm; upper fugacity 10atm

S/No.	Code	M*[g/mol]*	D*[kg/m^3]*	HVF	APV *[cm^3/g]*	VSA*[m^2/cm^3]*	GSA*[m^2/g]*	DPS	Di*[A]*	Pore size Category	L	%wt
1	LTA	1442	1414	0.47	0.33	1675	1184	3	10.24	Extra large	36	4.8
2	JBW	360.5	1874	0.17	0.09	847.5	452.3	1	3.86	Small	6	3.25
3	RTH	541.8	1605	0.37	0.23	1441	897.7	1	7.64	Extra large	8	2.89
4	THO	600.8	1571	0.31	0.2	1503	956.7	3	4.48	Medium	8	2.61
5	CLO	11728	1129	0.55	0.49	2070	1834	3	15.33	Extra large	143	2.4
6	NPO	360.5	1867	0.12	0.06	607	325.2	1	3.34	Small	4	2.19
7	NAB	600.8	1605	0.26	0.16	1585	987.5	3	3.78	Small	6	1.97
8	OSO	540.8	1329	0.44	0.33	1985	1493	3	5.67	Medium	5	1.83
9	SBN	600.8	1611	0.29	0.18	1564	971.1	2	4.41	Medium	5	1.65
10	JOZ	1202	1633	0.24	0.15	1165	713.3	3	4.42	Medium	9	1.49
11	LOV	1082	1677	0.27	0.16	1443	860.7	3	4.25	Medium	8	1.47
12	OWE	961.4	1709	0.32	0.18	1464	856.3	2	5.22	Medium	7	1.45
13	SOD	721	1662	0.33	0.2	1298	781.1	0	0	Small	5	1.38
14	NAT	1202	1620	0.3	0.19	1495	922.4	3	3.95	Small	8	1.32
15	EDI	300.4	1622	0.3	0.18	1373	846.6	3	4.88	Medium	2	1.32
16	OFF	1082	1606	0.36	0.22	1504	936.4	3	6.51	Large	7	1.29
17	RRO	1082	1782	0.24	0.13	1293	725.4	2	3.87	Small	7	1.29
18	MER	1923	1634	0.32	0.2	1477	904.4	3	6.25	Large	12	1.24
19	AFY	961.4	1409	0.48	0.34	2103	1492	3	7.42	Large	6	1.24
20	JSN	961.4	1783	0.27	0.15	1206	676.2	1	4.53	Medium	6	1.24

Table key:D= density[kg/m^3], M=mass[g/mol]; HVF=helium void fraction; APV=accessible pore volume[cm^3/g]; VSA=volumetric surface area[m^2/cm^3]; GSA=gravimetric surface area[m^2/g]; DPS=dimensionality of the pore system; Di=largest overall cavity diameter[A]; L=loading].

The pore sizes are classified as being small (≤4 angstrom), medium (4.1-5.5 angstrom), large (5.6-7.5 angstrom) or extra-large (≥7.5 angstrom)[26].

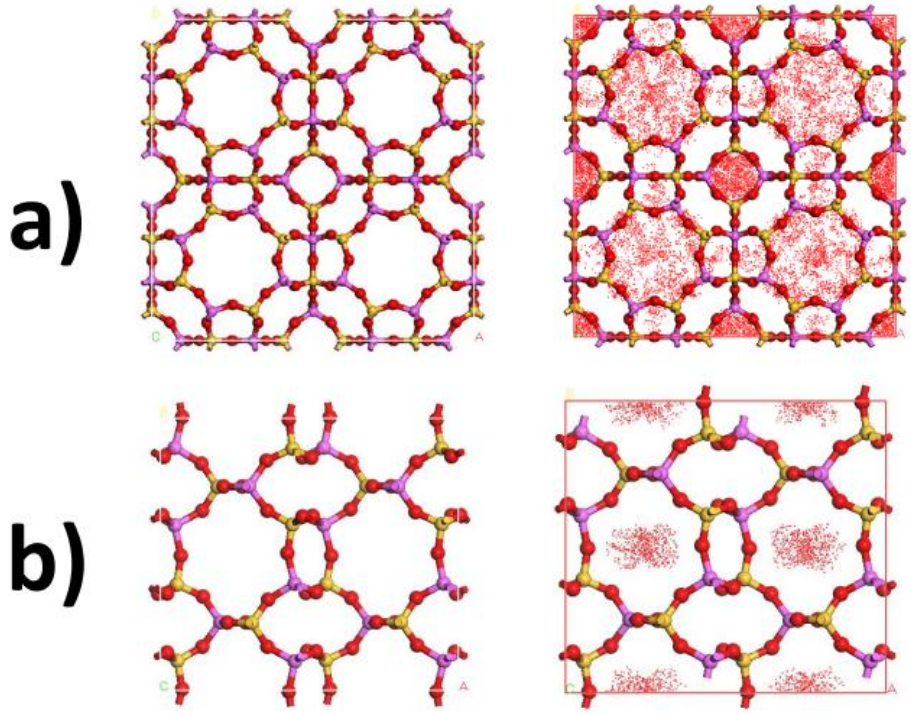

Figure 2. Structures of (a) LTA and (b) JBW (Left) before loading, (right) after loading

The second ranked zeolite is JBW (Figure 2b), with a hydrogen uptake capacity of 3.25%wt. This zeolite accommodates only six hydrogen molecules per cell, but since it has one dimensional pore system and relatively low mass, it gets a higher percentage weight. RTH zeolite, having a mass of 541.8g/mol and a comparable density of 1605kg/m^3 has a hydrogen uptake capacity of 2.89%wt. This zeolite possesses extra-large pore sizes with only 8 hydrogen molecules per cell. This shows that the smaller mass of this material and a comparable density are very important factors for its hydrogen uptake. THO zeolite with an uptake capacity of 2.61%wt is also considered among the best zeolites. It only has a capacity of 8 molecules per cell. However, this small number of molecules per cell still makes a larger percentage weight hence making THO a good material for hydrogen uptake. From the data presented in this work it

is quite evident that the number of molecules loaded per cell of a zeolite does not qualify the material to be the best for hydrogen storage. For instance, several zeolites with very high number of molecules per cells have been overtaken by those with fewer molecules per cell. For example, CLO with a loading of 143 molecules per cell has a hydrogen uptake capacity of 2.4%wt. This makes it the fifth in the rank. Zeolite NPO has only a loading of 4 molecules per cell, but percentage mass of 2.19%wt. Other zeolites with high loading of hydrogen molecules but low percentage mass among many include, MWF, MAZ, OBW, GIU, KFI, IFU, IMF, SBT, EEI, TSC and SFV which have loadings of 225, 12, 19, 20, 20, 20, 31, 22, 24, 50 and 67 molecules per cell respectively with low percentage masses of (0.52, 1.11, 0.83, 0.69, 0.69, 0.52, 0.36, 0.51, 0.4, 0.29 and 0.43) %wt respectively. This behavior is exhibited by several other zeolites in table 1. This could be attributed to the fact that despite the number of molecules loaded, the mass of the zeolite is very important to determine the percentage weight of the adsorbate in line with other framework properties. This means that a good material for adsorption should have a suitable mass, density, pore volume and surface area. In addition, the current data shows clearly that pore sizes alone cannot determine the hydrogen storage capacity of any zeolite. This is shown by several zeolites having small pore sizes but exhibiting a higher uptake capacity. On the other hand several zeolites with extra-large pore sizes exhibit a very low hydrogen uptake capacity. One of the reasons may be that the pore size needs to be narrow to confine adsorbed gas. For instance, JBW zeolite with small pore size has a better capacity 3.25%wt whereas PAU with extra-large pore size is the least among the 233 zeolites studied with a capacity of 0.03%wt. This is in contrast to our previous studies of the adsorption of hazardous on heavy metal cations on the 242 zeolites by employing molecular simulations and machine learning techniques, where the role of pores, topology, and chemical characteristics in the sorption was examined[1]. The

results showed that only the zeolites with high diameter of pores exhibited appreciable loading of the cations. In our other study of adsorption of CrO_4^{2-}, AsO_4^{3-}, NO_3^- and PO_4^{3-} on zeolites[3], it was established that CLO, LTN, MWF, TSC, ITV, PAU, FAU and DFO zeolites are the best performing in terms of loading while several zeolites like ANA, DFT, BIK, SBN and JNT gave no loading at all. Largest overall cavity diameter, mass and accessible pore volume appeared to be the three most important descriptors affecting loading[3].

To complement the molecular simulation results, machine learning has been used to gain more chemical insights into loading capacity of hydrogen onto the zeolites by ranking how importance of each structural parameter (descriptor). At first, we have ranked the influence of Di, DPS, GSA, VSA, APV, HVF, D and M on the percentage weight (Figure 3). The results below clearly show that Di, density D and mass M negatively affects the percentage weight capacity. Density of the zeolite also affects the storage capacity negatively such that the denser the material the lower the percentage weight. Apart from the three parameters, the rest have positive effect on the percentage weight. It is evident that GSA and VSA have the highest positive impact to the percentage weight. From this, the best material could be achieved by reducing the mass and density while increasing both gravimetric and volumetric surface area.

In addition, we have also ranked the influence of Di, DPS, GSA, VSA, APV, HVF, D and M on the number of adsorbed molecules per cell (L) as shown in figure 4. Mass has shown highest positive correlation with loading (L). Di is the second parameter after mass affecting the number of adsorbed molecules positively while APV is the third.

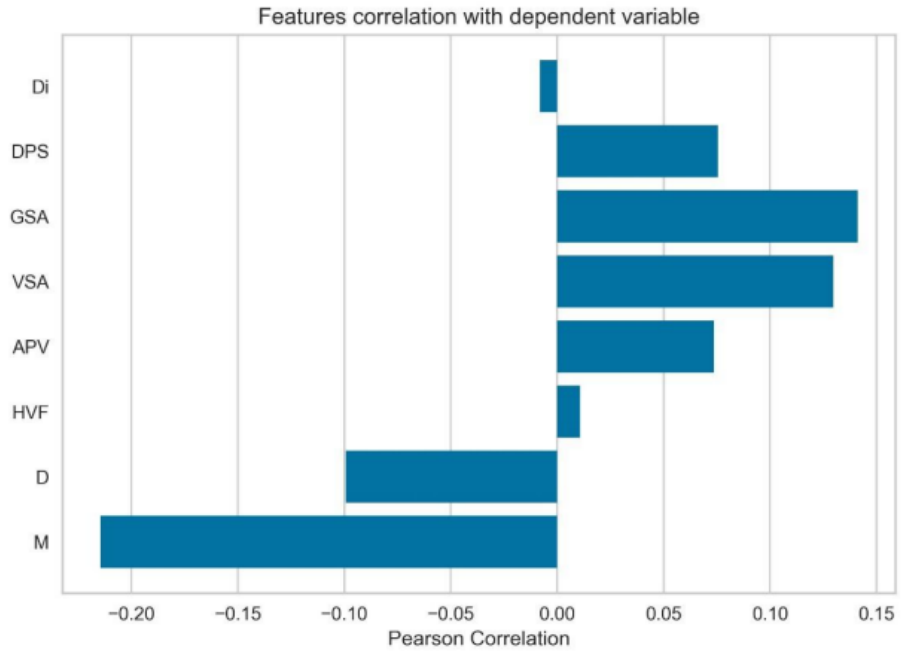

Figure 3. Pearson correlation between features and dependent variable (percentage weight)

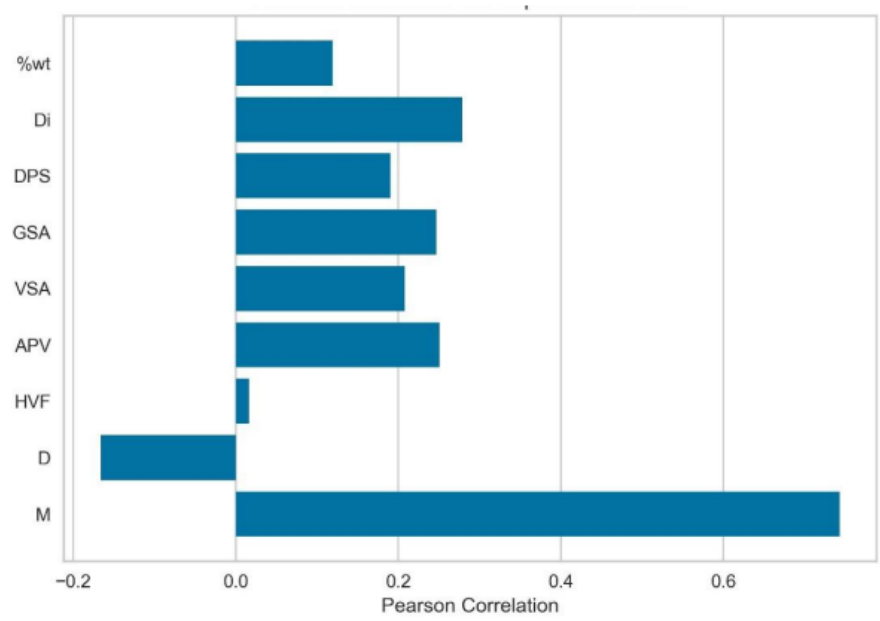

Figure 4. Pearson correlation between features and dependent variable (loading)

Random forest (RF), k-nearest neighbor (k-NN), gradient boosting model, linear regression (LR) and support vector machine (SVM) are used for regression analysis. Data is divided in training and test sets with various ratios, 70:30% training: test ratio has showed better performance for all models. Performance of random forest (RF) and gradient boosting model is much better than other models. The scatter plots for correlation between calculated and predicted loading are given in Figure 5, respectively for random forest model (left) and gradient boosting model(right). In case of random forest model, R^2 values for training and test sets are 0.87 and 0.79, respectively. In case of gradient boosting model, R^2 values for training and test sets are 0.86 and 0.82, respectively. Performance of both the models is sufficiently high.

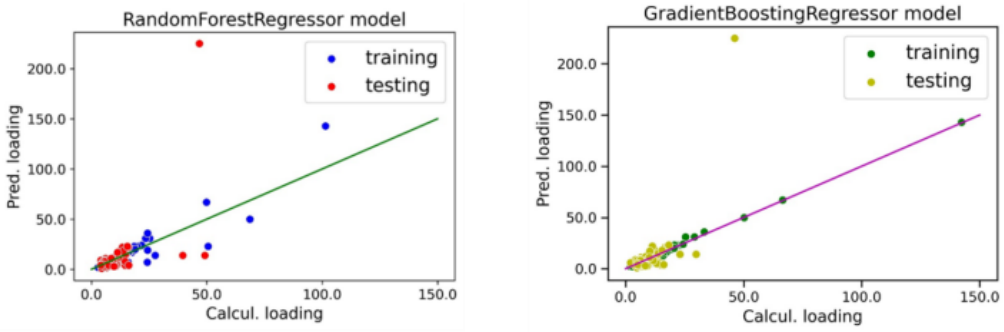

Figure 5. (Left)Scatter plot between calculated and predicted loading values through random forest model. (Right) Scatter plot between calculated and predicted loading values through gradient boosting model.

Bearing in mind that the use of zeolites as hydrogen storage media has been experimentally and theoretically investigated using several zeolites of different pore architecture and composition, it is important to also compare our results with previous studies. The hydrogen storage capacities of some selected nanoporous materials are shown in table 2. It is clear that most of the theoretical and experimental results provided in literature closely match with our

results, with small variations resulting from different conditions i.e., temperature and pressure. For instance, previous studies had shown that zeolite H-OFF at 77K and a pressure of 1.6MPa has a capacity of 1.75%wt[7]. This study was done experimentally and the results are closely related to the findings in our study at 298K and a pressure of 1013KPa which provides that zeolite OFF has an uptake capacity of 1.29%wt at a temperature of 298K and a pressure of 1013KPa. However, the slight difference is attributed to the difference in pressure and temperature. Similarly MAZ zeolite from experimental results has a capacity of 1.64%wt which compares with the findings of this study of 1.11%wt. Elsewhere, zeolite templated carbon (ZTC) has been investigated theoretically under 77K and a pressure of 1 bar and found to have a hydrogen capacity ranging from 0.64 to 3.00 %wt [27]. Another study was conducted at 298K and a pressure of 100 bar and found to have a capacity ranging between 0.07 to 1.31%wt [28].

Table 2 Comparison of our work with other studies

Adsorbent	Temperature	Pressure	H_2 uptake (%wt)	Reference	Type of study
LTA zeolite	77K	1.51MPa	1.54		Experimental
LTA zeolite	298K	1013KPa	4.8	This study	
H-OFF zeolite	77K	1.6MPa	1.75	[7]	Experimental
OFF zeolite	298K	1013KPa	1.29	This study	
Na-MAZ zeolite	77K	1.6MPa	1.64	[7]	Experimental
MAZ zeolite	298K	1013KPa	1.11	This study	
JBW zeolite	298K	1013KPa	3.25	This study	
RTH zeolite	298K	1013KPa	2.89	This study	
Random CNT networks	77	1bar	2.84-3.34	[29]	Experimental
Exfoliated GO	77K	1 bar	1.2	[30]	Experimental
Diamond derived grapheme	77K	1 bar	0.68	[31]	Experimental
GO frameworks (GOFs)	77K	1 bar	0.35-0.92	[32,33]	Experimental
ZTC	77K	1 bar	0.64-3.00	[34]	Theoretical
FPGNs	77K	100 bar	1.69-10.35	[27]	Theoretical
SWCNTs	77K	100 bar	2.75-3.60	[35]	Experimental
Random CNT networks	77K	100 bar	5.01-8.85	[29]	Experimental
Pillared graphene	77K	100 bar	7.2	[36]	Theoretical
porous nanotube networks	77K	100 bar	5.8-23.6	[27]	Theoretical

ZTC	77K	100 bar	0.81-9.23	[34]	Theoretical
FPGNs	298K	100 bar	0.61-1.86	[36]	Theoretical
MWCNT	298K	100 bar	0.2	[37]	Experimental
Random CNT networks	298K	100 bar	1.47-2.00	[38]	Experimental
MWCNT	298K	100 bar	0.68	[35]	Experimental
Nitrogen- incoporated carbon nanotube	298K	100 bar	0.9-2.0	[37]	Experimental
ZTC	298K	100 bar	0.07-1.31	[28]	Theoretical

We further used quantum chemical calculations to investigate the interaction of the zeolites, with hydrogen. We have focused on the interaction of MWF with hydrogen, considering, among the 233 zeolites (table S1, supporting information), MWF exhibits the highest loading of 225 hydrogen molecules per cell. The MWF zeolite cluster was modeled according to literature (Figure 5)[39]. Based on the modeled MWF zeolite cluster, three possible adsorption sites (MWF-O, MWF-Si, and MWF-Si-O sites) were predicted for hydrogen adsorption according to Figure 4 above. The quantum chemical calculations were conducted to calculate the global reactivity electronic descriptors along with the HOMO-LUMO energy gap of the studied systems[40]. According to the well-known Koopmans approximation, the ionization Potential (IP) and the Electron Affinity (EA) are given by;[41]

$$IP = -E_{HOMO} \quad (1)$$

$$EA = -E_{LUMO} \quad (2)$$

$$-\mu = {}^{1}/_{2}\,(E_{HOMO} + E_{LUMO}) = \chi \quad (3)$$

$$\eta = {}^{1}/_{2}\,(IP - EA) = \frac{E_{LUMO} - E_{HOMO}}{2} \quad (4)$$

$$\omega = \frac{\mu^2}{2\eta} \quad (5)$$

$$S = \frac{1}{2\eta} = \frac{1}{IP-EA} = \frac{1}{E_{LUMO}-E_{HOMO}} \quad (6)$$

Where μ, χ, η, ω, and S are are the chemical potential, electronegativity, chemical hardness electrophilicity, and chemical softness respectively[42]. The energy gap and the global reactivity descriptors of the studied compounds are presented in **Table 2** while the molecular orbital distributions of all the possible adsorption modes are presented in Figure 6. From the HOMO LUMO energy gap results shows a variation in the energy values as the hydrogen is absorbed within the MWF zeolite framework[43]. The variation in energy gap for the hydrogen absorption on the different active sites within the MWF zeolite is given as 8.26, 8.23, and 7.99 eV for MOF H_2-Si, MOF-H_2-Si-O, and MOF-H_2-O respectively.

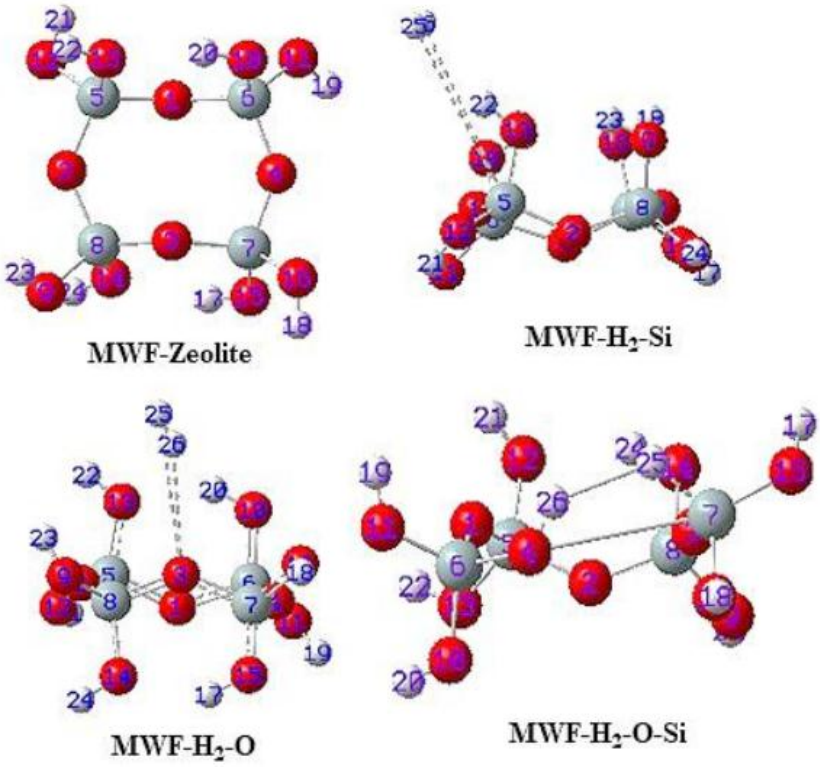

Figure 6. Modeled MWF zeolite cluster and the associated possible adsorption configurations

Table 2. Global reactivity descriptors of the studied surfactants and complexes

S/no	MOF	MOF-H_2-S	MOF-H_2-O	MOF-H_2-S-O
HOMO/eV	-8.73	-8.92	-8.73	-8.95
LUMO/eV	-0.75	-0.66	-0.74	-0.72
Energy gap/eV	7.98	8.26	7.99	8.23
Softness	0.13	0.12	0.12	0.12
Hardness	3.99	4.13	3.99	4.11
Electrophilicity	2.81	2.77	2.80	2.83
Electronegativity	-4.74	-4.79	-4.73	-4.83

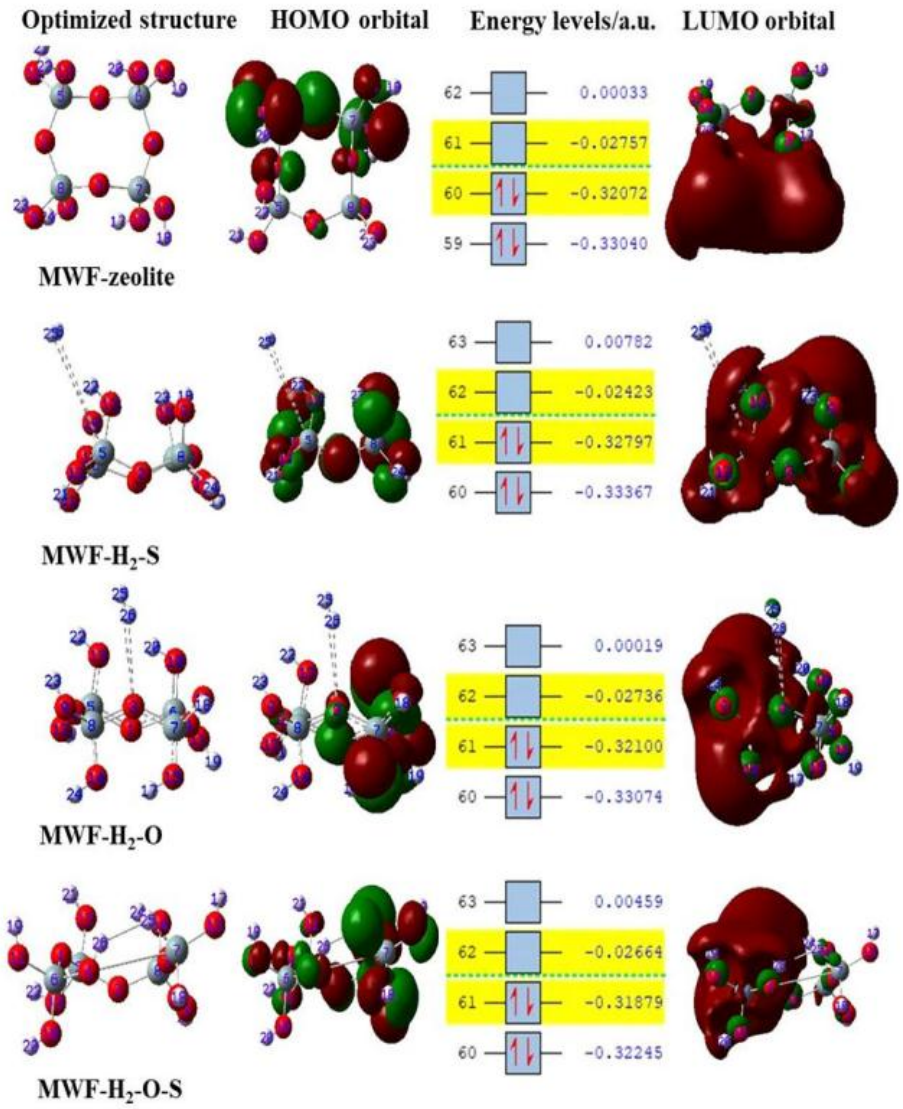

Figure 7. The optimized structures, HOMO orbitals, energies, and LUMO orbitals of the studied systems

Adsorption energy has also been calculated to provide more chemical interaction insight[44]. Generally, the adsorption energy of an adsorbate (hydrogen) trapped on the surface of an adsorbent (cluster) is predicted using equation (7) which is given as:

$$E_{ads} = E_{system} - (E_{adsorptive} + E_{MWF}) \quad (7)$$

Where E_{ads}, E_{system}, $E_{adsorptive}$, and E_{MWF} is the adsorption energy, total energy of the interacting system (hydrogen and cluster), total energy of the hydrogen, and total energy of the free zeolite cluster respectively[45]. The calculated adsorption energies for the three different hydrogen adsorption modes on the surface of the zeolite cluster are presented in **Table 3**. From the results, the calculated adsorption energies are -0.054, -0.027, and -1.361 eV on MWF-H_2-S, MWF-H_2-O, and MWF-H_2-S-O respectively. The MWF-H_2-S-O adsorption complex has the highest relative adsorption energy due to the strong bonding interactions of hydrogen with the S and O-atoms of the MWF cluster. Furthermore, it is also observed to possess relatively shortest hydrogen-cluster adsorption distance of 1.504 Å. This fact-finding is also supported by previous studies[39,46].

Table 3. Adsorption energies of the different possible adsorption modes of hydrogen on zeolites calculated using the gen/DFT method

S/no	MWF-H_2-S	MWF-H_2-O	MWF-H_2-S-O
$\mathbf{E_{system}}$/a.u.	-924.839	-924.838	-924.787
$\mathbf{E_{hydrogen}}$/a.u.	-1.175	-1.175	-1.175
$\mathbf{E_{MOF}}$/a.u.	-923.662	-923.662	-923.662
$\mathbf{E_{ads}}$/eV	-0.054	-0.027	-1.361
Distance/Å	4.374	2.937	1.504

In order to offer details on the intra/inter molecular hydrogen bonding [47], natural bond orbital analysis was performed at B3LYP/ 6-31G+(d) level of theory. The corresponding donor-acceptor

stabilization energy, $E^{(2)}(i \rightarrow j)$ for each donor (i) NBO and acceptor (j) NBO is given by equation (12).

$$E^{(2)} = q_i \frac{(F_{i,j})^2}{\varepsilon_j - \varepsilon_i} \quad (12)$$

Where qi is the orbital occupancy, i, j are diagonal elements and $F_{i,j}$ is the off-diagonal NBO Fock matrix element(). The most interacting donor NBO, acceptor NBO, and the stabilization NBO energies of the MWF-MOF cluster and the cluster-hydrogen interactions (MWF-H_2-S, MWF-H_2-O, and MWF-H_2-S-O) are presented in **Table 4.** As reported in the table, the observed significant donor-acceptor NBO interactions was found to occur between O_1-$Si_6 \rightarrow O_4$-Si_6, O_1-$Si_5 \rightarrow O_1$-Si_6, O_1-$Si_6 \rightarrow O_4$-Si_6, and O_1-$Si_6 \rightarrow O_1$-Si_5 natural bond orbitals having second order stabilization energies of 507.26 kcal/mol, 841.92 kcal/mol, 510.97 kcal/mol, and 768.11 kcal/mol respectively. The observed highest and least perturbation energies within the cluster-hydrogen interaction is observed to occur between O_1-$Si_5 \rightarrow O_1$-Si_6 and O_1-$Si_6 \rightarrow O_4$-Si_6 interacting orbitals with stabilization energies of 841.92 kcal/mol and 510.97 kcal/mol respectively.

Table 4. Most interactive stabilization energies for the hydrogen-cluster complex

Compounds	Donor NBO	Acceptor NBO	$E^{(2)}$/(kcal/mol)	E(i)-E(j)/a.u.	F(i,j)/a.u.
MWF	O_1-Si_6	O_4-Si_6	507.26	0.04	0.251
MWF-H_2-S	O_1-Si_5	O_1-Si_6	841.92	0.01	0.268
MWF-H_2-O	O_1-Si_6	O_4-Si_6	510.97	0.02	0.252
MWF-H_2-S-O	O_1-Si_6	O_1-Si_5	768.11	0.02	0.300

4.0 Conclusion

According to the molecular simulation results, LTA stands out to be the best zeolite storage of hydrogen amongst the 233 zeolites studied. It has the highest value for H_2 capacity of 4.8%wt. On the other hand, JBW follows as the second in terms %wt with 3.2 Grand Canonical Monte Carlo (GCMC) simulations have been used to evaluate the hy storage performance on 233 zeolites. A machine learning algorithm was used to ra importance of various structural features such as mass (M), density (D), helium void f (HVF), accessible pore volume (APV), gravimetric surface area (GSA), and largest cavity diameter (Di) and how they affect the capacity of the zeolites. These parameters af number of molecules per cell and the percentage weight differently. The results show tha and M have a negative effect on the percentage weight capacity, while GSA and VSA ha highest positive contribution to the percentage weight. From this, the best material co achieved by reducing the mass and density while increasing both gravimetric and volu surface area. Further quantum chemical calculations were also performed to calcul adsorption energy, global reactivity electronic descriptors, and natural bond orbital ana order to provide insights into the interaction of the zeolites with hydrogen. These e indicated that the reaction that took place in the process was exothermic.

References

1. McCusker, L. B., Olson, D. H. & Baerlocher, C. *Atlas of Zeolite Framework Types*. *Atlas o Zeolite Framework Types* (2007). doi:10.1016/B978-0-444-53064-6.X5186-X.

2. Turnbull, M. S. Hydrogen Storage in Zeolites: Activation of the Pore Space Through Incorporation of Guest Materials. 262 (2010).

3. Mulana, F. A study of hydrogen storage in zirconium- containing NaY 5 . 7 zeolite. **1**, 32–37 (2011).

4. Ennaert, T. *et al.* Potential and challenges of zeolite chemistry in the catalytic conversion of biomass. *Chem. Soc. Rev.* **45**, 584–611 (2016).

5. Russo, A. V., Andrade, C. V., De Angelis, L. E. & Jacobo, S. E. Adsorption and catalytic oxidation of organic pollutants using Fe-zeolite. *Water Sci. Technol.* **77**, 939–947 (2018).

6. Wu, D., Li, J., Yao, L., Xie, R. & Peng, Z. An Electrochemical Ethylamine/Acetonitrile Redox Method for Ambient Hydrogen Storage. *ACS Appl. Mater. Interfaces* **13**, 55292–55298 (2021).

7. Dong, J., Wang, X., Xu, H., Zhao, Q. & Li, J. Hydrogen storage in several microporous zeolites. *Int. J. Hydrogen Energy* **32**, 4998–5004 (2007).

8. Deniz, C. U. Computational screening of zeolite templated carbons for hydrogen storage. *Comput. Mater. Sci.* **202**, 110950 (2022).

9. Maesen, T. L. M., Beerdsen, E., Calero, S., Dubbeldam, D. & Smit, B. Understanding cage effects in the n-alkane conversion on zeolites. *J. Catal.* **237**, 278–290 (2006).

10. Catlow, C. R. A., Bell, R. G., Gale, J. D. & Lewis, D. W. Modelling of structure and reactivity in zeolites. *Stud. Surf. Sci. Catal.* **97**, 87–100 (1995).

11. Gramm, F. *et al.* Complex zeolite structure solved by combining powder diffraction and electron microscopy. *Nature* **444**, 79–81 (2006).

12. Systèmes, D. Biovia Discovery Studio ® 2016 Comprehensive Modeling and Simulations. 4 (2016).

13. Mayo, S. L., Olafson, B. D. & Goddard, W. A. DREIDING: A generic force field for molecular simulations. *J. Phys. Chem.* **94**, 8897–8909 (1990).

14. Kim, S. *et al.* PubChem 2019 update: Improved access to chemical data. *Nucleic Acids Res.* **47**, D1102–D1109 (2019).

15. Delley, B. An all-electron numerical method for solving the local density functional for polyatomic molecules. *J. Chem. Phys.* **92**, 508–517 (1990).

16. Delley, B. From molecules to solids with the DMol3 approach. *J. Chem. Phys.* **113**, 7756–7764 (2000).

17. Golchoobi, A. & Pahlavanzadeh, H. Extra-framework charge and impurities effect, Grand Canonical Monte Carlo and volumetric measurements of CO2/CH4/N2 uptake on NaX molecular sieve. *Sep. Sci. Technol.* **52**, 2499–2512 (2017).

18. Pilot, W. P. Pipeline pilot overview. 1–6.

19. Ritschl, F. *et al.* An extension of the Consistent Valence Force Field (CVFF) with the aim to simulate the structures of vanadium phosphorus oxides and the adsorption of n-butane and of 1-butene on their crystal planes. *Zeitschrift fur Anorg. und Allg. Chemie* **628**, 1385–1396 (2002).

20. García-Pérez, E. *et al.* A computational study of CO2, N2, and CH4 adsorption in zeolites. *Adsorption* **13**, 469–476 (2007).

21. Krishna, R. & van Baten, J. M. Insights into diffusion of gases in zeolites gained from molecular dynamics simulations. *Microporous Mesoporous Mater.* **109**, 91–108 (2008).

22. Frisch, M. J. *et al.* Gaussian 09, Revision B.01. *Gaussian 09, Revis. B.01, Gaussian, Inc., Wallingford CT* 1–20 (2009).

23. Eno, E. A. *et al.* Reactivity, stability, and thermodynamics of para-methylpyridinium-based ionic liquids: Insight from DFT, NCI, and QTAIM. *J. Ion. Liq.* **2**, 100030 (2022).

24. Lu, T. & Chen, F. Multiwfn: A multifunctional wavefunction analyzer. *J. Comput. Chem.* **33**, 580–

592 (2012).

25. Buitinck, L. *et al.* API design for machine learning software: experiences from the scikit-learn project. (2013).

26. Vinaches, P., Bernardo-Gusmão, K. & Pergher, S. B. C. An introduction to zeolite synthesis using imidazolium-based cations as organic structure-directing agents. *Molecules* **22**, (2017).

27. Dimitrakakis, G. K., Tylianakis, E. & Froudakis, G. E. Pillared graphene: a new 3-D network nanostructure for enhanced hydrogen storage. *Nano Lett.* **8**, 3166–3170 (2008).

28. Yang, S. J., Jung, H., Kim, T. & Park, C. R. Recent advances in hydrogen storage technologies based on nanoporous carbon materials. *Prog. Nat. Sci. Mater. Int.* **22**, 631–638 (2012).

29. Ozturk, Z. *et al.* Hydrogen storage in heat welded random CNT network structures. *Int. J. Hydrogen Energy* **40**, 403–411 (2015).

30. Wang, Y., Guan, C., Wang, K., Guo, C. X. & Li, C. M. Nitrogen, hydrogen, carbon dioxide, and water vapor sorption properties of three-dimensional graphene. *J. Chem. Eng. Data* **56**, 642–645 (2011).

31. Subrahmanyam, K. S., Vivekchand, S. R. C., Govindaraj, A. & Rao, C. N. R. A study of graphenes prepared by different methods: Characterization, properties and solubilization. *J. Mater. Chem.* **18**, 1517–1523 (2008).

32. Burress, J. W. *et al.* Graphene oxide framework materials: Theoretical predictions and experimental results. *Angew. Chemie - Int. Ed.* **49**, 8902–8904 (2010).

33. Srinivas, G., Burress, J. W., Ford, J. & Yildirim, T. Porous graphene oxide frameworks: Synthesis and gas sorption properties. *J. Mater. Chem.* **21**, 11323–11329 (2011).

34. Nishihara, H. *et al.* High-pressure hydrogen storage in zeolite-templated carbon. *J. Phys. Chem. C*

113, 3189–3196 (2009).

35. Yuca, N. & Karatepe, N. Hydrogen storage in single-walled carbon nanotubes purified by microwave digestion method. *World Acad. Sci. Eng. Technol.* **79**, 605–610 (2011).

36. Mert, H., Deniz, C. U. & Baykasoglu, C. Monte Carlo simulations of hydrogen adsorption in fullerene pillared graphene nanocomposites. *Mol. Simul.* **46**, 650–659 (2020).

37. Zhu, H. *et al.* Hydrogen adsorption in bundles of well-aligned carbon nanotubes at room temperature. *Appl. Surf. Sci.* **178**, 50–55 (2001).

38. Yang, S. J., Cho, J. H., Nahm, K. S. & Park, C. R. Enhanced hydrogen storage capacity of Pt-loaded CNT@MOF-5 hybrid composites. *Int. J. Hydrogen Energy* **35**, 13062–13067 (2010).

39. Unimuke, T. O., Louis, H., Eno, E. A., Agwamba, E. C. & Adeyinka, A. S. Meta-Hybrid Density Functional Theory Prediction of the Reactivity, Stability, and IGM of Azepane, Oxepane, Thiepane, and Halogenated Cycloheptane. *ACS Omega* **7**, 13704–13720 (2022).

40. Louis, H. *et al.* Synthesis, characterization, DFT, and TD-DFT studies of (E)-5-((4,6-dichloro-1,3,5-triazin-2-yl)amino)-4-hydroxy-3-(phenyldiazenyl)naphthalene-2,7-diylbis(hydrogen sulfite). *SN Appl. Sci.* **3**, (2021).

41. Enudi, O. C. *et al.* Understanding the aqueous chemistry of quinoline and the diazanaphthalenes: insight from DFT study. *Heliyon* **7**, e07531 (2021).

42. Louis, H., Guo, L. J., Zhu, S., Hussain, S. & He, T. Computational study on interactions between CO2 and (TiO2)n clusters at specific sites. *Chinese J. Chem. Phys.* **32**, 674–686 (2019).

43. Kachurovskaya, N. A., Zhidomirov, G. M., Hensen, E. J. M. & Van Santen, R. A. Cluster model DFT study of the intermediates of benzene to phenol oxidation by N2O on FeZSM-5 zeolites. *Catal. Letters* **86**, 25–31 (2003).

44. Oluigbo, C. J. *et al.* Controllable fabrication of abundant nickel-nitrogen doped CNT electrocatalyst for robust hydrogen evolution reaction. *Appl. Surf. Sci.* **562**, (2021).

45. Bisong, E. A. *et al.* Vibrational, electronic, spectroscopic properties, and NBO analysis of p-xylene, 3,6-difluoro-p-xylene, 3,6-dichloro-p-xylene and 3,6-dibromo-pxylene: DFT study. *Heliyon* **6**, e05783 (2020).

46. Anyama, C. A. *et al.* Experimental and Density Functional Theory Studies on a Zinc(II) Coordination Polymer Constructed with 1,3,5-Benzenetricarboxylic Acid and the Derived Nanocomposites from Activated Carbon. *ACS Omega* **6**, 28967–28982 (2021).

47. Wang, Q. *et al.* Experimental, DFT and MD evaluation of Nandina domestica Thunb. extract as green inhibitor for carbon steel corrosion in acidic medium. *J. Mol. Struct.* **1265**, 133367 (2022).